



HAL
open science

Potential of radiation sensitive silica-based optical fibers for dosimetry and regeneration techniques

Gaetano Li Vecchi

► **To cite this version:**

Gaetano Li Vecchi. Potential of radiation sensitive silica-based optical fibers for dosimetry and regeneration techniques. Optics [physics.optics]. Université Jean Monnet - Saint-Etienne, 2022. English. NNT : 2022STET0061 . tel-04200508

HAL Id: tel-04200508

<https://theses.hal.science/tel-04200508>

Submitted on 8 Sep 2023

HAL is a multi-disciplinary open access archive for the deposit and dissemination of scientific research documents, whether they are published or not. The documents may come from teaching and research institutions in France or abroad, or from public or private research centers.

L'archive ouverte pluridisciplinaire **HAL**, est destinée au dépôt et à la diffusion de documents scientifiques de niveau recherche, publiés ou non, émanant des établissements d'enseignement et de recherche français ou étrangers, des laboratoires publics ou privés.



N°d'ordre NNT: 2022STET0061

THÈSE de DOCTORAT DE L'UNIVERSITÉ JEAN MONNET SAINT-ÉTIENNE

Membre de la COMUE de LYON

**École Doctorale N° 488
(SCIENCES, INGÉNIERIE, SANTÉ)**

Spécialité / discipline de doctorat :
Optique, Photonique et Hyperfréquences

Soutenue publiquement 16/12/2022, par :
GAETANO LI VECCHI

Potential of radiation sensitive silica-based optical fibers for dosimetry and regeneration techniques

Devant le jury composé de :

OUERDANE, Youcef	Prof. des Universités, Saint-Etienne	Président
GAILLARDIN, Marc	Directeur de recherche, CEA	Rapporteur
BOUZAOUÏ, Mohammed	Prof. des Universités, Lille	Rapporteur
RIZZOLO, Serena	Docteur, Airbus	Examinatrice
GIRARD, Sylvain	Prof. des Universités, Saint-Etienne	Directeur de thèse
KADI, YACINE	Professeur, CERN	Co-directeur de thèse

Table of contents

Table of contents	2
1 Chapter I - State-of-the-Art.....	13
1.1 Radiation effects on optical fibers: RIA, RIE, RIRIC	14
1.1.1 General theory	15
1.1.2 Radiation effects on P, P _{Ce} doped fibers	33
1.1.3 Radiation effects on Al doped fibers.....	40
1.2 Dosimetry with optical fibers	43
1.2.1 Radiation Induced Emission (RIE).....	43
1.2.2 Optically Stimulated Luminescence (OSL)	44
1.2.3 Thermally Stimulated Luminescence (TSL).....	45
1.2.4 Radiation Induced Attenuation RIA.....	46
1.3 CERN needs and selection of RIA-based dosimeter for the study.....	48
2 Chapter II - Investigated Samples and Experimental Tools	50
2.1 Selected radiation-sensitive optical fibers	50
2.2 Selected instrumentation.....	54
2.2.1 Optical Time Domain Reflectometer (OTDR), HR-OTDR.....	55
2.2.2 Optical Frequency Domain Reflectometers (OFDR).....	58
2.3 Irradiation facilities.....	60
2.3.1 ⁶⁰ Co facility at CERN.....	60
2.3.2 CHARM facility at CERN	61

2.3.3	MOPERIX machine in Saint-Etienne	63
2.3.4	TRIUMF facilities (Vancouver, Canada).....	65
2.4	Experimental setups.....	67
2.4.1	RIA, RIA/T, T (recovery)	67
2.4.2	Cut-back	68
2.4.3	Photobleaching	70
2.4.4	H ₂ -Loading.....	72
3	Chapter III - Investigation of the Fiber Dosimetry Properties	74
3.1	Definition of the dosimetry properties.....	74
3.2	Dosimetry properties of the optical fibers	75
3.2.1	Dose dependence	76
3.2.2	Dose rate dependence	77
3.2.3	Effect of successive irradiations.....	83
3.2.4	Temperature dependence for CERN applications	93
3.2.5	Temperature dependence of P-doped fiber from -80°C to 300°C.....	97
3.3	Discussion of the dosimetry potentials of the three fibers.....	102
4	Chapter IV. P-doped Fiber Dosimetry in different radiation fields	105
4.1	Experiments done at CERN facilities	105
4.1.1	Investigations based on post mortem measurements	105
4.1.2	Experiment at the Proton Synchrotron Booster (PSB).....	110
4.2	Experiments at TRIUMF Facilities	113
4.2.1	Experiment at PIF facility: 480 MeV protons	113

4.2.2	Experiment at TNF facility: atmospheric neutrons	114
5	Chapter V. Towards Optimized P-doped Optical Fiber Dosimetry.....	118
5.1	. Role of the guiding properties	119
5.1.1	Spectral study of the RIA in the selected OFs (NIR).....	122
5.2	Regeneration of the dosimeter through H ₂	125
5.3	. Regeneration of the dosimeter through photobleaching.....	132
5.4	Spatial resolution investigation	141

Conclusions

*To my son Enzo,
May the eyes of his mind discover
All that mine have not been able to see.*

Acknowledgements

This PhD thesis has been realized in collaboration between the Laboratoire Hubert Curien of the University of Saint-Etienne (France) and the Conseil Européen pour la Recherche Nucléaire (CERN) (Switzerland). This thesis was carried out as part of the distributed optical fiber radiation sensor (DOFRS) project at CERN, which I participated in during my PhD years.

The strength and beauty of research lies in imagining and trying to understand what is not yet clear or known. The constant quest for knowledge has always been inherent in human nature. I too, in my own small way, have been captured by the fascination of research and have tried to be part of it during my experience.

As all great minds know, and as Prof. Giorgio Parisi himself, who recently won the Nobel Prize for physics, has openly declared, research is a team game and only through collaboration and sharing can important results be achieved.

Since for me the fact that I was able to complete this path is a great achievement, I feel obliged to thank a few people who have stood by me during this period, which was certainly not easy for me. As I am not a great speaker, I will limit myself to mentioning just a few people who are, however, representative of the research groups I have had the honour of working with.

First of all, I must thank the entire MOPERE group in Saint-Etienne and in particular Prof. Sylvain Girard, my thesis director. It is only thanks to him that this thesis has come to light. His intellectual honesty and human support have been milestones for me in completing this manuscript.

I must thank Prof. Yacine Kadi, my thesis co-director and supervisor at CERN, where I spent most of my PhD. He was always available and a valuable support in the moments of difficulty that were not lacking.

Finally, I would like to thank the person who, more than any other, has been close to me, even if distant, and who has supported and put up with me over these long years, but who at the same time has given me immense joy, thank you MAKKA.

INTRODUCTION

Fiber optic sensor technology was initially suggested about half a century ago. By the early 1980s, the basic principle of so-called distributed fiber sensing architecture began to emerge. It is an exciting idea to exploit a telecom-grade optical fiber and look out how the evolving surrounding environment affects its transmission characteristics. The first historical application of fiber optics was in the field of telecommunications, occurring at the same time as the development of semiconductor lasers [1]. The constant needs to transmit more and more information in ever more quickly way have led to an exponential increase of the R&D activities about optical fibers (OFs). Any kind of information (text, music, images, ...) can be encoded in light pulses travelling for thousands of kilometers along these dielectric waveguides as thin as human hairs. The scientific community has recently recognized the importance of OFs by assigning the Nobel Prize in Physics (2009) to C. K. Kao, who started working on OFs in the sixties and first understood, in 1966, the potentiality of low-loss silica-based waveguides for telecommunications. Since then, the progress in OFs has never stopped and in fact, more and more applications related to this technology have risen [1]. Nowadays the use of OFs runs from the telecommunications to structural health monitoring applications in civil, space or industrial environments [2].

In addition to optical communications, OFs and related technologies have found a variety of other applications ranging from precision metrology to photonic sensors. Various optical measurement techniques have been proposed and demonstrated in R&D, maintenance and trouble-shooting of fiber-based systems. Different optical systems require specific measurement and testing techniques depending on the key requirements of each application [3]. Over the years, fiber-optic measurement has become a stand-alone research discipline, which is both interesting and challenging.

The field of distributed optical fiber sensors (DOFSs) has grown from an intriguing concept in the early 1980s to a technology that has widespread usage today, and it continues to be the subject of very active research [2]. Distributed sensors have become a ‘de facto’ standard way of operating, for example, in the monitoring of high-voltage transmission cables, fire detection applications ... These practical applications have, in turn, led to the development of a number of actors dedicated to the supply of DOFSs and their data analysis.

Distributed optical fiber sensing is attracting considerable attention in several application fields for its unique capability to accurately and continuously measure physical parameters, such as temperature, strain, pressure, liquid levels over distances reaching tens of kilometers with meter or sub-meter scale spatial resolutions. Nowadays, the Large Hadron Collider (LHC) along with the pre-accelerators present in CERN’s accelerators complex benefit, for example, from a distributed temperature monitoring system (DTS) ensuring the immediate and reliable detection of abnormal temperature variations which could for example indicate the presence of a fire or a cooling liquid leakage. It also benefits from the distributed optical fiber radiation sensor (DOFRS) that monitor the dose of radiations deposited along the fiber pathway all around selected accelerators, helping in reducing the radiation risk on microelectronic components. In fact, such DOFRS and DTS were combined, to discriminate between the evolutions of the two measurands, although today’s systems at CERN do not require it anymore. Usually, the DOFRS operation principles are based on radiation induced attenuation (RIA) measurements. Depending on the fiber type and the interrogation optical wavelength, the sensor will be more or less sensitive and spatially-resolved. Among the various types of radiation-sensitive optical fibers (exhibiting high RIA levels), the most investigated ones are the Phosphorus-doped optical fibers. However, these state-of-the-art systems using OTDR still have some limitations such as an operational dose ranging up to a few kGy, no possibility to reset the dosimeter, limited dynamics....Furthermore in order to be able to use these fibers sensors in the tunnels of CERN’s

accelerator complex, they have been characterized and tested in a representative (and more complex) radiation environment. This was achieved using the new CERN High energy AccelRator Mixed field facility (CHARM) facility that is associated to a mixed field radiation environment, including not only photons but also protons, neutrons, muons and other particles, representative of the LHC radiation environment. This PhD thesis is part of the Optical Fibre Dosimetry work package of the Radiation To Electronics (R2E) project, whose foundations were laid during Dr. Iacopo Toccafondo's thesis and after was supervised by Dr. Diego Di Francesca, this project has today achieved remarkable results. I, in my small way, had the honor to take part in it and give my contribution during my PhD work. The project supervisor and co-director of my thesis was Prof. Yacine Kadi. The work was then associated with the Radiation to Electronics (R2E) team. This team, among various key activities, operates the CHARM [4] facility authorizing the access to a unique tool to investigate the potential of the systems developed in the framework of this project.

The objectives of this work are to evaluate the limits of the state-of-the-art techniques, to propose innovative fiber sensor architectures to overcome the remaining issues, this innovation being done at the component (*new specialty optical fibers differently doped*) or system (*interrogation technique, HR-OTDR, OFDR*) levels. The main objective is to identify the structure of the fiber and the interrogation scheme that allows to achieve the performance required by CERN: dose monitoring in the range of 1 Gy(SiO₂) to 100 kGy, with a spatial resolution below one meter with a sensor independent to the dose rate and the temperature in the 15-35°C range. Part of the development about the fiber itself has benefited from the close collaboration between LabHC and the French fiber manufacturer iXBlue Photonics through their joint research laboratory, the LabH6. More precisely, during this work we target to 1) understand the physics of radiation effects in silica-based materials 2) identify ways to control the radiation response of the fibers by acting on its compositions, structure, pre- or post-

treatments; 3) to develop and test fiber sensor prototypes at LabHC MOPERIX, CHARM and ^{60}Co facilities et 4) to analyze the obtained results, determine the sensor performances, limitations, integration procedure at LHC.

Last but not least, we worked on a protocol to regenerate the optical fiber dosimeter damaged by radiation and to be able to reuse it without having to replace it. We also showed how this process can be repeated several times without changing the dosimeter response.

The PhD thesis is organized in 5 Chapters. In Chapter I, we present the theoretical background on the radiation interaction with silica-based optical fibers and the major induced effects at both macroscopic and microscopic scales. We introduce the mathematical formalism to describe the light propagation along the fiber and give a short overview about the main point defects that radiation generates in the silica-based core and cladding of the OFs studied (doped with either P, PCe or Al). Finally, the motivation to develop for CERN needs a distributed fiber optic sensor are developed as well as the main research axis followed during the PhD thesis.

In Chapter II we give the experimental details on the investigated samples, describe the employed facilities and setups for the radiation testing, the experimental setups for the thermal, H_2 loading and photo-bleaching treatments.

Chapter III presents the results of our study regarding the dosimetry performances of the different radiation sensitive optical fibers. Particularly, we studied how the radiation response of our samples changes when some environmental parameters such as dose, dose-rate, temperature change and also how the fibers respond to several consecutive irradiations. Some of these results have already been published, particularly those concerning the P-doped OF, our benchmark.

Afterwards, in Chapter IV we focus on the P-doped OF that is the most exploited fiber in this PhD thesis work, shedding light on the response of the fiber in mixed irradiation fields, such as

those found in CERN tunnels, by reporting the results of measurements made online and postmortem at the CHARM facility of CERN in Geneva.

The strategy to improve the performance of our dosimeter and optimize its applications are described in Chapter V. Here, we present a study about the light guiding effect on the fiber radiation response, the impact of pre- and post-irradiation on the radiation induced optical losses. We also present the results regarding the regeneration of the fiber-based dosimeter, first by exploiting hydrogen-loading of the fiber, second through an innovative photobleaching-based method.

1 Chapter I - State-of-the-Art

The radiation-matter interaction processes and in particular their exploitation are involved in many research fields. Whether we are talking about ionizing radiation or particle radiation interacting with the material i.e. dielectric or semiconductor, the primary effect is an energy transfer to the matter with consequent occurrence of secondary processes and so-on (cascade effects). Figure 1.1 gives a schematic representation about the processes occurring during the radiation interaction with glass. All these processes lead to a modification of the electronic and atomic structures resulting into transient or permanent changes of the material with repercussions on its optical and mechanical properties.

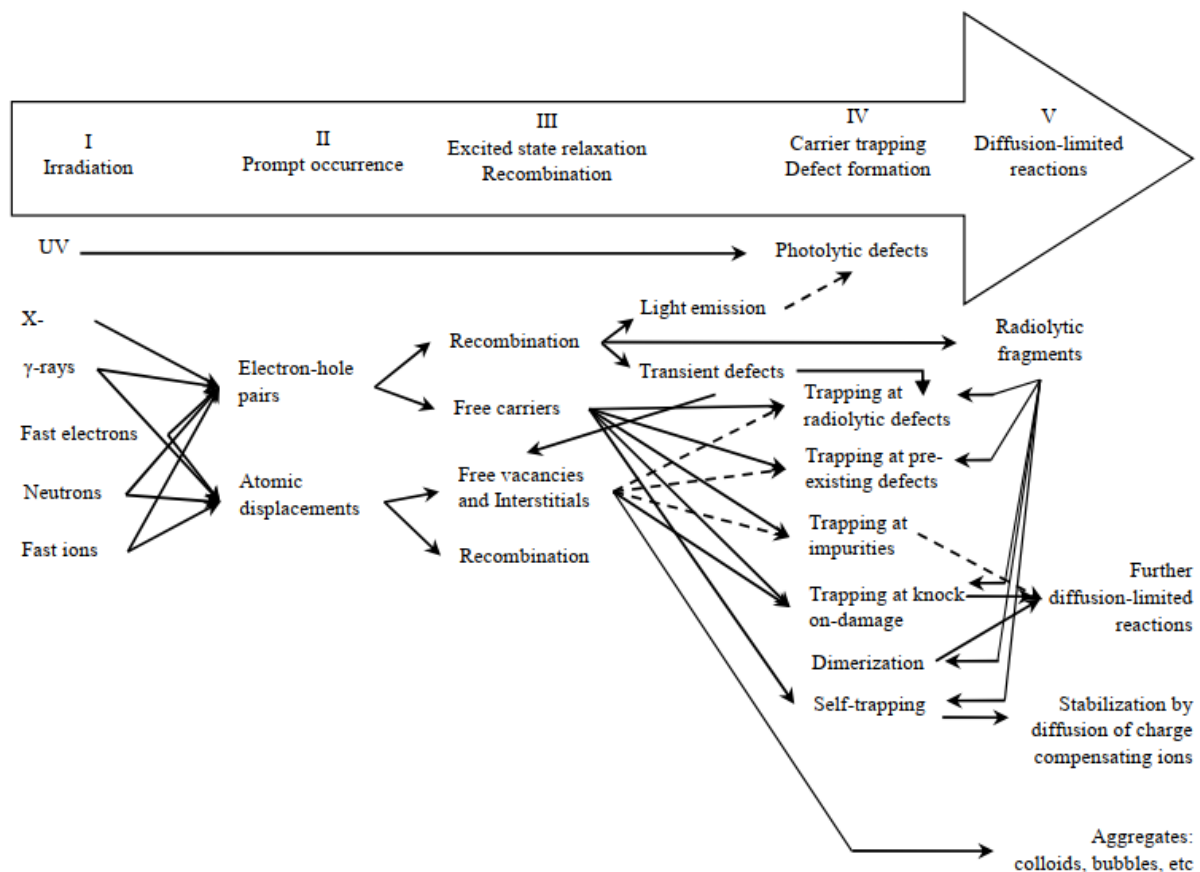


Figure 1.1 Diagram of the most relevant radiation-damage effects in glass material [5].

For the purposes of this PhD thesis, we mainly focused on the effects of ionizing radiation on the response of silica-based optical fibers (OFs), in particular on its impact on its transmission properties. We will show that we could exploit to our advantage these radiation effects in so-called radiation-sensitive optical fibers to design radiation detectors and even dosimeters. Furthermore, taking advantage of the numerous developments regarding the fiber interrogators, we will show that these detectors or dosimeters could be either punctual or distributed, meaning, for this last case, that the dose could be monitored all along the fiber length with a spatial resolution of about one meter.

1.1 Radiation effects on optical fibers: RIA, RIE, RIRIC

Optical Fibers (OF) are waveguides used for several decades in telecommunications for the transmission of large amounts of data. Thanks to their unique advantages such as their quasi-immunity to electromagnetic perturbations, low attenuation, high bandwidth, multiplexing capability, low weight and volume and others, their application field strongly enlarges as well as the diversity of profiles of use. This is particularly true for what concerns the fiber-based sensing applications. In particular, OFs have found widespread use in radiation-rich environments such as space, high energy physics facilities or nuclear/dismantling industries. Given the objectives of this thesis work, we have treated only the most usual OFs, i.e. the ones based on pure or doped silica glasses (*eg. polymer-based fibers are not considered*) and those using the total internal reflection (TIR) to ensure the light guidance (*excluding hollow-core optical fibers*). For a broader overview of the different types of OFs used in radiation environments, more information can be found in [6,7]. When the OFs are installed in such severe environment, the radiation impinging on the variously doped silica layers of the OF generate several physical phenomena, leading to the generation of microscopic point defects that affect the waveguide macroscopic properties. The main radiation effects that should be considered are: the radiation induced attenuation (RIA), the radiation induced emission (RIE) and

radiation-induced refractive change (RIRIC). In the following paragraph we will briefly present the physical principles underlying these three phenomena.

1.1.1 General theory

When radiation hits the fiber, whether photons, protons, neutrons or heavy particles, the silica matrix, doped or not, changes as well as its macroscopic properties [7]. The amplitudes and kinetics of these changes depend on several factors. However, it is today well-known that they strongly depend on the chemical composition of the SiO₂ matrix and of the choices made for the dopant used to modulate the refractive-index of the core or cladding. Furthermore, the presence of impurities, introduced voluntary or not (hydroxyl groups, chlorine) during the fiber fabrication process, could also totally modify the glass radiation response.

Radiation-Induced Attenuation (RIA) corresponds to the increase of the fiber linear attenuation due to the appearance of optical absorption bands associated with the different radiation-induced defects. RIA is directly related to the nature of the chemical elements incorporated in the fiber core and cladding. This phenomenon is then naturally wavelength-dependent and usually the RIA is stronger at shorter wavelength (UV-VIS spectral region) where most of the defects' absorption bands are located. RIA is even time-dependent, temperature-dependent and dose-rate dependent, as all these parameters affect the generation or recombination rates of the point defects. It was demonstrated that at the end of the radiation, there is often a spontaneous RIA recovery, due to the recombination of metastable defects through thermal or photo-bleaching processes [8,9].

Radiation-Induced Emission (RIE) consists of light emission from the silica-based fiber under irradiation. This emission could be due to electronic transitions between the ground and the excited point defect states, we then talk about radiation-induced luminescence, RIL. The luminescence can arise from either pre-existing defects (also called sometimes color centers)

or from radiation induced point defects. Another possible source of parasitic light is the Cerenkov emission that occurs when a charged particle propagates through a dielectric medium at a speed greater than the speed of propagation of the light in that medium. Cerenkov radiation explains for example the blue glow of underwater nuclear reactor.

Radiation Induced Refractive Index Change (RIRIC) is caused by a combination of effects due to radiation-induced changes in matrix density, theoretically explained by the Lorentz-Lorenz formula, and RIA involving the creation of associated point defects explained through the Kramers-Krönig relations. In theory, the density effect is also included in the Kramers-Krönig relations but in practice it is more convenient to separate the color centers contribution, responsible for the RIA, and describe the remaining changes as density effects [7,10,11].

In the last decades, these phenomena have been deeply studied to characterize and try to predict the behaviors of the OFs in a variety of environments. The relative importance of the three phenomena depends on the considered radiation environment, e.g. RIRIC is a real issue for in-core instrumentation. However, for all environments RIA remains a concern and then most of the studies were devoted to find ways to mitigate the RIA impact on the performances of data links, diagnostics or sensors. In parallel to these radiation hardening studies, it was discovered that in some case the RIA and RIE effects, that negatively impact most of the applications, could be used to design innovative radiation sensor, active (*online measurement*) or passive (*post-irradiation measurement*), point or distributed, very efficient to monitor the harsh environments in which the fibers are installed.

1.1.1.1 Radiation-material interaction and related phenomena

When the light propagates in a medium, it interacts with its constituents (atoms and molecules). If the wavelength of the travelling light is far from the intrinsic resonance of the medium, the electric field induces a time-dependent polarization dipole in the medium. The inducted dipole generates a secondary electromagnetic (EM) wave that is the so-called “Rayleigh-scattered

light”. The addition of the scattering fields gives the resulting scattered light intensity. In a perfectly homogeneous medium, the phase relationship of the emitted wave only allows the forward scattered beam. But, as OFs are not a homogeneous medium, the randomly ordered molecules and dopants create localized variations in density. Latter given rise to Rayleigh scattering which causes attenuation of the forward propagating signal proportional to $1/\lambda^4$. Then, Rayleigh losses is larger at shorter wavelengths and responsible for a backward propagating light. It is worth to note that the Rayleigh-associated optical losses are intrinsic to the fiber type and then it sets its ultimate lower limit of attenuation (*close to 0.16 dB/km at 1550 nm in pure-silica core fiber*). Rayleigh scattering is a linear and elastic scattering process. That means that the scattered power is proportional the incident one and that no energy is transferred to the medium. By definition, no frequency shift is observed between the incident and scattered light signals.

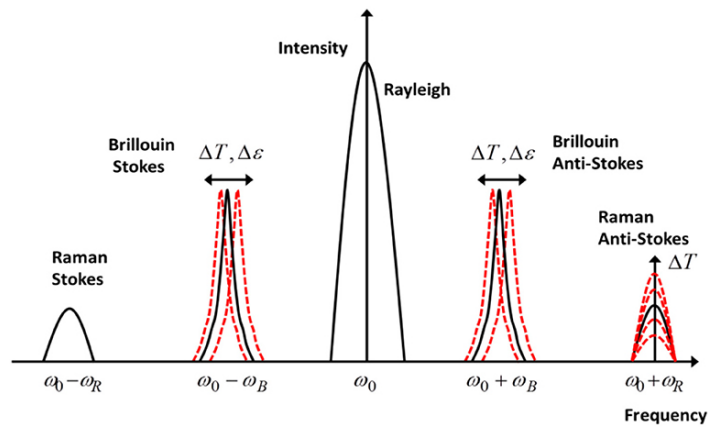


Figure 1.2 Brillouin, Raman and Rayleigh scattering phenomena exploited in various architectures of distributed optical fiber temperature or strain sensors.

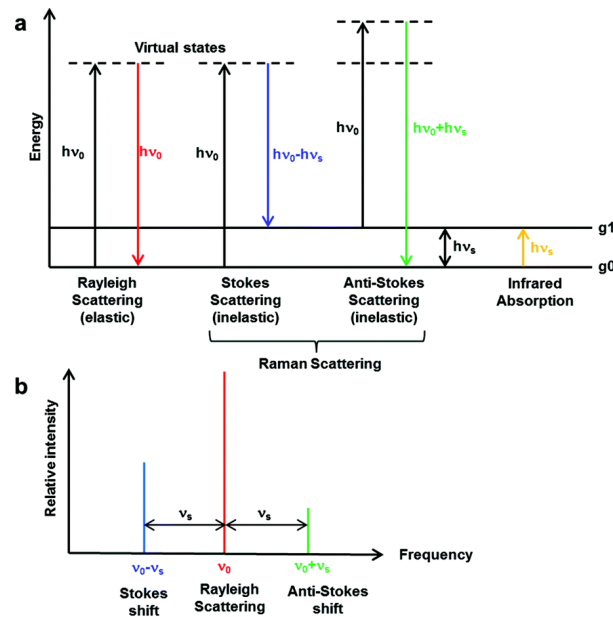


Figure 1.3 In a) we report a simplified representation of the energy levels involved in the scattering processes. In Rayleigh scattering emitted photons have the same energy of absorbed ones (elastic), in Stokes scattering emitted photons have a lower energy while in anti-Stokes scattering energy is higher (inelastic). In b) a schematic representation of the frequency shift due to the various types of scattering.

In addition to the Rayleigh scattering, two other scattering processes occur when light interacts with matter. The three processes are depicted in Figure 1.2 and Figure 1.3, their main features are briefly summarized below:

- **Rayleigh scattering** is an elastic backscatter process with no frequency shift, the pulse spectral width is in the range of MHz; it stems from the local variation of the medium density.
- **Brillouin scattering** is an inelastic backscattering process with frequency shift in the range of GHz; it stems from interaction of light with the sound waves or the acoustic phonons of the medium.
- **Raman scattering** is an inelastic backscattering process with frequency shift in the range of THz; it stems from interaction of light with the molecular vibrations and rotations in the medium.

As long as the input light is scattered without strongly altering the property of the medium, the scattering is considered to occur in the spontaneous regime. When the light intensity increases to a level such that it modifies the optical properties of the medium, the scattered light becomes proportional to the power of the input light and this regime becomes stimulated.

While at macroscopic level the charge of matter is neutral, at microscopic level the situation is quite different. At molecular dimensions there is an EM field related to the readjustment of molecular electron clouds. So, we would observe local charge density small-scale fluctuation. Without external input, such as the incident light, such short-range fluctuations would not produce measurable macroscopic effects at a far distance, as they are mutually incoherent and thus cancelled out. However, if an external light is injected into the fiber, the electric field \mathbf{E} redirects the originally inconsistent randomly fluctuating molecular clouds so as to generate a collective response on a small spatial scale. This response covers a small fraction of the EM field wavelength of the injected light, is proportional to the EM field and its macroscopic effect is called polarization \mathbf{P} :

$$\mathbf{P} = \epsilon_0 \chi \mathbf{E} \quad (1.1)$$

Where χ is the electric susceptibility, defined as $\chi = (\epsilon_r - 1)$, is a material status dependent quantity characterizing the collective response. ϵ_0 and ϵ_r are the *electric permittivity of free space* and *relative permittivity*, respectively. The susceptibility χ possesses a randomly fluctuating contribution. This fluctuating dielectric parameter gives a fluctuating polarization-induced light emission in all directions as illustrated in the Figure 1.4. Some of the scattered Rayleigh light is re-captured by the waveguide and sent in the backward direction. This backward propagating Rayleigh scattered light has a time delay that can be used for distributed sensing.

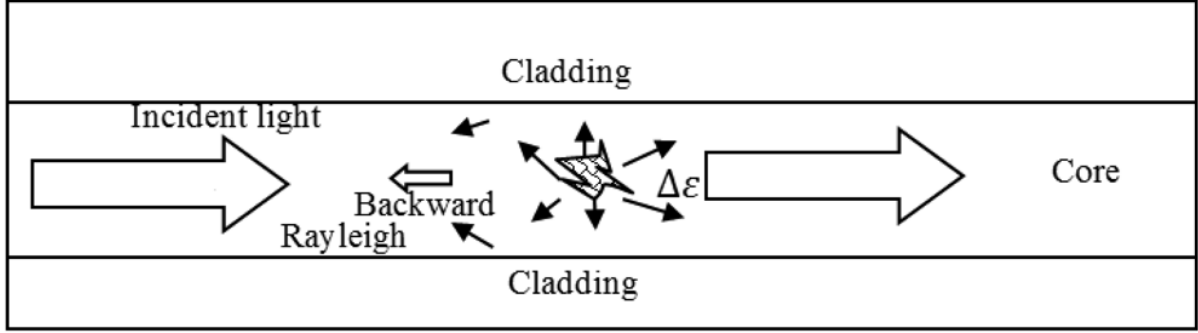


Figure 1.4 Simplified representation of Rayleigh scattering process in OF [12].

Since OF are dielectric materials, we assume a simple linearity relationship between the polarization and the electric external field. The electric displacement field vector \mathbf{D} is written as [12]:

$$\mathbf{D} = \epsilon_0(1 + \chi)\mathbf{E} = (\epsilon + \Delta\epsilon)\mathbf{E} \quad (1.2)$$

$\Delta\epsilon$ describes the local fluctuations that give rise to the spontaneous scattering, while ϵ is a constant. Applying Maxwell's equations we can write the electric field equation as:

$$\mu_0\epsilon \frac{\partial^2 \mathbf{E}}{\partial t^2} - \nabla^2 \mathbf{E} - \nabla[\mathbf{E} \cdot \nabla \ln(\epsilon + \Delta\epsilon)] + \mu_0 \frac{\partial^2 (\Delta\epsilon \mathbf{E})}{\partial t^2} \quad (1.3)$$

The first two terms represent the ordinary coherent propagation process, while the last two terms describe the random spontaneous scattering terms caused by the spatial and time fluctuations $\Delta\epsilon$. For the Rayleigh scattering we can assume only a spatial variation to $\Delta\epsilon$, and then the equation is simplified as follow:

$$\nabla^2 \mathbf{E} + \nabla[\mathbf{E} \cdot \nabla \ln(\epsilon + \Delta\epsilon)] + \mu_0\epsilon\omega^2 \left(1 + \frac{\Delta\epsilon}{\epsilon}\right) \mathbf{E} = 0 \quad (1.4)$$

where we replace the partial time derivation $\partial/\partial t \rightarrow -i\omega$ assuming a time variation for the \mathbf{E} field of type $e^{-i\omega t}$.

For the case of OFs, we can make two other hypotheses to simplify this equation: we could consider only the longitudinal dependence on z and we can make the transverse wave approximation. We then obtain:

$$\frac{\partial^2 \mathbf{E}}{\partial z^2} + \mu_0 \epsilon \omega^2 \left(1 + \frac{\Delta\epsilon(z)}{\epsilon}\right) \mathbf{E} = 0 \quad (1.5)$$

Equation above can be viewed as a scalar differential equation of the following type:

$$\frac{\partial^2 E}{\partial z^2} + \beta^2 \left(1 + \frac{\Delta\epsilon(z)}{\epsilon}\right) E = 0 \quad (1.6)$$

Above we defined the propagation constant (the wave number in the waveguide) as $\beta = \omega\sqrt{\mu_0\epsilon}$ and $\Delta\epsilon(z)$ is the variation of the permittivity of the OF core as a function of distance along the core radius. One could propose the following solution [13]:

$$E = E_0 e^{i\beta z} + \Psi(z, \beta) e^{-i\beta z} \quad (1.7)$$

where E_0 is the constant amplitude of the forward-traveling wave and $\Psi(z, \beta)$ is the spatially varying amplitude of the backward-traveling wave. The differential equation for a backward scattered wave is then:

$$\frac{\partial^2 \Psi}{\partial z^2} - 2i\beta \frac{\partial \Psi}{\partial z} + \beta^2 \left(\frac{\Delta\epsilon(z)}{\epsilon}\right) E_0 e^{i\beta z} + \beta^2 \left(\frac{\Delta\epsilon(z)}{\epsilon}\right) \Psi = 0 \quad (1.8)$$

Neglecting the second order derivative and the last term (i.e., $|\Psi| \ll E_0$), we can find an approximate solution for the backward scattered Rayleigh light due to the random spatial variation of the permittivity:

$$\Psi(d, \beta) - \Psi(0, \beta) \approx \frac{\beta E_0}{2i} \int_0^d \frac{\Delta\epsilon(\zeta)}{\epsilon} e^{2i\beta\zeta} d\zeta \quad (1.9)$$

Usually, the detected signal is $\Psi(0, \beta)$ which is seen to be related to the end face reflection amplitude, $\Psi(d, \beta)$. This relation tells us that the complex amplitude of the Rayleigh backscattered signal from a random fluctuation in the permittivity as a function of distance is

the Fourier transform of the permittivity evaluated at twice the spatial frequency (wavenumber) of the exciting field.

1.1.1.2 Influence of the OF guiding properties

Silica-based OFs are cylindrical dielectric waveguides that can transport optical energy and information. There exist different classes of OFs varying in terms of mechanisms allowing the light guidance: Total Internal Reflection (TIR) based OFs, photonic bandgap fiber (PBGF)... In this PhD, we focused on the fibers exploiting the TIR mechanisms that are the ones exploited today for dosimetry application. These fibers have a central core surrounded by a concentric cladding with a slightly lower refractive index. This difference in RI allows the light guidance inside the fiber and the signal propagation down its length. Since the core has a higher index of refraction than the cladding, light will be confined into it if the angular condition for TIR is met. To find this condition one use the Snell's law for two media with RI n_1 (n_{core}) > n_2 ($n_{cladding}$), :

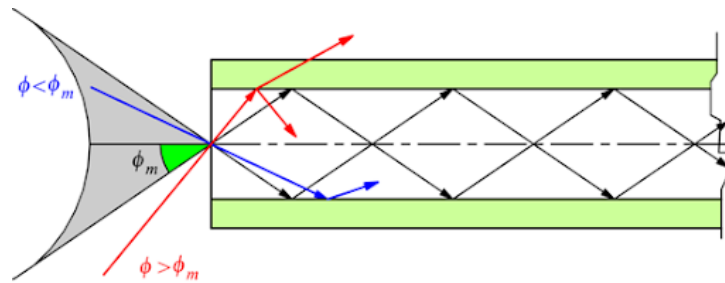


Figure 1.5 Schematic representation of the light transmission into an OF.

$$n_1 \sin \Phi_1 = n_2 \sin \Phi_2 \quad (1.10)$$

In which Φ_1 is the angle of incidence at the interface between the two media and Φ_2 the refraction angle. We defined Φ_m as the *acceptance angle*, the critical-angle to have a total reflection at the core-cladding interface and then to guide the light. If we consider the RI of the air equal to 1 we can define the *Numerical Aperture (NA)*:

$$NA = \sin \Phi_m \quad (1.11)$$

The Numerical Aperture (NA) of a fiber is defined as the sine of the largest angle an incident ray can have to ensure its total internal reflectance at the core-cladding interface. Rays launched outside the angle specified by a fiber's NA will excite cladding radiation modes compromising the OF's transmission performances. Qualitatively, NA is a measure of the light gathering ability of an OF. It also indicates how easy it is to couple light into a given fiber structure.

It is useful to introduce the dimensionless *normalized frequency* V ,

$$V = \frac{\pi d}{\lambda} \sqrt{n_1^2 - n_2^2} = \frac{\pi d}{\lambda} NA \quad (1.12)$$

It is worth pointing out that a unique parameter V gathers all of the experimental parameters characterizing the waveguide (thickness d , refractive indices n_1 and n_2) as well as the vacuum wavelength of the optical wave. The number of modes can be roughly calculated as of V :

- For Step Index OF $\rightarrow N = \frac{V^2}{2}$
- For Graded Index OF $\rightarrow N = \frac{V^2}{4}$

The geometry and composition (through the refractive index) of the OFs determine the discrete set of electromagnetic fields, or fiber modes, which can propagate in the OF.

- To attain a more detailed understanding of the optical power propagation mechanism in a fiber, it is necessary to solve Maxwell's equations subject to the boundary conditions at the interface between the core and the cladding.
- The core-cladding boundary conditions lead to a coupling between the electric and magnetic field components. This gives rise to hybrid modes.
- With the assumption $n_1 - n_2 \ll 1$ (*weak guidance approximation*), only four field components need to be considered and their expressions become simpler. The field components

are called *Linearly Polarized* (LP) modes and are labeled LP_{jm} where j and m are integers designating mode solutions. In the real cases, the RI in the core is not uniform and we can describe the variation of the squared refractive index as:

$$n^2(x, y) = n_2^2[1 + 2\Delta \cdot f(x, y)] \quad \text{with} \quad \Delta = \frac{n_1^2 - n_2^2}{n_2^2} \quad (1.13)$$

Where Δ is called the guidance parameter of the fiber and $f(x, y)$ is a normalized function that describes the shape of the refractive index variations.

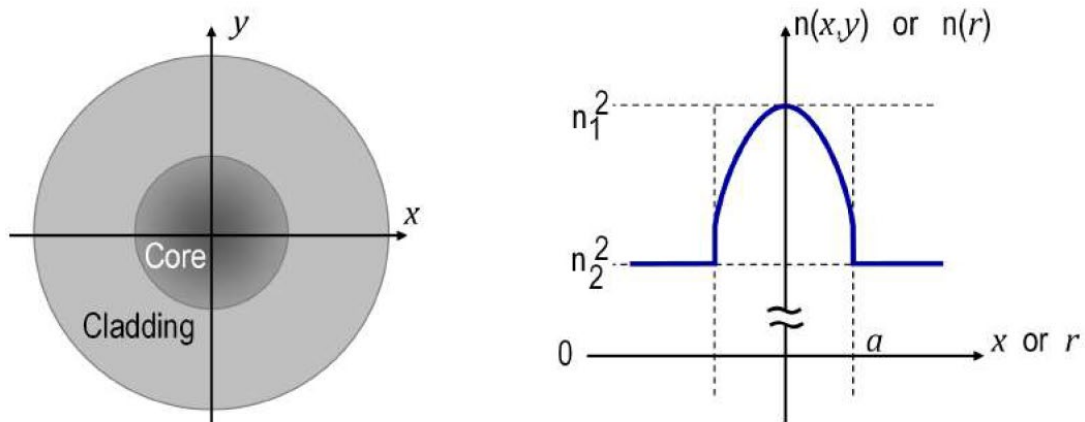


Figure 1.6 Schematic representation of the cross-section of an optical fibre and an example of a core-cladding refractive index profile.

For the step-index OFs the refractive index takes two discrete values: n_2 in the cladding and n_1 in the core, which greatly simplify the equations.

The weak guidance approximation concerns the condition $\Delta \ll 1$ i.e. when the 1st-order perturbation terms in (1.13) may be neglected. Physical meaning is that the guidance is a balance between (i) the effect of the index inhomogeneity that forms the waveguide and (ii) the natural (free-space) diffraction of the mode caused by its limited size.

Under these conditions, the propagation equations for the normal mode [14] simplify considerably and may be written, in each individual medium of refractive index n_i as:

- two Transverse Vector Propagation Equations:

$$(\nabla_T^2 + k_0^2 n_i^2 - \beta^2) \mathbf{E}_T = \mathbf{0} \quad (\nabla_T^2 + k_0^2 n_i^2 - \beta^2) \mathbf{H}_T = \mathbf{0} \quad (1.14)$$

- two Longitudinal Scalar Propagation Equations:

$$(\nabla_T^2 + k_0^2 n_i^2 - \beta^2) E_z = 0 \quad (\nabla_T^2 + k_0^2 n_i^2 - \beta^2) H_z = 0 \quad (1.15)$$

Where $\beta = \omega^2 / c^2 n^2(x, y)$ is the *dispersion relation* and $k_0 = \omega / c$ is the *propagation constant* of the field in vacuum. β describes the phase evolution of the field along the propagation direction z exactly as k_z , the wave vector along z , describes the field of a plane wave directed along z in a medium of index n . The concept of the effective index is closely linked to k by the relation: $n_{eff} = \beta / \omega / c = \beta / k_0$.

The boundary conditions of the weak guide approximation to describe step-index waveguides are field continuity and normal field derivative continuity at the core-cladding intersection.

Under these conditions, the electric field is governed by the vector propagation equation

$$(\nabla_T^2 + k_0^2 n_i^2 - \beta^2) \mathbf{E}_T = \mathbf{0} \quad (1.16)$$

In Cartesian system of coordinates, this leads to two identical and uncoupled equations for the components of the field:

$$(\nabla_T^2 + k_0^2 n_i^2 - \beta^2) E_x = 0 \quad (\nabla_T^2 + k_0^2 n_i^2 - \beta^2) E_y = 0 \quad (1.17)$$

Therefore, the transverse electric field may be written as:

$$\mathbf{E}_T = \psi(x, y) \exp(\pm i\beta z) \mathbf{u}_T \quad (1.18)$$

where \mathbf{u}_T is a unit transverse vector of arbitrary but constant direction. The scalar amplitude $\psi(x, y)$ is defined by the scalar wave equation:

$$(\nabla_T^2 + k_0^2 n_i^2 - \beta^2)\psi(x, y) \cong 0 \quad (1.19)$$

And the transverse magnetic field is obtained as:

$$\mathbf{H}_T = \psi(x, y) \exp(\pm i\beta z) (\mathbf{u}_z \times \mathbf{u}_T) n \sqrt{\frac{\epsilon_0}{\mu_0}} \quad (1.20)$$

From the shapes of \mathbf{E}_T and \mathbf{H}_T it appears that, in the weak guidance approximation, the guided modes of a fiber have a uniform polarization. As introduced, these linearly polarized modes are called LP modes. They are twice degenerate: each solution $\psi(x, y)$ corresponds to two orthogonal linear polarizations.

After the general introduction we can now derive the solutions for the optical propagation mode in OF under the weak guidance approximation. Writing the guided electric field of a mode as:

$$\mathbf{E}(x, y, z, t) = \psi(x, y) \exp(\pm i\beta z) \exp(-i\omega t) \mathbf{u}_T$$

Remembering that its propagation is governed by (1.19) and using the appropriate cylindrical coordinates, given the geometry of the fibers:

$$\left\{ \frac{\partial^2}{\partial r^2} + \frac{1}{r} \frac{\partial}{\partial r} + \frac{1}{r^2} \frac{\partial^2}{\partial \varphi^2} + [k_0^2 n^2(r) - \beta^2] \right\} \psi(r, \varphi) = 0 \quad (1.21)$$

Writing this equation we are taking into account that the refractive index varies only with r . We can manage the equation to find a separable variables solution

$$\psi(r, \varphi) = R(r)\Phi(\varphi) \quad (1.22)$$

and after a few simple steps we find:

$$\left\{ \frac{r^2}{R} \frac{d^2 R}{dr^2} + \frac{r}{R} \frac{dR}{dr} + r^2 [k_0^2 n^2(r) - \beta^2] \right\} = -\frac{1}{\Phi} \frac{d^2 \Phi}{d\varphi^2} \quad (1.23)$$

where the left side is a function of only r (*radial part*) and the right side depends only on φ (*azimuthal part*), so we can split the equation in two new equations independent on φ and r respectively.

For the Azimuthal part we must impose the condition:

$$\frac{1}{\Phi} \frac{d^2\Phi}{d\varphi^2} = \text{constant} \quad (1.24)$$

$\Phi(\varphi)$ must have a period of 2π or $2\pi/N$. Since the constant is related to a second derivative, we write it as:

$$\frac{1}{\Phi} \frac{d^2\Phi}{d\varphi^2} = l^2 \quad \rightarrow \quad \frac{d^2\Phi}{d\varphi^2} = \Phi l^2 \quad (1.25)$$

i.e., that solutions are combinations of $e^{\pm l\varphi}$, and thus, due to periodicity, l is an integer, taken as positive. For $l \geq 1$ we find two independent solutions that we can write in the form of sin and cos and for each one of them, two orthogonal polarization states are possible (modes fourfold degenerate). For $l = 0$ the only solution is $\Phi(\varphi) = 1$ and the mode is twofold degenerate. Once l has been determined, the left-hand side provides the radial variations of the field:

$$\frac{r^2}{R} \frac{d^2R}{dr^2} + \frac{r}{R} \frac{dR}{dr} + r^2[k_0^2 n^2(r) - \beta^2] = l^2 \quad (1.26)$$

To find the solutions of the $R(r)$ function for each value of l this equation has to be solved. From now on we will be indicating with the letter a the radius of the fiber core. One way to do this is to normalize the equation by introducing some concepts, some of which are already known:

- $V = k_0 a \sqrt{n_{core}^2 - n_{cladding}^2}$ normalized frequency

- $\alpha^2 = k_0^2 n_{core}^2 - \beta^2$ transverse propagation constant in the core
- $\kappa^2 = \beta^2 - k_0^2 n_{cladding}^2$ transverse propagation constant in the cladding
- $u = \alpha a$ $v = \kappa a$ and $u^2 + v^2 = V^2$ normalized values

Applying these normalized variables to the previous equation we find:

$$0 \leq r \leq a \quad r^2 \frac{d^2 R}{dr^2} + r \frac{dR}{dr} + \left(u^2 \frac{r^2}{a^2} - l^2 \right) R = 0 \quad (1.27)$$

$$r \geq a \quad r^2 \frac{d^2 R}{dr^2} + r \frac{dR}{dr} + \left(v^2 \frac{r^2}{a^2} - l^2 \right) R = 0 \quad (1.28)$$

whose solutions are the functions of Bessel.

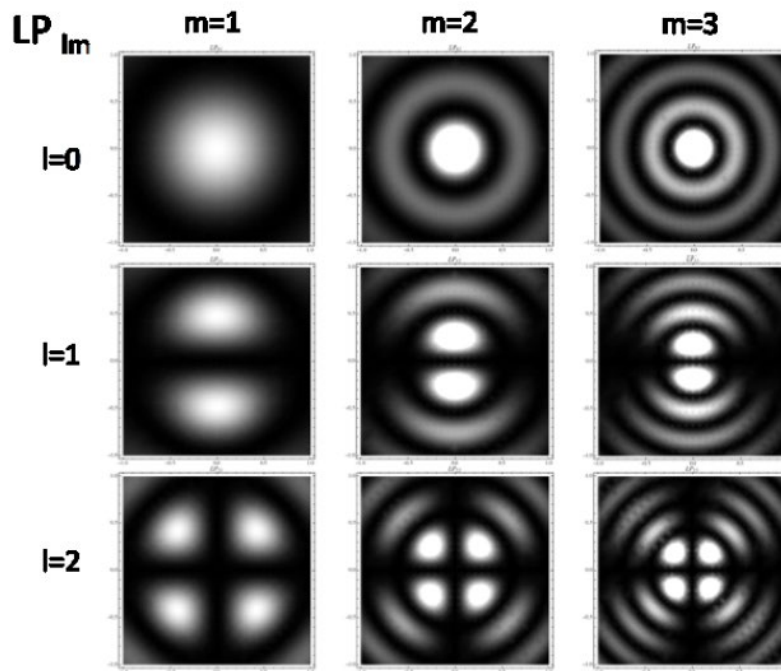


Figure 1.7 Intensity distribution of the LP_{lm} modes in OFs [15].

We will not detail the solutions of Bessel's functions because they are quite complicated and not useful for our purposes, but we only show a graphic representation of some of them to have an idea of their behaviour and to highlight the ones ($J_1(x)$) able to physically reproduce the

guided wave in the fiber core and those ($K_l(x)$) representing efficiently the evanescent part of the guided modes in the fiber cladding

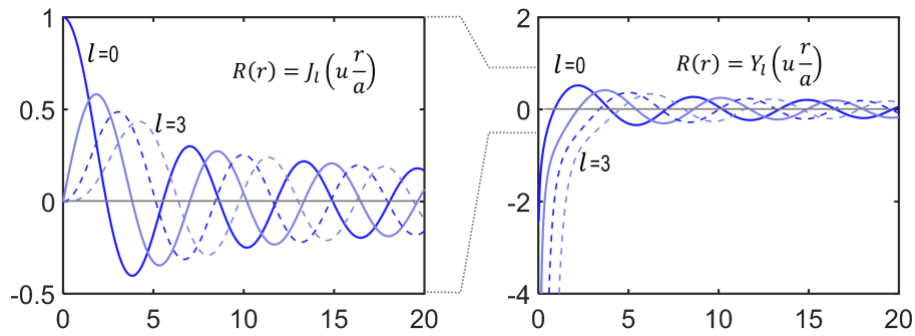


Figure 1.8 Variations of the Bessel functions of the first and second kind $J_l(r)$ and $Y_l(r)$ for $l = 0$ to 3 in the core region.

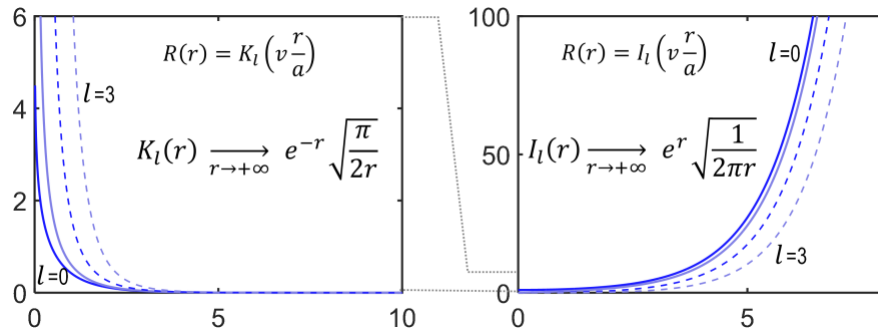


Figure 1.9 Modified Bessel functions of the 2nd kind $K_l(r)$ and of the 1st kind $I_l(r)$ for $l = 0$ to 3 in the cladding [15].

At this point, introducing the continuity of Φ and of the normal derivative of Φ at $r = a$, we can write the dispersion relation for the LP modes equation which holds for all l [16].

$$\frac{J_l(u)}{u J_{l\pm 1}(u)} = \frac{K_l(v)}{v K_{l\pm 1}(v)} \quad (1.29)$$

From this equation and the definition of the newly normalized parameters it is possible to find the number of allowed guided modes in the chosen fiber structures: for each value of l , the equation provides m possible values for b and this number m is a function of parameter V . Here

$$b \text{ is the longitudinal propagation constant given by: } b = \frac{(\beta^2/k_0^2) - n_{cladding}^2}{n_{core}^2 - n_{cladding}^2}$$

We refer to guiding modes as LP_{lm} :

- l is the index of the Bessel function. It characterizes the periodicity of the azimuthal distribution $\Phi(\varphi)$. When $l = 0$ there is no azimuthal variation i.e. the amplitude is unchanged by a 2π rotation at constant r . When $l = 1$, one dark radial fringe crosses the field, i.e. the amplitude goes twice to 0 along a 2π rotation at constant r . For any other value of l , l dark radial fringes cross the field, i.e. the amplitude goes $2l$ times to 0 along a 2π rotation at constant r .
- m is the number of extrema in the radial oscillations of the Bessel function.

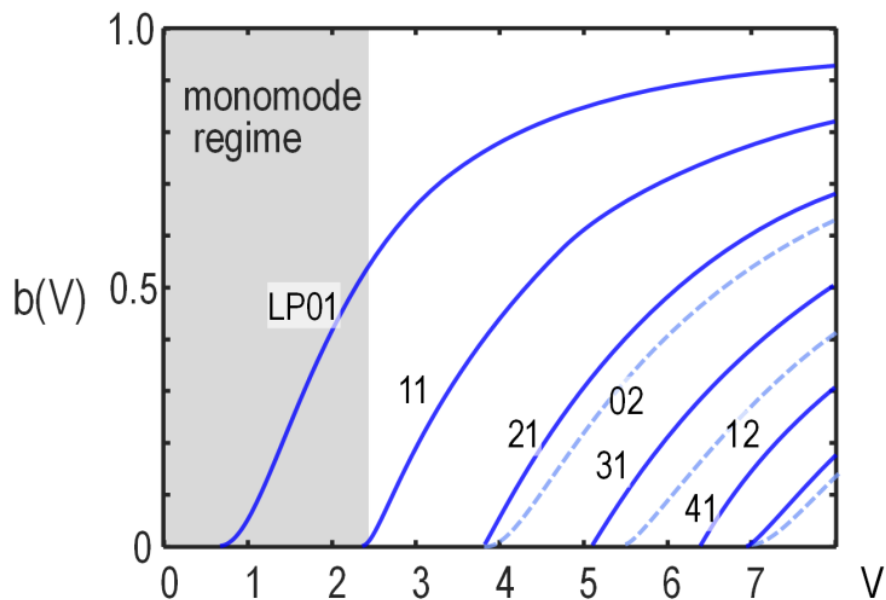


Figure 1.10 The first LP_{lm} modes $b(V)$, i.e. normalized dispersion. Full lines: $m = 0$ modes; lighter dashed lines $m = 1$ modes [15]

The graph of $b(V)$ shows that for $V < 2.405$, LP_{01} is the only mode that propagates. In a SMOFs only the fundamental mode (noted as LP_{01}) is guided for wavelengths above the cutoff one. LP_{01} always exists and possesses no cut-off frequency. $V = 2.405$ is the normalized cut-off frequency of the LP_{11} mode. The number of guided modes supported by the fiber increases stepwise with increasing values of V (so decreasing values of the wavelength).

Most of the LP_{01} mode power remains confined in the core but an evanescent part of the wave is travelling in the fiber cladding [17,18]. The fraction of light power propagating inside the core (also defined as the *Confinement Factor, CF*) is wavelength dependent, increasing at decreasing wavelengths in the single-mode regime. Even if the modes are guided, a part of their energy is transmitted to and guided by cladding. In addition to a finite number of guided modes, the optical fiber waveguide has an infinite continuum of radiation modes that are not trapped in the core. Some of this radiation gets trapped in the cladding causing cladding modes to appear. As the core and cladding modes propagate along the fiber, mode coupling occurs between the cladding modes and the higher-order core modes. This generally results in a loss of power from the core modes. In addition to bound and radiated modes, a third category of modes, called leaky modes [19], is present in optical fibers. Leaky modes are only partially confined to the core region, and attenuate by continuously radiating their power out of the core as they propagate along the fiber. This power radiation out of the waveguide results from a quantum mechanical phenomenon close to the one known as the tunnel effect [20].

- A mode remains guided as long as the condition $n_2k < \beta < n_1k$, where $k=2\pi/\lambda$, is satisfied.
- The boundary between truly guided mode and leaky modes is defined via the *cutoff* condition $\beta = n_2k$.
- As soon as β becomes smaller than n_2k , power leaks out of the core into the cladding region.

$$CF = \frac{\int_0^{2\pi} \int_0^{R_{core}} ||E_{LP_{01}}||^2 r d\theta dr}{\int_0^{2\pi} \int_0^{R_{fiber}} ||E_{LP_{01}}||^2 r d\theta dr} \quad (1.30)$$

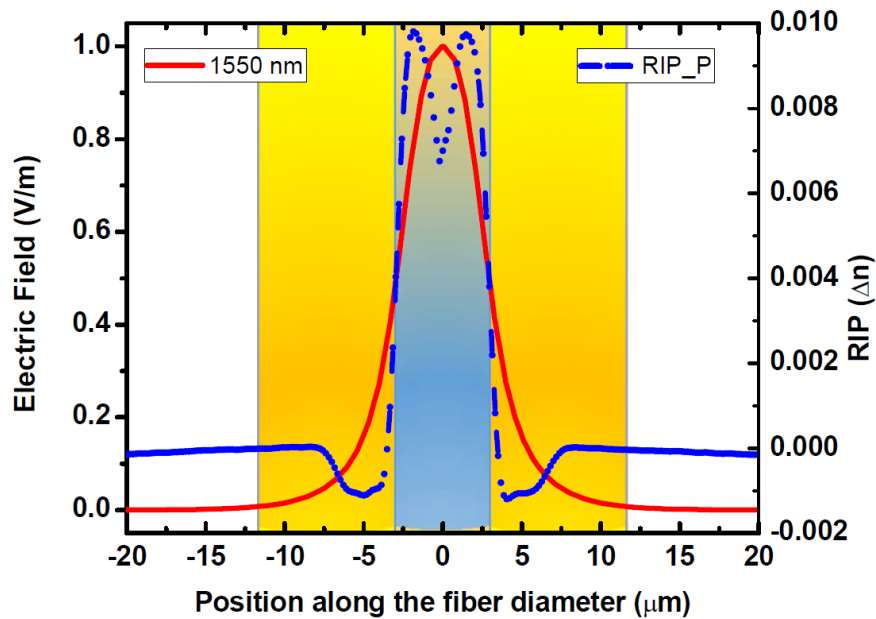


Figure 1.11 Distribution of the power of fundamental mode in the core 80% (central part) and in the cladding 20% (yellow parts) for the P-doped SMOF. In blue is given its measured refractive index profile (RIP).

1.1.1.3 Some notes on radiation effects in “common” passive OF types

To have a global view on the mechanisms involved in the OFs transmission degradation under irradiation, we present a brief overview of the principal point defects associated to the dopants of interest and list their associated optical properties (absorption or even luminescence). A complete and recent overview can be found in [21]. These point defects will drive the radiation response of OFs and explain that differently doped fibers can have very diverse radiation behaviors. As phosphosilicate glasses are intrinsically (before irradiation) more transparent in the ultraviolet (UV) than Ge-doped optical fibers, P-doped fibers could be adapted for some specific applications needing to operate in the 300 nm – 2 μm spectral domain. As an example, P-doped fibers have been designed for the laser diagnostics of megajoule class lasers that are working at 351 nm [22,23].

1.1.2 Radiation effects on P, P₂O₅ doped fibers

The *Continuous Random Network* model, proposed by Zacharias was the first model describing the structural properties of amorphous silica [24] assuming that discrete crystallites do not occur in simple glasses, but that there are spatial fluctuations of the degree of intermediate range order within the vitreous network. More highly ordered regions, in which the atomic arrangement approaches the ones of related crystalline materials, are interconnected by regions where the order degree is reduced [25].

Based on this model we know today that the P atoms are incorporated in the doped silica glass as phosphorus pentoxide whose stoichiometric formula is P₂O₅. In Figure 1.12, we report the sulfur dioxide structure corresponding to the one found in phosphosilicate glass.

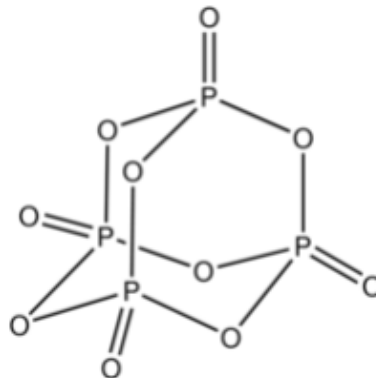


Figure 1.12 Sulphur dioxide structure, model by which the phosphorus atoms are part of the doped silica structure.

As reported in literature and interestingly for the OF production, P-doping reduces the silica melting temperature [25] and changes its viscosity. Phosphate glasses are also studied as material with interesting transmission properties in the UV [26]. One of the most remarkable applications of P-doped silica concerns the design of active OF serving to conceive optical amplifiers and lasers. These specialty OF are doped with rare-earth elements such as Erbium, Ytterbium [27] allowing to the light signal amplification through pumping at lower wavelengths. Rare-earth dopants indeed are hardly dissolved in pure silica and in order to

increase their concentration preventing the clustering of the rare-earth ions, which is very detrimental for the light amplification, aluminosilicate host-matrix is usually preferred [28,29]. However, recent findings have shown that P-doped silica is able not only to increase the solubility of rare-earth ions compared to pure silica but it can also provide a higher clustering threshold than aluminosilicate glasses [30,31]. These features are technically relevant in the case of Erbium/Ytterbium co-doping. Further studies over the last decades have shown that the P-doped OFs are very radiation sensitive, being associated with extreme RIA levels [7,32]. This high sensitivity was the first characteristic leading to new studies trying to evaluate their exact potential for use as radiation detectors or as dosimeters.

Figure 1.13 gives an overview of the main absorption bands P-related defects. It should be emphasized that these bands have been observed in either bulk glasses (or preforms) and optical fibers. From this figure, several statements can be made:

- First, most of the known P-related defects that pre-exist the irradiation or are created during exposure are associated with absorption bands peaking in the ultraviolet–visible domain, at wavelengths below 800 nm ($E > 1.55$ eV). As a general rule, the RIA levels are lower in the near-IR part of the spectrum at wavelengths above 800 nm.
- Second, the contribution of various defects to the measured RIA will also depend on their localization in the fiber cross sections and on the amount of light travelling in this region. Furthermore, the defect generation or bleaching efficiencies can be modified by other parameters such as the internal fiber stress, or through photo-bleaching effects [6].

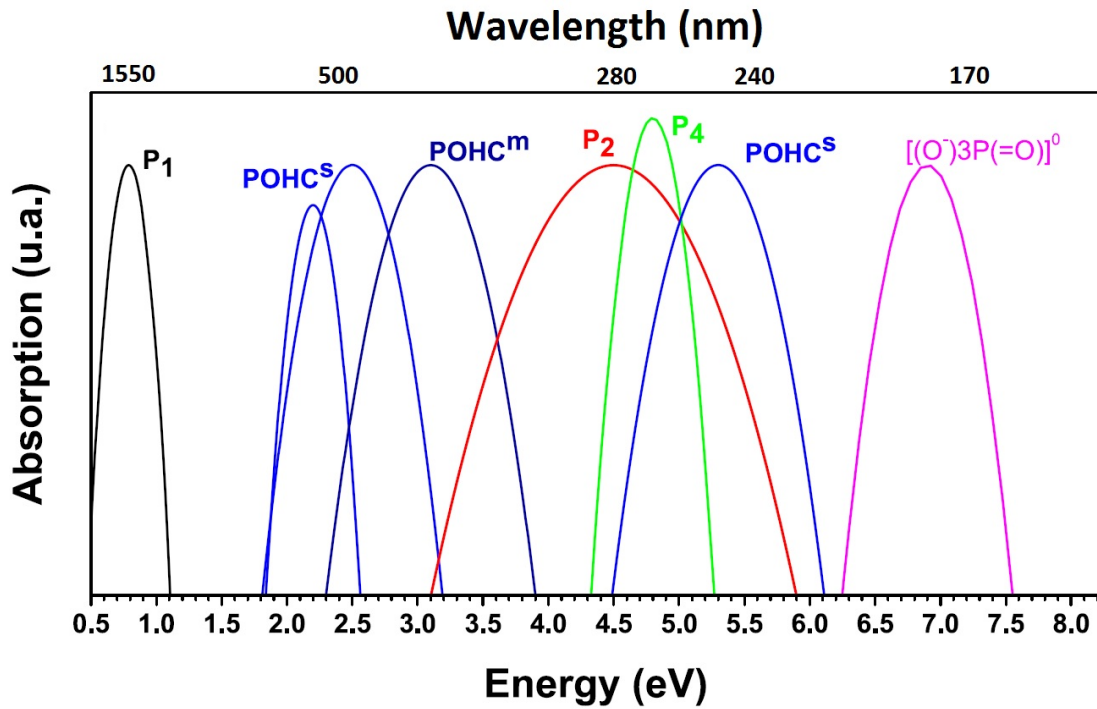


Figure 1.13 The main absorption bands associated with P-related point defect structures, adapted from [6].

The main features of the P associated defects reported by Griscom et al. [33] are hereafter listed.

- **P1 defect** consists in one P atom bonded with three oxygen atoms and with an unpaired electron located close to P. The main absorption band associated with this defect is peaked around 1600 nm (0.78 eV) which falls in the Near-Infrared (NIR), a spectral region of crucial interest for the telecommunications. The P1 defect has probably a structure comparable to the PO_3^{2-} molecular ion, and consequently P1 has been suggested to be the P analogue of the SiE' center.
- **P2 defect** consists in one P atom with an unpaired electron and four bonded oxygen bridging atoms. In the defect-free SiO_2 glass, each oxygen would bridge two SiO_4 tetrahedra. On the other hand, the ideal P_2O_5 glass would be characterized by one non-bridging and three bridging oxygen atoms per P atom (see Figure 1.12). In a SiO_2 - P_2O_5 glass, this same defect could be justly termed a “silicon-substituted phosphorus”.

Because P has a higher valence (+5) than silicon (+4), such a precursor defect would provide a coulombic trapping potential for an electron. On this basis, P2 defect has been ascribed to a silicon-substituted phosphorus which has trapped an electron.

- **P4 defect** is formed by a phosphorus atom with a lone pair attached and an unpaired electron and with two bonded oxygen atoms. In literature we find that a possible precursor of a P4 center could be a tri-coordinated P ion bonded to three bridging oxygen atoms. In this view, the formation of the P4 center would be represented as in the lower branch of Figure 1.14 by an electron trapping. The three coordinated P^{3+} precursor for the P4 defect is also particularly attractive because the same structure could give rise to the P1 center by the hole trapping as illustrated in the upper branch of Figure 1.14. Another possible precursor of the P4 is the twofold coordinated P. In this case, as reported in Figure 1.14, a hole trapping gives rise to the conversion into P4.

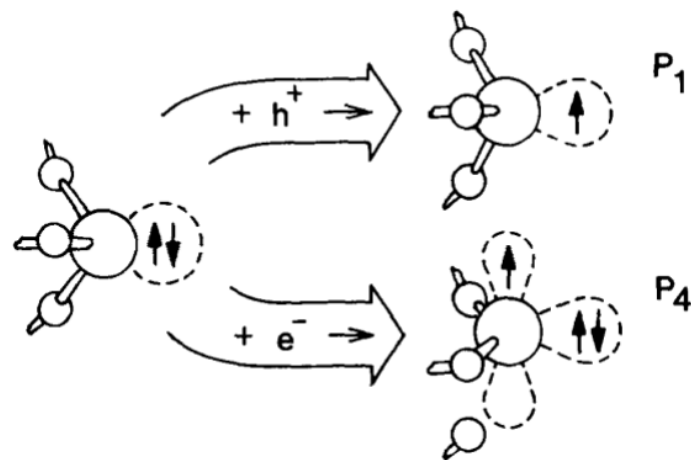


Figure 1.14 Model for the formation of the P1 and P4 centers by hole and electron trapping, respectively, at the site of a three-coordinated P^{3+} precursor structure. Adapted from ref. [33].

- **POHC** (phosphorus oxygen hole centers) defects correspond to either stable or metastable defects. Both defects are linked to P bonded to four atoms of oxygen but if the unpaired electron is located on a non-bridging oxygen we have the metastable-POHC configuration, while if the unpaired electron is shared by two non-bridging

oxygen atoms we have the stable-POHC configuration. It is worth to mention that in the original paper by Griscom et al. [33], the metastable variety of POHC was thought to be unstable at room temperature, whereas successive studies have shown that this is not the case [34]. A particularity of P1 defect is that its concentration can increase after the end of the irradiation, as it was shown that POHCs can recombine into P1 at room temperature [33].

Table 1-1 reviews the main properties of the P-related point defects. If this dopant is associated with a variety of absorbing centers, only one luminescence band around 400 nm has been attributed to a P-related species. A very complete and pioneer work basing on OA and ESR measurements on thermally-treated and irradiated samples was published by D.L. Griscom [33], recent deep theoretical and experimental investigations of the radiation effects in phosphosilicate glasses have been done by L. Giacomazzi et al. [35].


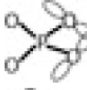
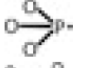



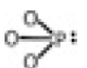

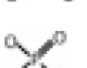



To complete the discussion on the behaviour of the P-related point defects we report the isochronal study carried out by D.L. Griscom et al. [33]. All parameters regarding the experiment can be found in the original article, and will not be reported here. Figure 1.15 reports the result of the isochronal experiment with several attractive features.

- The P1 defect grows in concentration for anneals up to ~500 K; since P1 and POHC are both trapped hole centers, it can be supposed that holes are thermally de-trapped from the relatively shallow POHC sites and largely re-trapped at P1 sites.
- The sudden onset of annealing of the P2 population above ~570 K correlates well with similar sudden decrease in P4, P1 and POHC. Since P2 is almost certainly a trapped electron center and the respective population appears to be related to the relation $[POHC]+[P1]+[P4]\sim[P2]$ at temperature below ~625 K, it can be logically suggested

that electrons thermally de-trapped from P2 recombine with trapped hole at the sites of P4, P1 and POHC.

- The observed correlation of the annealing curves for P1 and P4 in the range ~670-730 K suggests that hole may be exchanged between the two sites in this particular temperature range.

Table 1-1 Phosphorus-related point defects and their main optical characteristics. Adapted from [21].

Name	Structure	Param	OA peak eV (FWHM) eV	Oscillator strength	Note	PL peak eV (FWHM eV, lifetime RT)
m-POHC		Yes	2.2 (0,35) 2.5 (0,63)	0.5 0.5		None reported None reported
s-POHC			5.3 (0,74) 3.1 (0,73)	0.5 0.5		None reported None reported
P1		Yes	0.79 (0,29)	0.0007		None reported
P2		Yes	4.5 (1,27)	0.035		None reported
P4		Yes	4.8 (0,41)	0.014		None reported
PO2		No	> 5.5 eV	Unknown	Unknown	None reported
P ₂ O ₃		No	5.9 6.1	0.001 0.05		None reported None reported
[(O-)3-P:] ⁰			6.4	0.04		None reported
Type I PODC			8 8.43	0.3 0.2	Small cluster simulation Small cluster simulation	None reported None reported
PO ₂		No	4.7 (0,7) 6.4 (0,6)	0.002 comparable with the 4.7 PLE peak		3 (highly asymmetric; 5–6 ms) 3 (highly asymmetric; 5–6 ms)
P2O5		No	6.9 7.16	0.004–0.006 0.002		None reported None reported
[(O-)3-P=O] ⁰			7.2 6.1 6.5	0.002 0.009 0.006		None reported None reported None reported
PO3**		No	7.2 6.1 6.5	0.002 0.009 0.006		None reported None reported None reported
[(O-)2-P(=O)2] ⁰			7.2 5.1–5.4	0.009 0.001		None reported None reported
PODC II		No	6.82–6.99	0.02–0.1	Small cluster simulation	None reported

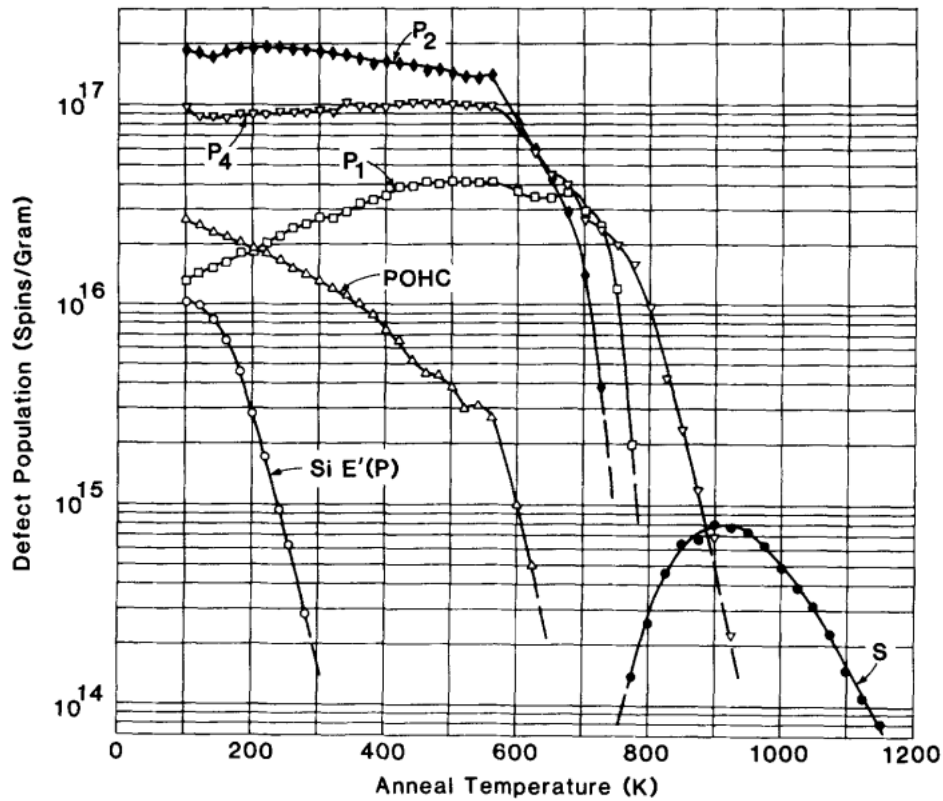
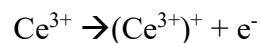


Figure 1.15 P-defects' populations versus annealing temperature for a phosphosilicate glass x-ray irradiated at 77 K and measured at 100 K following 5-min pulse anneals at the indicated temperature [33].

In recent years an element that has started to be increasingly used as a co-dopant in the fabrication of OF is cerium. Ce can be incorporated in the doped silica as Ce^{3+} or as Ce^{4+} ions [36,37]. The concentrations of the two ions are correlated to the production process and, in particular, to the oxygen presence during this process. An oxygen-rich atmosphere promotes the formation of Ce^{4+} ions while an oxygen poor one favours the Ce^{3+} ions. An important difference that distinguishes the two ions concerns their absorption properties: an absorption band peaking at 3.9 eV is associated to the Ce^{3+} ion while a band peaking at 4.8 eV is associated to Ce^{4+} ion [38]. When a Ce^{3+} ion is exposed to UV or ionizing radiation (X-rays, γ -rays, ...), it is ionized and becomes an ion $(Ce^{3+})^+$:



Furthermore, Ce^{3+} ion is an efficient luminescence center in the visible spectral domain but its luminescence decreases above a certain concentration due to the formation of clusters in the glass [39]. The peculiar role of Ce is extended to the radiation hardening of silica-based materials since by acting as a charge donor it could inhibit some of the radiation-induced processes [25,40], leading for example to lower RIA levels. This aspect is further investigated in the present work in connection to its potential interest in the design of fiber-based dosimeters.

1.1.3 Radiation effects on Al doped fibers

Aluminum, which is incorporated by substituting a silicon site, is one of the most abundant impurities in natural SiO_2 . Its incorporation results in a hole trapped on an oxygen bridging one Al atom with one Si atom leading to the Aluminum-Oxygen-Hole Center (Al-OHC), which atomic structure is defined as $[\text{AlO}_4]^0$. It is considered to be the most probable structural origin of this point defect [41].

Literature devoted to Al-related point defects remains significantly less abundant than for the other silica-associated point defects, although considerable work has been published in recent years [42]. First results have been obtained studying natural silica that contains Al impurity [43,44,45]. Only a in few cases the investigated samples have Al contents that can be compared to the doping levels used for the OF manufacturing [46,47,48,49]. As a consequence, whereas for the natural silica it is accepted that the Al can be inserted in the glass matrix replacing the Si and with an alkaline charge compensator as neighbour [44,45] in doped silica (some weight percent) this aspect still needs further investigations to be confirmed. Table 1-2 details the optical absorption bands associated with the Al-defects. As shown in Figure 1.16, this defect set is sufficient to describe the RIA measured in the UV–visible spectral range in aluminosilicate OFs. Regarding these attributions we notice that the relation between the Al-OHC and the 2.3 eV OA band is well supported by various investigations [41,45], whereas the others have still to be confirmed. As an example, there are some investigations in which the

2.3 eV OA band is clearly present in the RIA spectrum whereas the 3.2 eV seems absent or with a smaller relative amplitude [45] with respect to those observed in [41,49]. Anyway, the bands reported in Table 1-2 are not sufficient to reproduce the data from the UV to the NIR as evidenced in [49]. Recent investigations have highlighted that the Al-doped fibers are good candidates for radiation detection [46], a better understanding of the Al insertion in silica matrix as well as the properties of its related defects represents, for sure, one of the future challenges.

Table 1-2 Aluminum-related point defects: main optical characteristics and key references [41,45,50]. Adapted from [21].

Name	Structure	Param.	OA peak eV (FWHM eV)	Oscillator strength	Note	PL peak eV (FWHM eV, lifetime RT)
Al-OHC	≡Al- \dot{O} -Si≡	Yes	2.3 (0.9)	0.060	PL excited in the range 1.7–2.5	1.5–1.0 and 0.7–0.2
			3.2 (1)	0.124		Proposed by simulation
			4.9 (1.08)	0.126		Unknown
AlE'	≡Al•	Yes	4.1(1.02)	0.214		Unknown
			4.9 (1.08)	0.126		Unknown
?	?	?	Higher than 7.5 eV	Unknown	Structureless induced absorption under ArF irradiation at 80 K	Unknown
Transit ODC(II)	?	No	Excitation ArF laser	Unknown	The decrease of the 2.7 PL was attributed to the back relaxation	4–4.5 (not reported; 4.5 ns)
Modified				Unknown	of the surrounding	2.7 (not reported, 1.7 ms) [Ⓣ]

[Ⓣ] afterglow during hundreds of seconds after switching off the laser; recombination between STHS and modified ODCs(II).

From a recent deeper study [49] it was demonstrated that varying the fiber core size, its Al content, its drawing parameters, and the preform deposition process has no major impact on the RIA characteristics, at least in the investigated ranges for the above-mentioned parameters. Similarly, no specific RIA dependence on the employed dose rate is clearly observed. The RIA spectrum shape appears to be almost independent on the investigated sample and features optical bands above 2 eV.

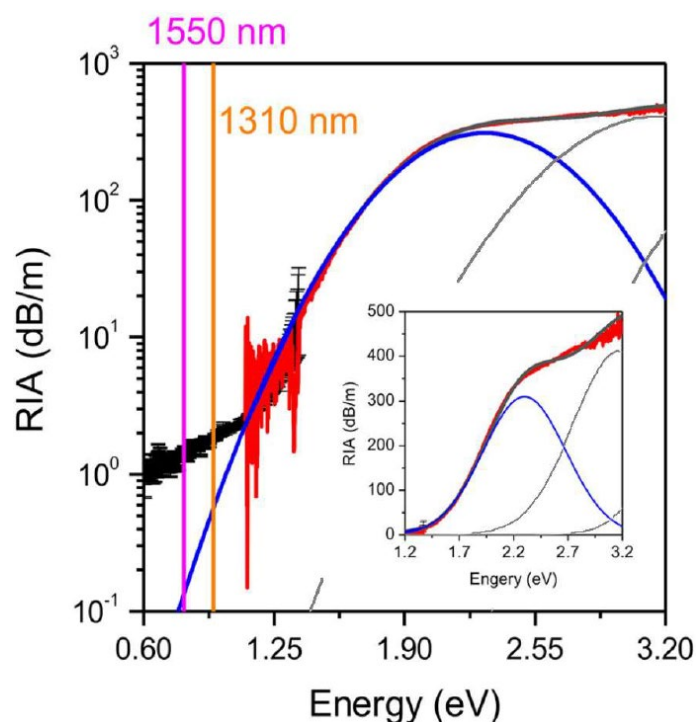


Figure 1.16 RIA spectrum recorded in the visible (—) and in the NIR (—) for the FibMM irradiated at 150 Gy (0.68 Gy s^{-1}). The Al–OHC 2.3 eV band (—), and the (—) 3.18 and 4.1 eV bands, resulting from fit of the RIA in the visible spectrum (—) are inserted. Wavelengths of interest for telecommunication are marked. The inset shows same data in linear–linear graph, from [49].

In Figure 1.16, we report the experimental data analysis from [49] that describes the RIA spectrum of an Al-doped OF. The RIA data can be reproduced using a similar set of Gaussian bands than the ones used by Hosono et al. [41]. Indeed, the two gray curves represent a 3.2 eV (FWHM of ~ 1.02 eV) and a 4.2 eV (FWHM of ~ 1 eV) bands, whereas the blue Gaussian is representative of the 2.3 eV (FWHM ~ 0.89 eV) band that was previously attributed to the Al–OHC, [41,45] also considering the data optioned for natural alpha-quartz. In this case the larger FWHM of the 4.2 eV band implies two effects: a small decrease of the 2.3 eV amplitude and a clear overestimation of the signal in the range 1–1.5 eV. Such differences can be related to the high RIA (low transmitted signal) level for energies higher than 2.8 eV, which complicates the estimation of the components at high energy, also impacting the fit quality at lower energies.

1.2 Dosimetry with optical fibers

The use of ionizing radiation for a wide range of applications has become increasingly significant in recent years. Radiation dosimetry is fundamental to these radiation processes and as such is the focus of many research activities. A number of physical and chemical sensors, which can be subdivided into liquid, solid and gaseous systems, are available to measure ionizing radiation and researchers are always looking for ways to improve their performances, to increase their sensitivities, to provide real-time measurements or significantly reduce the sensor costs. All these factors are important for providing the optimum radiation dosimeter. An optical fiber radiation dosimeter is a photonic system based on optical fiber technology, whereby radiation changes some of the characteristics of the optical signal propagating along the fiber. The optical fibers can be directly affected by the radiation and serve as the sensitive element. The sensor is then called an intrinsic sensor. In the case, the fiber is only used to transport the optical signal from an external probe, the sensor is classified as an extrinsic sensor [51]. There are several dosimetry techniques that can be applied to fiber optics to further improve the overall system, and some of these will be discussed below.

1.2.1 Radiation Induced Emission (RIE)

The Radiation Induced Emission (RIE) in OFs corresponds to the spontaneous emission of light when the material is exposed to radiation [52]. The light generated could be a combination of Cherenkov emission and Luminescence, depending of the fiber composition and irradiation characteristics. For pure-silica based OFs, the light can be generated through Cherenkov process by highly energetic radiations. So, when a fiber is installed in a harsh environment, the presence of relativistic particles passing through the fiber could generate light within the fiber core. This radiation can lie within a propagating mode in the fibre and be detected as unwanted background whose intensity depends on the angle between the beam and the fibre. RIE degrades the signal-to-noise ratio [53]. In a medium with Refractive Index (RI) n , the light emission occurs when

$n\beta > 1$, where β is the ratio between the particle's velocity and the speed of the light in vacuum. Cherenkov, as the radiation induced luminescence (RIL) lead to the generation of a parasitic signal affecting the data transfer capabilities of the fiber links. Several studies are performed to reduce or eliminate the Cherenkov's effect or RIL from the OFs installed in radiation environment to maintain high bandwidth data links [54]. In recent decades, RIL that was also seen as a promising option to build radiation detector or beam instrumentation, eg. in the medical field [55], particularly for radiology diagnostic and radiotherapy [56].

1.2.2 Optically Stimulated Luminescence (OSL)

Optical Stimulated Luminescence (OSL) is a well-known phenomenon in which an irradiated material when stimulated by an appropriate optical excitation emits a luminescence proportional to the absorbed radiation dose. When an irradiated fiber is exposed to a laser light, a luminescence can be observed. The radiation causes ionization of valence electrons and the subsequent creation of hole/electron pairs. Through non-radiative processes, the electrons and holes, generated by the irradiation, are captured by either pre-existing or radiation induced defects. Subsequent light illumination of the irradiated sample leads to absorption of energy by the trapped electrons and transitions from the localized traps into the delocalized conduction band. Recombination of the released electrons with the localized holes results in radiative emission processes, corresponding to the OSL signal. The OSL intensity depends on the dose deposited in the fiber. This principle has led to the development of dosimeters, including fiber-based, based on the physical principle of the OSL [57,58]. The advantages to develop the OSL dosimetry are:

- The optical nature of the readout process does not involve problems of blackbody radiation and thermal quenching;

- OSL also allows using low melting point dosimeter materials, namely, luminescence phosphors impregnated into a plastic matrix. Thus, robust dosimeters may be manufactured;
- The high sensitivity of OSL in some phosphors, such as $\text{Al}_2\text{O}_3:\text{C}$, also provides advantages related to multiple readings possibility;
- Readout process can be made very fast ($<1\text{s}$) through adjustment of the stimulating light intensity opening the way to a fast analysis of numerous dosimeters.

Last but not the list, the small-size optic of fiber based OSL dosimeters over the currently available radiation detectors is very interesting for medicine, as well as the possibility to combine dose measurements through OSL with real-time dose-rate evaluation through RIL [59].

1.2.3 Thermally Stimulated Luminescence (TSL)

The TSL principle is similar to that of OSL, however in the TSL case the stimulating factor is not the light injected into the fiber but the increase of its temperature.

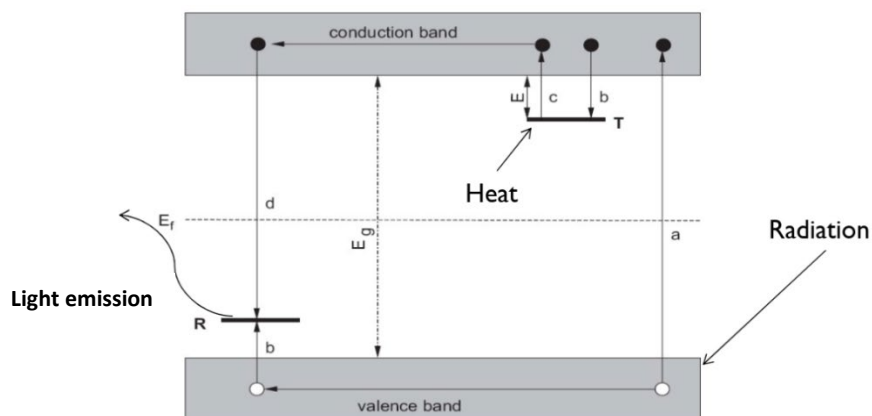


Figure 1.17 Energy band model showing the electron transition in TSL material using a simplified two-level model: (a) generation of electrons and hole; (b) electrons and hole trapping; (c) electron release due to thermal stimulation; (d) recombination. Solid circles are electrons, open circles are holes. Level T is an electron trap, level R is a recombination center, E_f is Fermi levels and E_R is the energy band gap.

In an OF, the primary interactions of photons or charged particles with the silica-based materials release numerous low-energy-free electrons and holes through ionization. These free carriers can either recombine or become trapped at electron or hole traps, respectively. In general, two types of traps are known: storage traps and recombination centres. A storage trap localizes free charge carriers and releases them during the subsequent heating, resulting in the TL process, or irradiation with light, resulting in the OSL process. A charge carrier released from a storage trap may recombine with a trapped charge carrier of opposite sign at a recombination (luminescence) center. The recombination energy is always partially emitted in the form of light that can be measured with photodiodes or photomultiplier tubes. The TSL intensity emission depends on the temperature: keeping the heating rate constant makes the temperature proportionally increasing with time and so the TSL intensity can be plotted as a function of time. The resulting curve is called glow curve [60]. The peaks in the glow curve may be correlated with trap depths responsible for TSL emission [61]. The use of TSL as a method for radiation dosimetry of ionizing radiation has been established for many decades and has found many useful applications in various fields, such as personnel and environmental monitoring, medical dosimetry, archaeological and geological dating, space dosimetry. Optical fibers, especially germanosilicate optical fibers, have been shown to be very efficient materials for TL-based dosimetry.

1.2.4 Radiation Induced Attenuation RIA

Radiation Induced Attenuation (RIA) corresponds to an increase of the fiber attenuation when exposed to radiation. RIA levels and kinetics depend on many parameters that we can collect in three groups: *radiation constraints*, *fiber profile of use* and *fiber characteristics*.

Radiation constraints are the nature of particles (x-ray, γ -ray, protons, neutrons), dose (fluence) [62], dose-rate (flux) [63,64] and the temperature [65,66]; *fiber profile of use* concerns operating wavelength [67], injected power [42] and the application purpose (data transfer,

sensing or diagnostics); *fiber characteristics* are the core and cladding composition [7,32], manufacturing process (stoichiometry, drawing parameters) [68,69,70], optogeometric parameters [71], nature of coating [21] and light guiding properties [46].

From the definition of Lambert-Beer law, the RIA can be calculated as:

$$\alpha_{RIA} \left(\frac{dB}{m} \right) = \frac{10}{L(m)} \cdot \log \frac{I}{I_0}$$

where I and I_0 are the intensities of the transmitted signal at a given time and before irradiation starts, respectively.

One of the main difficulties regarding the radiation vulnerability study of optical fibers concerns the representability of the available irradiation facilities to reproduce the constraints associated with the targeted environments. This is particularly true for space but even for new facilities or industries with environments (*dose, dose rate, temperature*) not covered by the existing radiation test facilities. The accessible accelerated results have to be associated with models that allow the expected fiber degradation to be extrapolated in the application conditions from the radiation data test. Today, several empirical or semi-empirical models have been developed to predict the growth and decay kinetics of RIA versus the dose or time after irradiation based on a limited set of radiation test results on the chosen OF. For an in-depth look at the RIA models developed over time, see the following works [67,72,73,74,75,76,77,78].

If for most applications RIA is a limiting issue that has to be mitigated, it should be noted that monitoring it in a radiation-sensitive optical fiber can be exploited for radiation detection and dosimetry applications, both pointwise and distributed, for example at the DESY facility in Germany [79] and more recently at CERN in Geneva [80,81,82,83].

1.3 CERN needs and selection of RIA-based dosimeter for the study

The CERN - *European Organization for Nuclear Research* - is the largest laboratory in the world for the high-energy physics studies. The most powerful particle accelerator called LHC (Large Hadron Collider) is active since 2008, in the last years CERN researchers have obtained the world record of 7 TeV collision energy and during LS2 (Long Shutdown 2) the machine upgrade for the new HL-LHC project has started to reach even higher energies. In order to monitor radiation levels and predict equipment and material lifetimes present in high energy accelerators and physics experiments, an accurate radiation dosimetry is highly important and very challenging due to the large areas which need to be monitored and the extended dose range of interest. Not only in the LHC, but also in the injection chain accelerators, it is critical to monitor radiation losses due to machine operation.

In general, radiation fields in the injection chain originate from a combination of the interactions between the beam and the residual gas elements inside the beam pipe and the beam-machine interactions in correspondence with specific machine elements (e.g. collimators). In LHC radiation fields originate from these two phenomena plus the production of secondary remnants of beam-beam collisions, typically relevant in the vicinity of the experimental areas.

Part of the purpose of the currently installed point radiation detecting systems (radio-photoluminescence (RPL), Beam loss monitor (BLM), Radiation sensitive Field Effect Transistors (RadFET), Radiation Monitor RadMon) [84,85,86,87] are able to provide, with the aid of simulations, the most accurate radiation maps of CERN's machines and online monitoring at specific locations. This valuable information, and the one derived from qualification tests, allow assessing equipment lifetime, implementing mitigation measures and

minimize radiation to electronics related failures as well as Injectors/LHC downtime. With respect to the current monitoring situation, the installation of a Distributed Optical Fiber Radiation Sensing (DOFRS) has provided additional and complementary means of monitoring radiation levels. This system presents some unique advantages:

- It is especially well adapted for the monitoring of large facilities such as CERN's machine (from tens of meters to several hundreds of meters);
- It can perform distributed radiation dose measurements with a spatial resolution down to one meter;
- It can perform online measurements allowing easy access to data during operation;
- The interrogator unit and all needed electronics are installed in remote/non-hazardous locations;
- The optical fiber cable can be replaced via cable blowing;
- Information of the cumulated radiation dose is stored in the optical fiber itself making it a robust monitoring system;
- Employing different fiber sensors, the system can perform measurements from a few Gy up to kGy.

The goals of this thesis were to continue to investigating new sensors for the DORFS system for application at CERN and to find a way to reset and reuse the dosimeter multiple times without replacing it. To do this we have studied different fibers whose core is doped with P, P-PCe and Al to extend and increase the measurable range of the dose and dose-rate. The possibility of using new and different detectors, HR-OTDR and OFDR, has also been evaluated to obtain a better spatial resolution potentially needed for future installations at CERN.

Summary: In this first chapter, we presented the theoretical background of light transmission in optical fiber. We gave an overview of the characteristic point defects and the corresponding absorption bands for the chemical elements used to dope the studied fibers. After that, we presented the main effects generated by radiation in fibers and their related consequences. Finally, we introduced the potential use of these effects to build a distributed fiber dosimeter and the first installation of such an instrument at CERN, within the DOFRS project.

2 Chapter II - Investigated Samples and Experimental Tools

This chapter consists of three sections. The first one presents the main characteristics of the three OFs which have been at the center of my PhD research work. The chosen OFs have been selected for their high radiation sensitivity, thanks to appropriate doping, and have been evaluated in view of their potential regarding the CERN needs in terms of radiation monitoring in its machine tunnels as well as in facilities. The second section offers an overview of the experimental setups and procedures used for the experiments carried out during this work. The last section describes the irradiation facilities that we used at CERN, in Saint-Etienne.

2.1 Selected radiation-sensitive optical fibers

The main three OFs studied during this thesis are all Single-Mode (SM) optical fibers, they differ by the natures of the dopants incorporated in their silica-based cores: Phosphorus (P), Phosphorus/Cerium (PCe) and Aluminum (Al). All samples have a cladding made of pure silica and have been manufactured by iXblue Photonics [88]. The core dopants increase its Refractive Index (RI) with respect to the one of the cladding, allowing the light guidance through total internal reflection. Each of these elements is known to strongly affect the radiation response of the silica glass in different ways explained by the specific optical properties of their own related point defects. In the same time, all the fibers have different physical properties such as different cut-off wavelengths and then different unimodal regime domains, different radial profiles for the fundamental mode at a given wavelength. In Table 2-1 we summarize the main characteristics of the optical fibers studied in this thesis work.

In Figure 2.1 are reported the Refractive Index Profile (RIP) of the three fibers. The RIP of the three fibers have been measured at iXBlue with IFA-100 Multiwavelength Optical Fiber Analyzer from Interfiber Analysis.

Table 2-1 Characteristics of the studied fibers.

OF		Core	Cladding	Coating	Manufacturer
iXSM-P	SM	~ 6 μm [P] \approx 9 wt. %	125 μm No doping	acrylate	iXblue
iXSM-PCe	SM	~ 6 μm [P] \approx 9.3 wt. % [Ce] \approx 2 wt. %	125 μm No doping	acrylate	iXblue
Al	SM	~ 5.2 μm – 3.3 μm [Al] \approx 4.5 wt. %	125 μm No doping	acrylate	iXblue
P-CERN	SM	~ 6 μm [P] \approx 10 wt. %	125 μm No doping	acrylate	iXblue
PCe-CERN	SM	~ 6 μm	125 μm No doping	acrylate	iXblue

Figure 2.2 illustrates the wavelength dependence of the Confinement Factor (CF) of the light for the three CERN's fibers (P-CERN, PCe-CERN and Al). From these curves, one can easily determine the cut-off wavelength for the three fibers below which the fibers start to be bimodal. In a SM OF and above this cut-off wavelength, only the fundamental one (noted as LP₀₁) is guided along the fiber. If most of the LP₀₁ mode power remains confined in the core, the CF values also confirm that a non-negligible part and evanescent part of the wave is propagating in the fiber cladding. The fraction of light power propagating inside the core is wavelength dependent, increasing at decreasing wavelengths. The spatial distribution of the mode explains that the RIA level will also depend on the nature of the cladding co-dopants even for fiber with identical cores [17,89,90]. For our fiber samples, the dopants are incorporated only in the core whereas the cladding is made of pure silica. Therefore, during the irradiation, the most highly-absorbing point defects responsible for the attenuation will be within the fiber core. This

difference between the radiation responses of the core and cladding materials, coupled with the wavelength dependence of the CF implies that the measured RIA spectra can be distorted and blue-shifted in the SM fiber RIA spectra with respect to the results that would have been obtained for a homogeneous bulk sample.

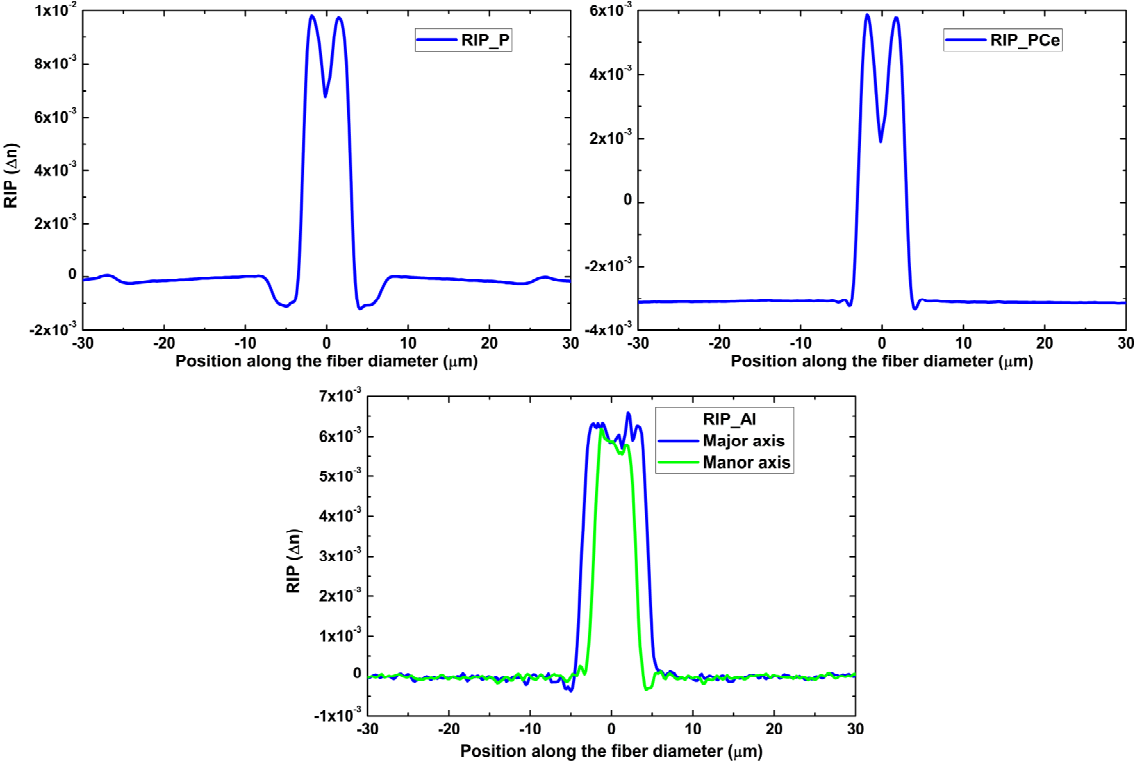


Figure 2.1 RIP of the three SMOFs as a function of position along the fiber diameter (center of the OF at zero), P, PCe and Al-doped OFs, respectively [46].

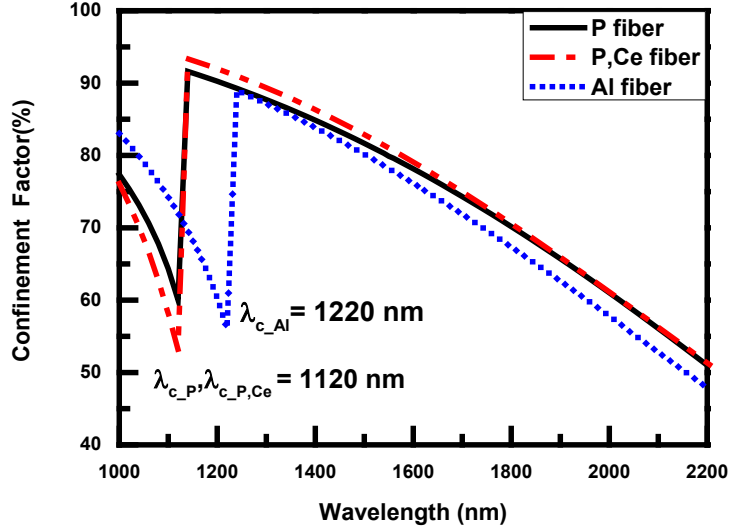


Figure 2.2 Spectral dependence of the confinement factor for P (black line), PCe (red dashed line), and Al-doped SM OF (blue dot line) [46].

We begin by presenting the structure and chemical analysis of the P-CERN doped fiber studied because it is our benchmark, then in the following paragraphs we go on to analyses all the characteristics that a radiation-sensitive fiber must possess in order to be classified as a dosimeter.

In Figure 2.3, we show the radial concentration profiles of P and F measured via Energy Dispersive X-ray (EDX) spectroscopy in the P-doped OF studied. In the inset of the same figure, we show a 2D map of the fiber cross section highlighting the dopant distributions. The P-doping is at the origin of the high radiation sensitivity of this fiber, whereas the F-doping is used to tailor its light guiding properties. The concentration of the residual Cl impurity, resulting from the production process, is of the order of 0.2 wt.% and homogenously distributed in the fiber cross section. The OA of the pristine sample is ~ 2 dB/km at 1550 nm. The refractive index profile of the OF, together with the simulated fundamental mode at 1310 and 1550 nm, have been reported in [46].

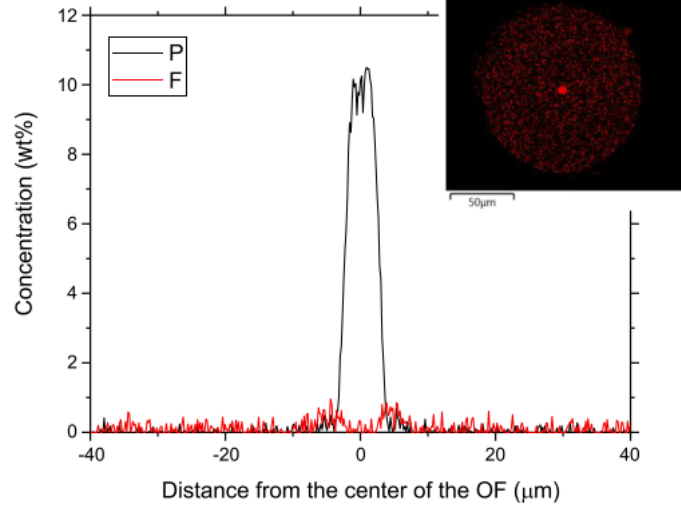


Figure 2.3 EDX measurement of the radial concentration (weight %) of P and F in the investigated OF sample. In the inset, we report a 2-dimensional map of the cross section of the OF with the intensity of the X-ray emission line of P [91].

2.2 Selected instrumentation

When an electromagnetic wave is launched into an optical fiber, part of the propagating light will be scattered by various mechanisms in the form of Rayleigh, Brillouin or Raman scattering processes. Local parameters of the external environment from which the fiber is exposed such as temperature, deformation, vibration, protons, neutrons and ionizing radiation affect its structural or optical properties. It means that the scattered signal in the fiber will be modulated by these physical parameters, and by measuring its changes, one can realize fiber sensors. If the input light injected in the OF is a pulsed signal with a pulse width τ , then the location of the modulated signal along the OF can be measured by the time delay of the speed of light c , the location accuracy is called spatial resolution:

$$\Delta z = \frac{\tau c}{2n_{eff}}$$

Where n_{eff} is the effective refractive index of the fiber. The factor 2 is related to twice the fiber length that the injected light must do to return to the starting point, i.e. the sensor that detects

the scattered light from point z . The pulse width τ defines the spatial resolution of the Rayleigh scattering based optical time domain reflectometer (OTDR).

Distributed sensor can also be realized in the frequency domain, so called optical frequency domain reflectometer (OFDR) based on Rayleigh scattering [92,93] or exploiting the Raman scattering and more specifically the power ratio of Stokes and anti-Stokes signals [94]. Rayleigh-based OFDR uses a tunable laser to scan a frequency range of ΔF and through Fourier transformation produces a spatial resolution of:

$$\Delta z = \frac{c}{2n_{eff}\Delta F}$$

By increasing the frequency scanning range, the spatial resolution can be reduced to a millimeter length or less. The sensing length is limited by the coherence length of the laser source and the state of polarization change along the fiber, which is tens of meters. Early development of OFDR was focused on locating high attenuation points [13] as this technique offers high spatial resolution (*on the order of 1 mm*). The sensing length is limited by the coherence length of the tunable laser (<100 m) [17].

2.2.1 Optical Time Domain Reflectometer (OTDR), HR-OTDR

An OTDR is an OF tester for the characterization of fiber and optical networks. It detects, locates and measures events at any location along the fiber link. The instrument then generates geographic information regarding localized loss and refractive events, providing a real time information about the fiber's main characteristics and performances.

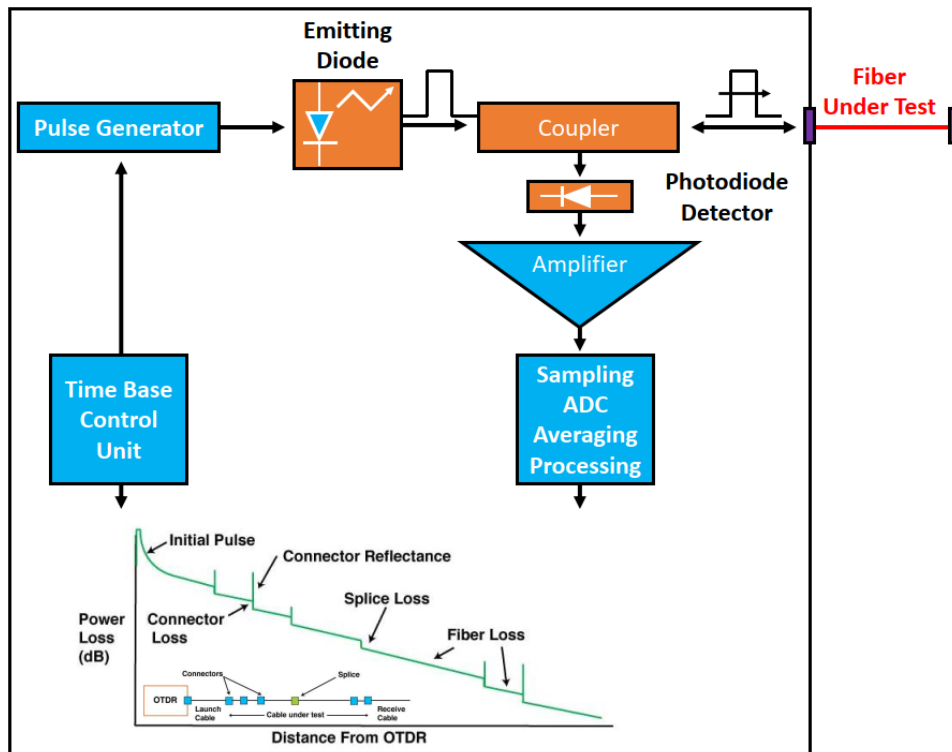


Figure 2.4 Block diagram representation of OTDR system.

An OTDR injects a short and high-peak power optical pulse into the fiber under test and measure the backscattered Rayleigh power as a function of time [95,96]. Knowing the group velocity of the pulse, the time scale can be converted into fiber length scale. The spatial information can therefore be obtained from the pulse round-trip time between the fiber input and a given position along the fiber. Due to the fiber intrinsic attenuation, the power associated to the launched pulses is gradually attenuated as the backscattered power. While light propagates into the OF, optical pulses encounter Fresnel reflections and Rayleigh scattering locations resulting in a fraction of the signal travelling back in the opposite direction which is linearly proportional to the optical power pulse at that location. One of the main advantages of the OTDR technique is that it only requires the access to one single end of the fiber.

Light energy is injected into the fiber by means of a laser diode and a pulse generator that produces a train of short optical pulses. A coupler fed to the photodiode separates the returning

light energy from the injected signal. The optical signal is converted to an electric signal, amplified, sampled and displayed. A representation of block diagram of an OTDR is reported in Figure 2.4. The lower part of the figure reports an example of the OTDR trace showing a vertical scale of attenuation in decibel (dB) and a horizontal scale of distance in kilometers (km) or meters (m). Numerous acquisition points are plotted, representing the backscatter signature of the fiber under test. There are three key parameters to assess one OTDR performances: its sensing distance that depends on the optical budget of the instrument and then on the optical fiber attenuation, its allowed discrimination between close events and its spatial resolution.

Its *dynamic range* is defined as the difference between the extrapolated point of the backscatter trace at the near end of the fiber and the upper level of the noise level at (or after) the fiber end. It is one of the most important characteristics as it determines the maximum length that can be probed. The higher the dynamic range, the higher the signal to noise ratio (SNR), and the better the trace and event detection. In fact, one of the most important factors affecting the SNR is the noise of the optical receiver. Shorter pulses imply higher spatial resolutions but carry less energy and require a broader receiver bandwidth which introduces additional noise and decreases the dynamic range.

The *dead zone* is the distance where the OTDR cannot accurately detect or locate any event or artifact along the fiber link. It is related to the recovery time of the photodiode from its saturated condition after a strong reflection. The length of fiber that is not fully characterized during this period is the dead zone. The last key parameters are *resolution* and *accuracy*. We can distinguish four types of *resolution*: Display Resolution, Loss Resolution, Sampling Resolution and Distance Resolution. The *accuracy* of a measurement refers to its capacity to be compared with a reference value. For a more complete description see [2].

In conclusion, it is very challenging to perform long distance measurements which require a high dynamic range with short testing pulses which would offer a high spatial resolution. To

reduce the detrimental impact of noise, a "signal averaging" method [95] is often used. In such cases, the measurements are repeated N times and then averaged. If the system is dominated by noise with mean value equal to zero, the noise is automatically reduced by a factor equal to \sqrt{N} implying that the electrical SNR of the measurements will also be enhanced by a factor \sqrt{N} . Of course, this implies an increment in the measurement time by a factor N [96].

OTDRs measure the optical losses at the wavelengths of their lasers. The main wavelengths for OTDR, as the ones used for the first installation in the PSB at CERN, are 850 and 1300 nm for multimode fiber (although from an operational standpoint, measurements have only been made at 850 nm) and 1310, 1550, and 1625 nm for single-mode fiber (also in this case the wavelength used from the operational point of view is 1550 nm). For the purposes of this thesis, having studied only single-mode OFs, we exclusively used single-mode OTDRs. In particular we have focused on the wavelength of 1550 nm as the P1 band has its optical absorption peak right there.

2.2.2 Optical Frequency Domain Reflectometers (OFDR)

OFDR is based on the frequency modulated continuous wave technology and involves Fourier transform of interference fringes from the fiber under test and from a reference arm. Also, since the spatial distribution of the reflection pattern contains both amplitude and phase information for every measurement, any change applied to the fiber (such as temperature, strain, humidity, radiation, refractive index...) can be measured by comparison with a reference trace [13]. OFDR methods fall into two main categories: incoherent OFDR (I-OFDR) and coherent OFDR (C-OFDR) [97]. For our experiments we had a C-OFDR at our disposal and so we will make a concise presentation of this OFDR category. Its operation principle is schematically reported in Figure 2.5.

Light from a tunable laser source is split and sent through measurement and static reference arms of an interferometer and recombined at an optical detector. Interference fringes are

generated as the laser frequency is tuned. Those fringes are detected and related to the optical amplitude and phase response of the system, or FUT. The interference fringes, occurring in the spectral domain of the FUT data can be processed using the Fourier transform into the time domain. In this domain, a map of the backscattered signals as a function of length internal to the FUT can be constructed. Hence, OFDR can be used for both spectral and time domain reflectometry. OFDR offers an alternative solution for a highly-spatially resolved measurement system exploiting the frequency response of the sensing fiber and converting it into the time/spatial domain response by Fourier transform to reconstruct the scattering pattern.

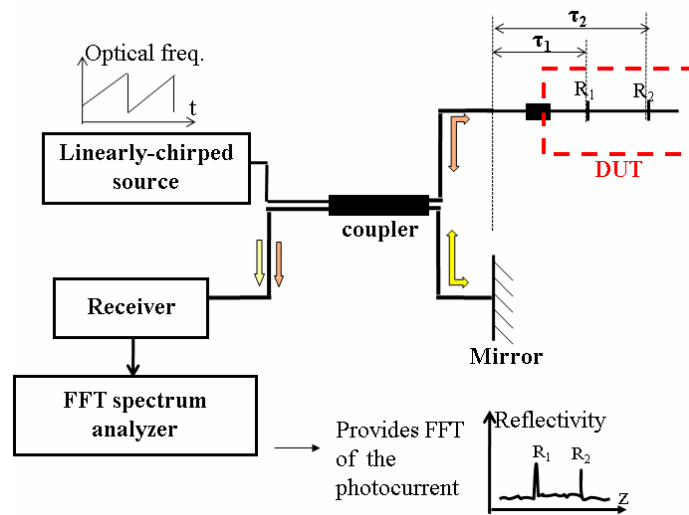


Figure 2.5 Schematic representation of how a C-OFDR works [97].

C-OFDR has got some advantages inherent to the coherent detection scheme. First of all, the measured photocurrent is not proportional to the reflected optical power but to its square root, which permits the system to measure signals with large amplitude differences. Secondly, the receiver bandwidth (RF frequencies) is lower compared to the OTDR techniques reducing the noise level and increasing the dynamic range (around 10 dB). Moreover, C-OFDR systems have got the ability to measure active devices (e.g. optical amplifiers) without saturation since only low power CW signals are used. Finally, no dead zone is observed in C-OFDR since the receiver does not saturate as in pulsed OTDR methods. However, C-OFDR has a problem in dealing

with long measurement distances as the measurement distance is limited by the coherence length of the tunable source [97]. For our radiation tests, we used an OBR 4600 by LUNA with the following characteristics:

- 10 micron spatial resolution with zero dead zone
- Sensing length up to 2 km
- could probe both single-mode and multi-mode fibers using the same instrument (but we used the OFDR only with SM OFs)
- Track change in the state-of-polarization as light propagates an optical network

2.3 Irradiation facilities

We now present the different facilities where the irradiation tests and the experiments have been carried out during this PhD work.

2.3.1 ^{60}Co facility at CERN

The ^{60}Co γ -ray irradiation facility at CERN is schematically represented in Figure 2.6. This facility allows performing gamma-ray irradiations up to 14 mGy/s dose rate at room temperature. The dose rate can be adjusted by moving away the sample from the source up to 4 m. The uncertainty on the dose rate is 5% at 2σ . In our γ -rays irradiation tests, fiber samples have lengths varying between 10 and 15 m and the fiber was coiled up in spools of 7 cm diameter ensuring the homogeneity of the dose deposition in the sample.

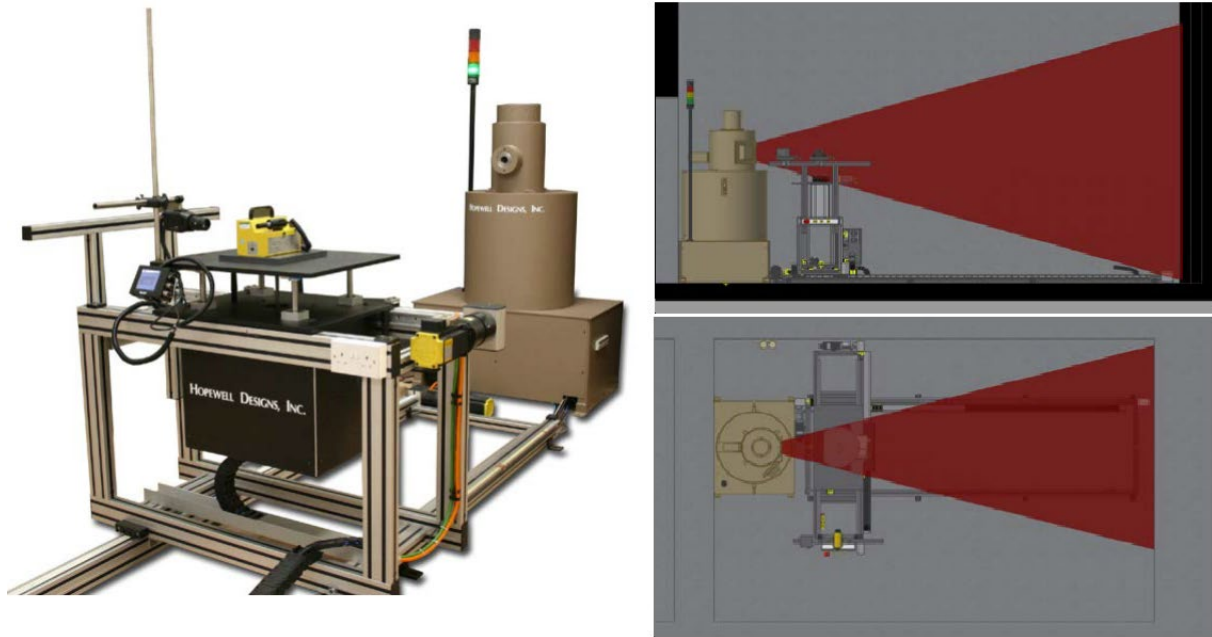


Figure 2.6 Picture of the protective box containing the source and movable table of ^{60}Co in the facility at CERN (left side). Side and top view of the irradiation chamber (right side).

2.3.2 CHARM facility at CERN

CHARM (CERN High energy AccelERator Mixed field facility) has been built at CERN in the Proton Synchrotron (PS) east area. The facility is illustrated in Figure 2.7. The facility scope is to assess radiation effects on electronics not only at component level but also at system level within particle accelerator representative environments. Its available radiation fields are also characteristics for ground and atmospheric environments (neutron energy spectra) as well as for space environments (representative for the inner proton radiation belt). The size of the available test area is such that large objects can also be irradiated. A 24 GeV/c proton beam extracted from the PS is focused on a cylindrical aluminum or copper target generating a mixed radiation field composed of protons, neutrons, pions, photons, muons and other particles. This unique facility [98], provides a variety of particle energy spectra which can be representative of several radiation environments and allowing large acceleration factors up to around 10^9 . It can be used to test electronics, optics and photonics equipments to be installed within particle

accelerators, and also to test devices and systems to be used for space, atmospheric and ground level applications. The choice of the target among two massive ones made of aluminum or copper and one with reduced effective density, allows to modulate the intensity of the radiation field with adjustments in the intensity over an order of magnitude.

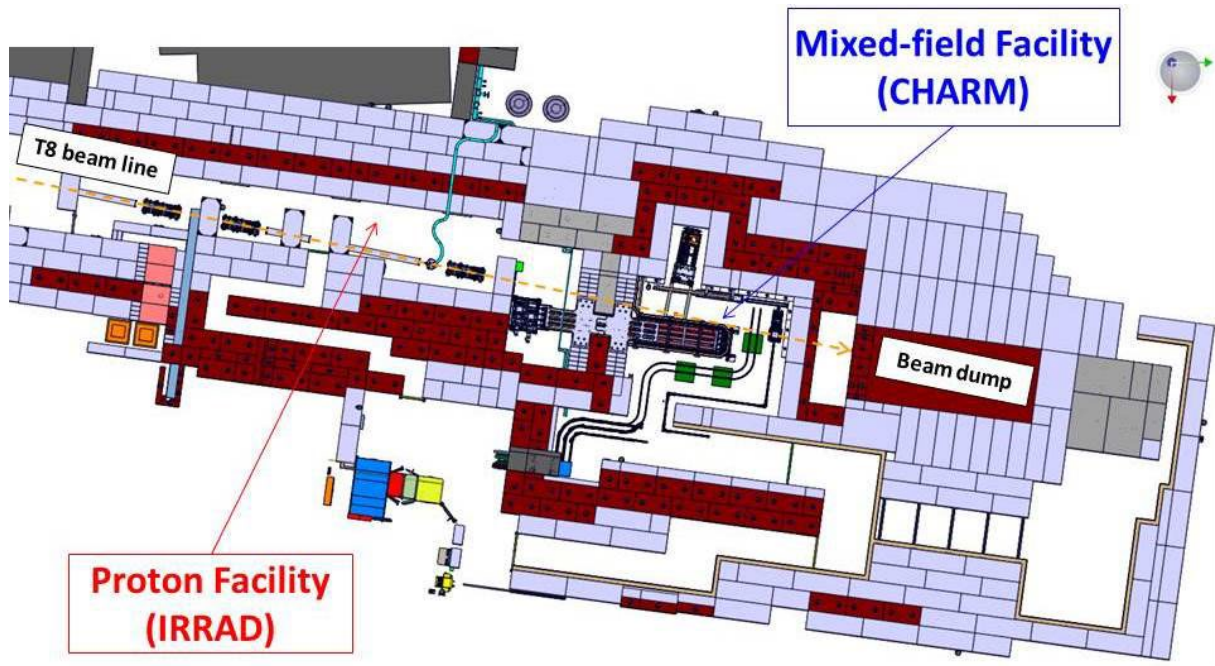


Figure 2.7 Proton Synchrotron east area at CERN with CHARM facility on the right side.

An additional way of completely changing the radiation field is provided by four mobile shielding plates of 40 cm of width each, two made of concrete and two made of iron, which can be placed between the target and a set of predefined test positions where the components under test will be placed. The desired shielding and target configurations can be remotely controlled according to the needs in terms of particle spectra and intensity. Figure 2.8 represents the irradiation chamber of CHARM facility. The numbered squares represent the different positions where it is possible to install the equipment to be tested.

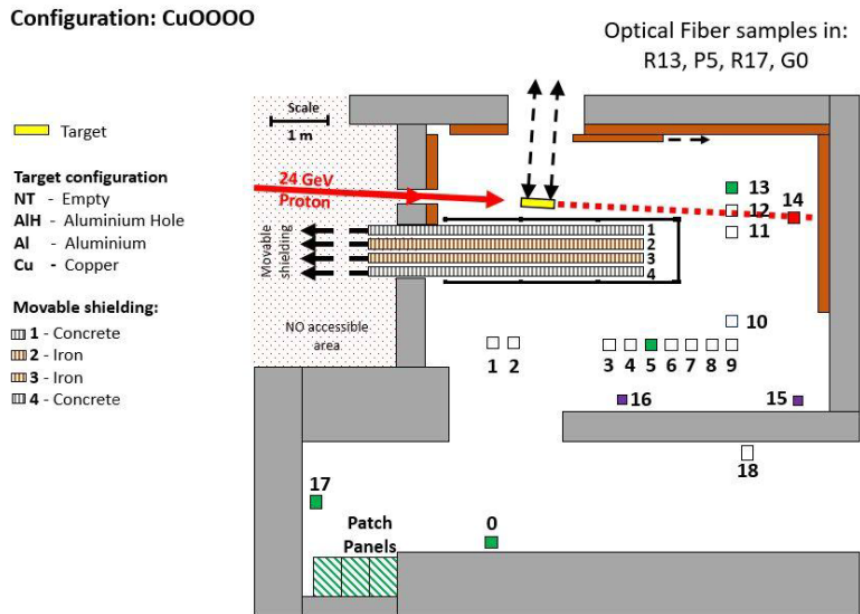


Figure 2.8 Schematic layout of the CHARM facility at CERN [99].

Near the target there is a table, not shown in Figure 2.8, where it is possible to place some samples to be tested. This position is associated with a significant gradient of field and consequently larger uncertainty on the dose. An error of the dose about $\pm 25\%$ can be associated to measurements done in CHARM.

2.3.3 MOPERIX machine in Saint-Etienne

Most of the RIA experiments were performed by irradiating the fiber samples with the X-ray MOPERIX machine (Figure 2.9a) of the Laboratoire Hubert Curien (St Etienne, France). The X-ray tube, which is equipped with a tungsten target, was operated at 100 kV to generate photons of ~ 40 keV average energy (see Figure 2.9b). The dose-rate can be varied either by changing the sample/tube distance or by varying the beam current. For X-ray irradiation, samples have been prepared in single-layer coils to avoid any shielding issue during irradiation. The temperature of irradiation can be controlled using a thermal plate allowing varying the temperature in the 20°C to 300°C range.

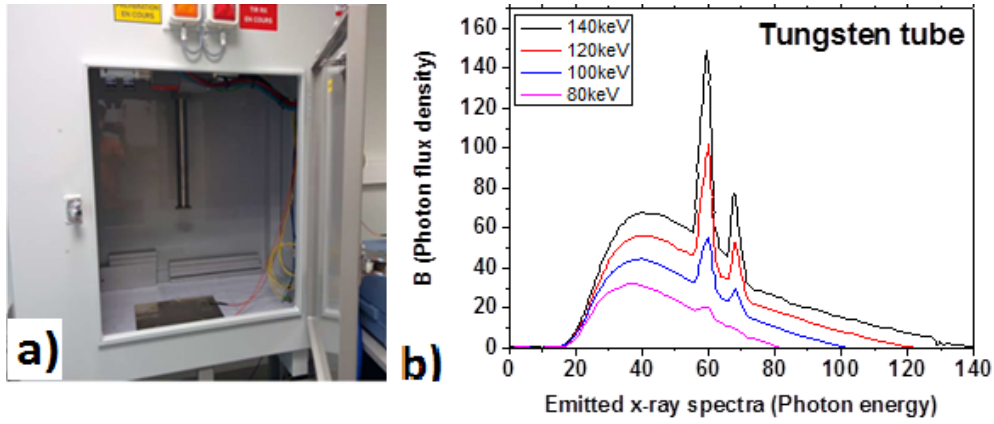


Figure 2.9 Illustration of the MOPERIX facility b) Typical X-ray beam spectra for a tungsten target operated at different voltages from 80 to 140 kV (adapted from [100]).

According with the mass attenuation coefficients of Si and O reported by the NIST [101], in silica the primary X-ray beam is reduced by a factor $1/e$ after about 0.18 and 2.7 cm at energy of 20 and 100 keV, respectively. Within 125 μm the attenuation at these energies is of 7% and 0.5 %. The dose rates or the doses in silica were evaluated according to the following procedure. The dose rate values measured by a N23344 soft X-ray chamber were converted in values in water using the calibration factors in the range 0.02-0.1 MeV, which is the energy range of the X-ray beam of the tungsten target. Then, by using the NIST [101] data for the mass energy absorption coefficients (μ_{en}/ρ) of Si, O and H, those of the silica and water were evaluated. Finally, the doses or the dose rates in silica were obtained using the following equation:

$$\text{Dose}_{\text{silica}} = \frac{\int_{0.02\text{MeV}}^{0.1\text{MeV}} E \cdot N(E) \cdot \left(\frac{\mu_{\text{en}}}{\rho}\right)_{\text{silica}}}{\int_{0.02\text{MeV}}^{0.1\text{MeV}} E \cdot N(E) \cdot \left(\frac{\mu_{\text{en}}}{\rho}\right)_{\text{water}}} \cdot \text{Dose}_{\text{detector-calibrated}}$$

where E_{ph} is the energy of the photon, $N(E)$ is the number of photons at energy E , (μ_{en}/ρ) are the mass energy absorption coefficients of silica and water and D_{calib} is the calibrated value obtained by the chamber.

2.3.4 TRIUMF facilities (Vancouver, Canada)

Some of the experiments were conducted at the TRIUMF Neutron Facility (TNF) and Proton Irradiation Facility (PIF)

The Proton Irradiation Facility (PIF) [102] is mainly devoted to single-event effect (SEE) studies and characterization of electronic components and detectors for space. PIF makes use of two different beamlines at TRIUMF. Beamline BL2C is devoted to lower energies, from 5 MeV up to 120 MeV while the BL1B beam line is devoted to higher energies, from 120 MeV up to 500 MeV. For the results presented in this study, a proton energy of 480 MeV was used from the high-intensity beam line BL1A [103]. It allows comparing the calibration coefficient of the P-doped SMF fiber observed under proton exposure to the results obtained at CERN under γ -rays.

After traversing several experiments, the protons of 100 to 150 μ A current and 400 to 450 MeV residual energy are stopped in a beam dump on an aluminum plate absorber surrounded by a water moderator [104]. Neutrons are produced from spallation reactions and are subsequently channelled through the shielding surrounding the TNF, illustrated in Figure 2.10.

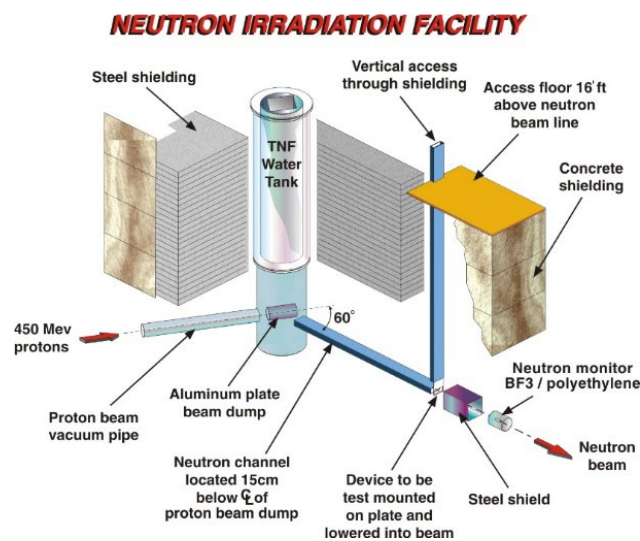


Figure 2.10 Schematic representation of TRIUMF Neutron Irradiation Facility in Canada [105].

The resulting neutron spectrum, simulated with FLUKA, is illustrated in Figure 2.11 and compared to the JEDEC standard JESD89A of terrestrial cosmic rays which induces soft errors in semiconductor devices [106]. This comparison shows that the TNF facility is well adapted for the accelerated testing of the vulnerability of technologies to these radiation constraints, offering a flux approximately 10^9 higher than the reference spectrum observed under standard conditions in New York City, USA. The P-doped SMF has been tested to neutron exposure at the TNF are mounted on an aluminum plate and lowered about 5 m into the neutron beam through a cable system in a vertical access channel. Once the fiber was in place, a counter records the neutron exposure in a neutron detector at beam level. The P-doped SMF was exposed in June 2019 at room temperature to an integrated neutron flux of $\sim 3.35 \times 10^6$ n [10 MeV – 400 MeV] $\text{cm}^{-2} \text{s}^{-1}$ for approximately 59 h to reach a total fluence of $\sim 7.1 \times 10^{11}$ n cm^{-2} . The FLUKA simulations of the TNF neutron spectrum (Figure 2.11) were exploited in order to calculate the equivalent dose and dose rate in Gy(SiO_2) and Gy/s associated with these test conditions. From these calculations, which consider neutrons within an energy spectrum from 0.1 to 400 MeV, a relationship is obtained between the neutron fluence and the equivalent dose in Gy(SiO_2). The neutron run was associated with an equivalent dose rate of ~ 0.91 Gy/h up to a total dose of ~ 53.8 Gy. The irradiation temperature remained between 20 °C and 30 °C. The obtained neutron calibration coefficient is then compared to X-ray experiments done with MOPERIX at UJM.

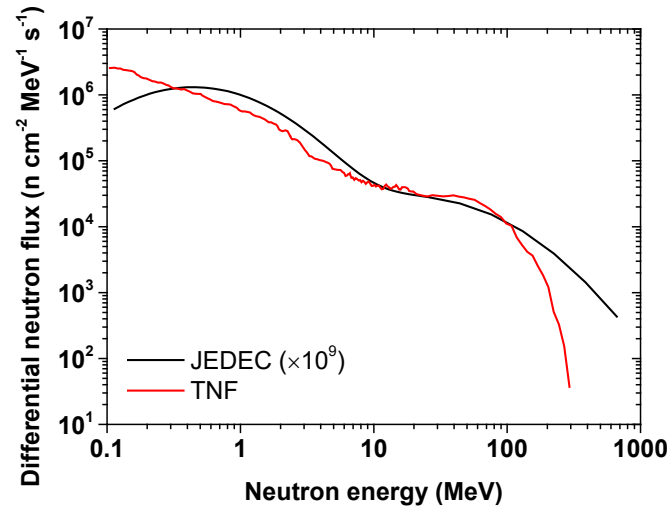


Figure 2.11 Simulated neutron spectrum of the TRIUMF TNF facility compared to the JEDEC atmospheric neutron reference spectrum. Accelerated tests are possible at a flux approximately 10^9 times higher than on the Earth's ground.

2.4 Experimental setups

2.4.1 RIA, RIA/T, T (recovery)

The online Radiation Induced Attenuation (RIA) technique consists in evaluating the losses of transmitted light in an OF during the irradiation [7,32]. In this experiment an OF is connected to a light source and a spectrometer and, at the same time, a part of the OF is irradiated. The time evolution of the induced losses is determined relatively to the initial transmitted spectrum with a time resolution not higher than 1 second. Very often, in order to ensure the same irradiation conditions, two or more fibers are tested at the same time. The experimental setup, (reported in Figure 2.12) consists of an UV-VIS-NIR light source (Deuterium-Halogen DH-2000 light source by Ocean Optics) and a NIR spectrometer (NIRQUEST by Ocean Optics). The sample is coiled “spiral shape” without overlapping it and is positioned inside the irradiator. In some experiments, the sample was spliced to a radiation resistant fiber to be connected to the source and to the spectrometer, located in the instrumentation zone. In turn the spectrometer is connected to a computer that allowing to acquire the spectra before, during and after the end of

the irradiation. The spectral resolution of the used spectrometer is 5 nm, and the spectral range is 900-2200 nm approximately.

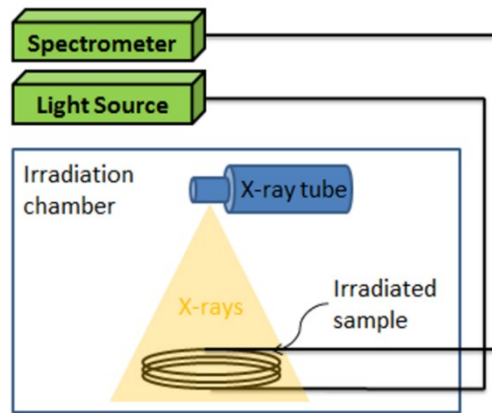


Figure 2.12 Schematics representation of setup employed for the online RIA measurements.

To carry out the irradiation at different temperatures we mounted our sample on a heating metallic plate installed at the bottom of the irradiation machine. The temperature was continuously monitored with two thermocouples and its evolution recorded through a Thermocouple Data Logger by Pico Technology. During the experiments, the temperature always remained within 0.5 °C from the targeted one.

For the recovery experiments as a function of the temperature, we stopped the irradiation and, keeping the temperature of the heating metal unchanged, we continuously acquire the data.

2.4.2 Cut-back

The cut-back technique consists in measuring the optical absorption (OA) of an OF by comparing the difference of light intensities along two different lengths of the same fiber sample. In practice, the technique consists of measuring the attenuation of transmitted light using two different lengths of the fiber and then applying Lambert-Beer's Law:

$$\alpha = \frac{10}{L_1 - L_2} \log \left(\frac{I_{L_1}(\lambda)}{I_{L_2}(\lambda)} \right)$$

where $L_1 > L_2$; we injected the light in the irradiated sample by a source and then we measured the transmitted light with a spectrometer. After that, we removed part of the sample and performed the measurement again. To avoid touching the instrument connectors and thus altering the measurement, we used a few meters of pristine fiber as launch cables and spliced our sample in between. To be sure that the quality of the welds did not compromise the experiment, we applied the following protocol:

- We spliced the sample between the launch fiber pigtails and we made the measure;
- We broke one of the two splices and redid it, and repeated the measurement (repeatability test).
- After that we always broke the same splice, removed a piece of sample, and repeat again the measure;
- Finally, we broke again the same splice and redo it, and repeated the measurement (repeatability test).

For each pass we always worked with one splice, keeping the second one unchanged, and noted the pieces of fiber that were removed for each new splice. For each measurement taken, a measurement was recorded without the source (shuttered for a short time), to monitor the variation of spectrometer noise during the experiment. The stability of the source was also verified before starting the measurement campaign. The method was applied for the characterization of irradiated OFs as well as the pristine ones. The difference between the post-irradiation absorption spectrum and the pre-irradiation one gives the post-mortem radiation induced attenuation spectrum. It is worth to mention that, depending on the tested OF and the irradiation conditions, the OA before the irradiation is negligible compared to the one after the irradiation, therefore the latter one coincides with the post-mortem radiation induced attenuation (RIA).

2.4.3 Photobleaching

The experimental setup used for photobleaching (PB) tests and developed in the framework of this PhD thesis is illustrated in Figure 2.13. This setup will be exploited in Chapter 5.3 to demonstrate that it is possible to regenerate the P-doped fiber-based dosimeter before its reuse under irradiation.

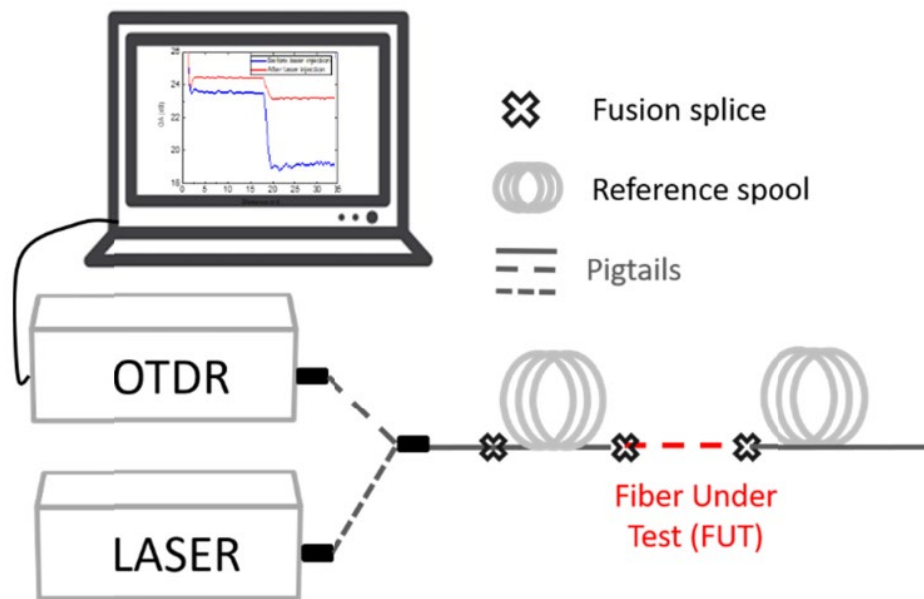


Figure 2.13 Experimental setup for the Photobleaching tests.

The irradiated fiber under test (FUT) is spliced at both ends to two OF coils of the same fiber not irradiated. These coils serve for reference analysis. As with the investigated radiation sensitive fibers, the RIA levels at 1550 nm can be of several dB per meter (*for example 4.2 dB/m for a P-doped fiber irradiated at 1170Gy*) it is necessary to use short fiber length to respect the optical budget of the OTDR probe instrument (12 dB). The selected T-BERD/6000A OTDR from VIAVI Solutions [107] has a spatial resolution of ~ 1 m. To overcome these issues, the one-meter sample under test is located between two 15 m long spools of not-irradiated fibers. This allows a fine monitoring of the PB efficiency evolution during the laser light injection,

even when working near the OTDR's dead zone. During the PB experiments, the fusion splices are never touched and light coupling conditions are strictly preserved during the entire procedure. OTDR traces are recorded before and after the PB step (*which could typically last one hour*) thanks to an FC/APC connector that allows to connect, one at a time, the instruments to the FUT. To induce the PB we used a few SM (or Multimode (MM)) Fiber-Pigtailed Lasers' from THORLABS [108] emitting at different wavelengths, as well as a cw Argon-ion laser line at 514 nm.

Figure 2.14 gives an example of the OTDR traces acquired before and after the 1, 2 and 3-hour laser light injections into an irradiated sample (1170 Gy) of the P-doped SMF. In this figure the two reference spools used to evaluate the RIA losses are highlighted. The initial RIA losses generated by the irradiation (measured by cut-back) and the intrinsic splices losses are also highlighted. The step in the middle of the traces, in between the two almost horizontal sections (reference spools), is due to the absorption of the irradiated samples and the losses at the two splice points. It is possible to quantify such effect by simply taking the difference of the two traces, since the two splices were not modified. Knowing the RIA values at 1550 nm before the PB, we can estimate the RIA recovery level over the 1 m long sample. From Figure 2.14, the reduction of the jump amplitude due to the PB effect is accompanied by an improved signal-to-noise ratio in the last part of the OTDR trace.

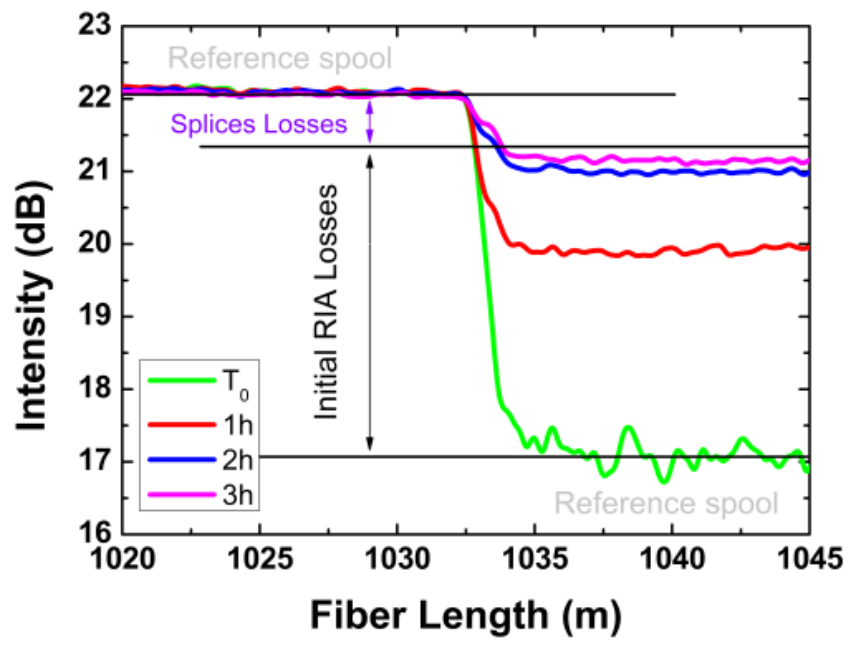


Figure 2.14 OTDR traces (at 1550 nm) of the P-doped sample irradiated up to 1170 Gy and bleached with 514 nm Argon-ion laser line (430 mW) at different times.

2.4.4 H₂-Loading

We carried out the H₂ treatments by placing the fiber samples under test in a PARR 4651 reactor, see Figure 2.15, and filling it up with 150 bars of H₂, at room temperature. It is worth to highlight that the bleaching test with H₂ loading was performed on slightly different fiber samples (canonical samples from UJM), precursor of the ones on which this PhD thesis focuses on and developed by iXblue for CERN needs. However, they have very similar chemical properties and performances, they will be named iXSM-P and iXSM-PCe in this manuscript and their characteristics are reported in Table 2-1. The fiber acrylate polymer coating gives no problems for the hydrogen diffusion that takes place transversally along the fiber cross section. Special custom-made connectors allowed the extremities of the OF to be externally accessible during the treatment. It was then possible to monitor *in situ* the evolution of the sample optical attenuation with the same technique explained for the RIA measurements (paragraph 2.4.1). Based on preliminary investigation [109], the duration of the H₂ loading was set to the

minimum necessary to permeate the OF cross section (no saturation was reached) and recover all the radiation-induced losses. Before the second irradiation, the H₂-recovered sample was left for 25 days at room temperature in air atmosphere to let the excess interstitial H₂ out-diffuses.

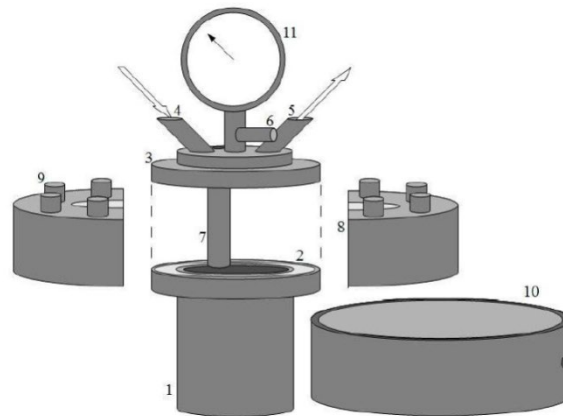


Figure 2.15 Schematic representation of the PARR reactor employed for the H₂ loading treatments. 1 is the vessel, 2 is a gasket, 3 is the cover of the vessel, 4 and 5 are the input and output valves for the gases, 6 is a pressure transducer, 7 is the well in which a thermocouple is placed, 8 and 9 are two steel half-rings for closing, 10 is a safety steel ring, 11 is a analogical pressure gauge. Adapted from [40].

Summary: In this short chapter we have presented the fibers studied, the instrumentation and techniques used to conduct our experiments, and the facilities in which they were conducted. After summarizing the main characteristics of the fiber samples studied in this PhD thesis, the two main tools used to conduct many of our experiments, OTDR and OFDR, and their principle of operation were presented. We gave a description of the structures used to obtain our results and the techniques used and developed during this work. In particular we have presented the protocol adopted to measure the effect of photo-bleaching on irradiated fibers and the experimental setup adopted to perform the experiments.

3 Chapter III - Investigation of the Fiber Dosimetry Properties

This chapter presents the results of our study carried out to qualify the dosimetry properties of the three selected single-mode OFs. Particularly we present an exhaustive study of the P-doped OF, as this OF was already selected for the implementation of fiber-based dosimetry at CERN facilities and is used for reference and comparison. We also characterize and analyze the dosimetry performances of the PCe and Al-doped SMOFs, two other classes of promising radiation sensitive fibers. Before to present the experimental results, we briefly review the needed characteristics that a radiation-sensitive fiber should possess in order to build a fiber-based dosimeter.

3.1 Definition of the dosimetry properties

A fiber-based dosimeter is a photonic system exploiting the radiation response of the optical waveguide. Radiation modifies some of the characteristics of the optical signal. Today, the RIA and RIE in optical fibers are mostly exploited to design radiation detectors, beam instrumentation or dosimeters. In this work, we measured the infrared RIA to monitor the total ionizing dose. That means that we build an intrinsic sensor as the optical fiber serves as the sensitive element. Then, the solution discussed in this PhD thesis differs from the extrinsic sensor technologies where a sensitive probe (crystal, ...) is connected to an optical fiber that solely serves to transport the optical signal from the probe material to the detector.

A very significant feature of an optical fiber dosimeter is that the dose monitoring is obtained by considering optical signals rather than electrical signals such as e.g. in the case of Floating-Gate or RADFET technologies. Consequently, fiber-based dosimeters are immune to quasi all electromagnetic perturbations that could alter the alternative microelectronic-based dosimeters.

In addition to the development of radiation resistant fibers, the advancement of OF sensing technology has introduced a number of alternatives to conventional dosimetry techniques. The optimal length of the sensing fibers used depends on the desired sensitivity and the interrogating wavelength of the system. Most OF sensors show increased sensitivity as the fiber length increases, allowing for lower doses to be measured [110]. However, the intrinsic (before irradiation) optical attenuation must be considered when choosing long lengths of fibers. This optical attenuation generally increases as the wavelength decreases, from the near-IR region and therefore the selected wavelength is often specific for optimum measurement. Thus, attenuation can restrict the sensing length of distributed dosimetry systems.

3.2 Dosimetry properties of the optical fibers

In this section, we present the results of several irradiation tests we carried out. In order to qualify and calibrate the investigated OF for dosimetry, it was necessary to explore different aspects of the fiber radiation response:

- Assessing the **RIA dependence on the dose**; ideally this dependence should be linear to simplify the calibration procedure.
- Verifying the **absence of dose rate dependence**; this is a crucial aspect as we have to ensure that the measured RIA can only correspond to one dose.
- Verifying the **absence of spontaneous recovery** processes after irradiation (in the temperature range of interest); this is not a mandatory characteristic except for the case where post-mortem dosimetry measurement is performed.
- Studying the **RIA dependence for successive irradiation** to highlight potential dependence on the irradiation history; it should be checked that the response of the fiber depends not too much on its profile of use.

- Verifying the **absence of any photo-bleaching effect** induced by the injected probing light; this is mandatory to have the best performances during the whole lifetime of the dosimeter.
- Verifying the **absence of dependence of the irradiation temperature** (within the temperature range of interest). As for the dose rate, this is a crucial property to verify.

In the following paragraphs we will investigate all these properties for each of the three different fiber types considered.

3.2.1 Dose dependence

Some of the results on the P-doped optical fibers have been obtained and published by Diego Di Francesca (prime investigator) in [91]: D. Di Francesca, et al. “*Qualification and Calibration of Single-Mode Phosphosilicate Optical Fiber for Dosimetry at CERN*”, J. Lightw. Technol., 37(18) 4643–4649, 2019, doi: 10.1109/JLT.2019.2915510. **(ANNEX 1)**

Numerous tests have been performed under X-rays and γ -rays to characterize the evolution of the RIA in the three fibers as a function of the deposited dose. In the case of the P-doped fiber, a fine characterization was mandatory as this RIA dose dependence serves as the calibration curve for the dosimeter and then directly defines the sensor performances. ^{60}Co γ -ray irradiation tests were then carried out at CERN to verify the radiation sensitivity and dose-rate dependence of the P-doped OF at room temperature. Figure 3.1 illustrates the dose dependence of the RIA measured at 1550 nm at five different dose rates ranging from 0.048 mGy/s to 5.76 mGy/s. The five RIA measurements at the different dose rates were carried out in parallel by placing the OF samples at different distances from the radiation source. In all cases we assured a good field homogeneity across the sample spool. An optical switch was used to probe each sample serially at regular time intervals (~ 1 minute). For less than 500 Gy, the RIA increases linearly with the dose (with less than 5% error). In this range, the radiation sensitivity at 1550 nm is about $4 \text{ dB}\cdot\text{km}^{-1}\cdot\text{Gy}^{-1}(\text{SiO}_2)$ with a 10% uncertainty due to the accuracy of the dose rate

measurement. We could not highlight any dose rate dependence within the investigated range and experimental accuracy.

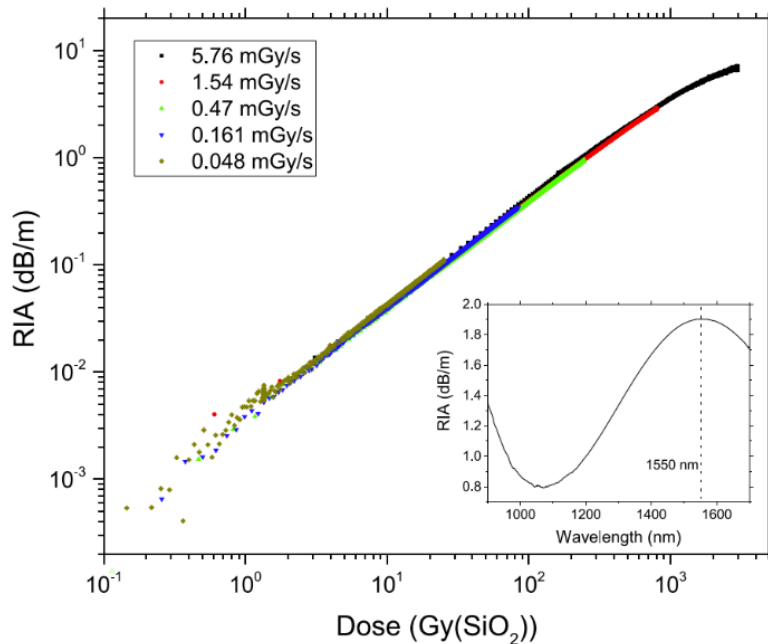


Figure 3.1 RIA as a function of the dose at 1550 nm for the P-doped OF at five different dose rates [91].

3.2.2 Dose rate dependence

We carried out X-ray irradiation to test the range where our potential dosimeters are independent to the dose rate. The tests have been performed in Saint-Etienne with the MOPERIX machine. The X-ray tube, which is equipped with a tungsten target, was operating at 100 kV to generate photons of ~ 40 keV average energy. Therefore, we performed the experiments with our three fibers, varying only the dose rate and leaving all the other experimental parameters unchanged (dose, temperature, time). All experiments were here performed at room temperature.

To find the desired dose rate value, we change the current of the irradiator and the distance between the sample and the X-ray tube. Once the desired dose rate was found, the samples were irradiated consecutively without changing the set-up, when possible. The dose rate range

selected to carried out the experiments were: 0.05, 0.7 and 10.3 Gy(SiO₂)/s; a very large range compared to the one used in experiments conducted at CERN. This allowed us to gain a deeper and broader view of fibre behaviour even at high dose rates. Figure 3.2 reports the result obtained for the P-doped OF. In a) we find the spectra acquired in the near infrared region from 900 nm to 1900 nm and in b) the growth kinetics at 1550 nm.

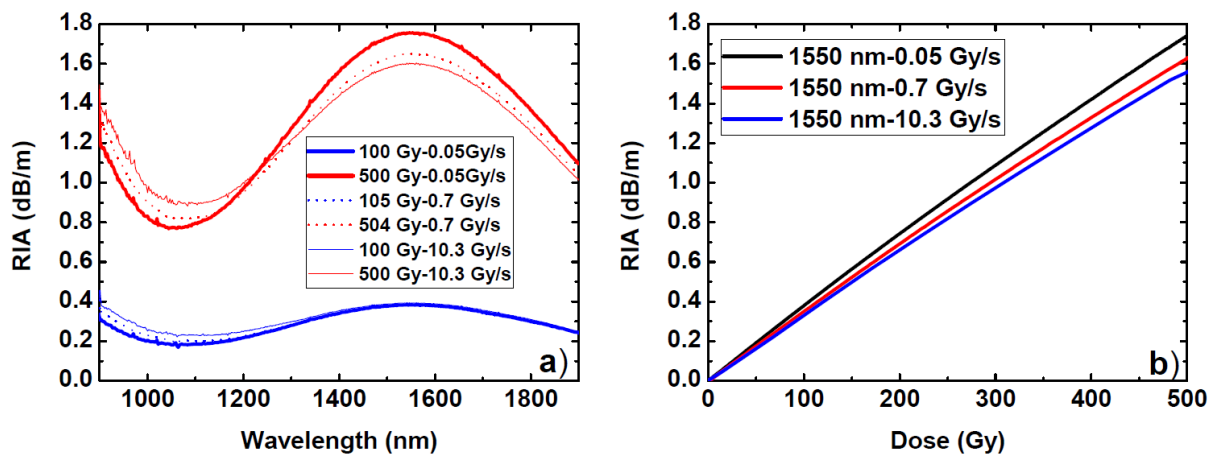


Figure 3.2 RIA spectra of P-doped OF at three different dose-rates at 100 and 500 Gy a); RIA growth kinetics at 1550 nm of P sample irradiated up to 500 Gy at three different dose-rates as a function of the dose b).

Our results show a slight dose rate dependence, RIA is slightly higher at lower dose rate. In the last three decades, several authors described and discerned the difference between “True” dose rate effect and Time dependent effect in microcircuit transistors and bipolar linear circuits. To our knowledge, at the moment, there are very few dedicated studies in the literature on this problem in the field of radiation sensitive optical fibers [42]. However, some articles discuss this effect in more details [42]. To be as clear as possible, we report the definition of True dose rate effect given by R. L. Pease et al.: “A true low dose rate effect means that the degradation at the end of a low dose rate irradiation is greater than the degradation measured after irradiation to the same dose at high dose rate followed by a room temperature anneal for a time at least as long as the irradiation time at low dose rate. A time-dependent effect means

that the degradation at high and low dose rate is essentially the same when measured at the same time from the beginning of irradiation (including anneal time)” [111]. It has been demonstrated that many bipolar linear circuits exhibit a “true” dose rate effect that has become commonly known as enhanced low dose rate sensitivity (ELDRS) [112,113]. ELDRS is characterized by a low dose rate enhancement factor that is the ratio of the parametric degradation at a low dose rate to the degradation at a high dose rate for a fixed dose. This approach to characterizing the dose rate response of bipolar devices and circuits as an enhancement factor versus dose rate was first used by Johnston, et al. [113]. In order to get a clearer idea of the results shown in the Figure 3.2, in Figure 3.3 we retrace the growth kinetics as a function of time during and after the irradiation run. The gray arrows indicate the irradiation end. The first effect clearly observable is the higher RIA value obtained at the lower dose rate, whereas the RIA levels for the other two dose rates under consideration are quite similar. The second important thing to consider is the absence of spontaneous recovery after the end of irradiation that seem independent from the irradiation dose rate. These results support the hypothesis underlying our research that phosphorus-doped fiber is today the best candidate for dosimetry applications.

In Figure 3.4 we report the irradiation results for the PCe-doped OF. The experiments were carried out in the same conditions and with the same set-up than for the P-doped OF. Contrary to the behavior of the P-doped OF, in this case the RIA value (at the same dose) increases with dose rate.

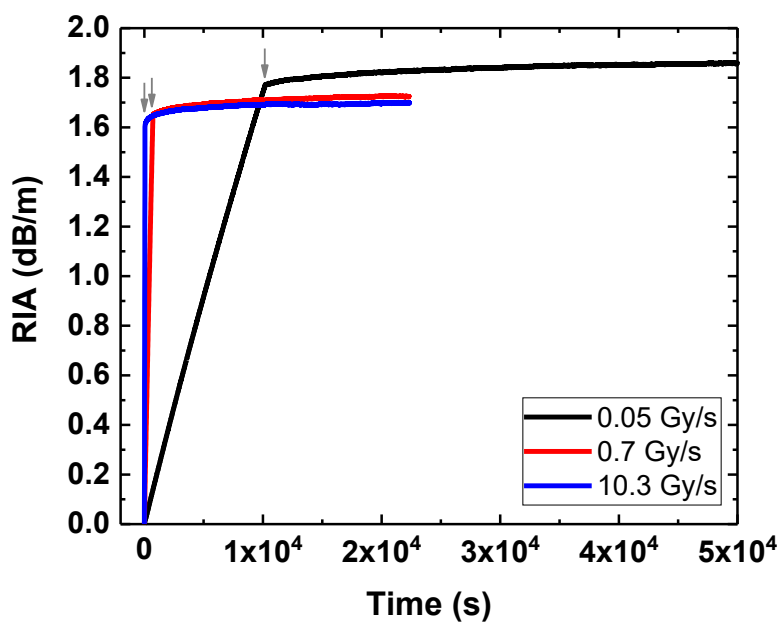


Figure 3.3 Comparison of RIA growth kinetics at 1550 nm of P samples irradiated up to 500 Gy at three different dose-rates as a function of the time. The grey arrows indicate the end of the irradiation.

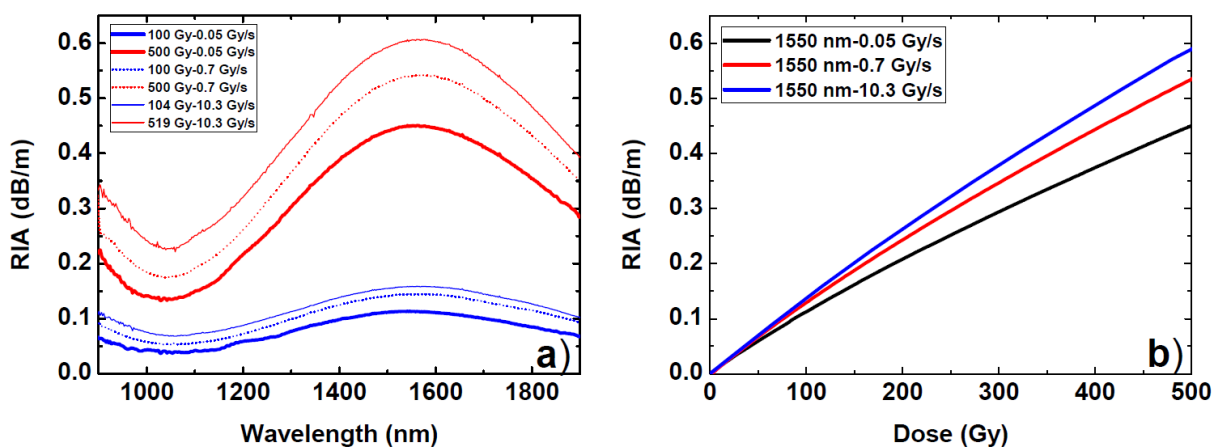


Figure 3.4 RIA spectra of PCE-doped OF at three different dose-rates at cumulated doses of 100 and 500 Gy a); RIA growth kinetics at 1550 nm of PCE sample irradiated up to 500 Gy at three different dose-rates as a function of the dose b).

This effect can be even better seen in Figure 3.5 where the RIA value after irradiation is also shown. For this fiber a spontaneous recovery at the end of irradiation is evident; it seems to be faster at the beginning and then appear to slow down at longer times.

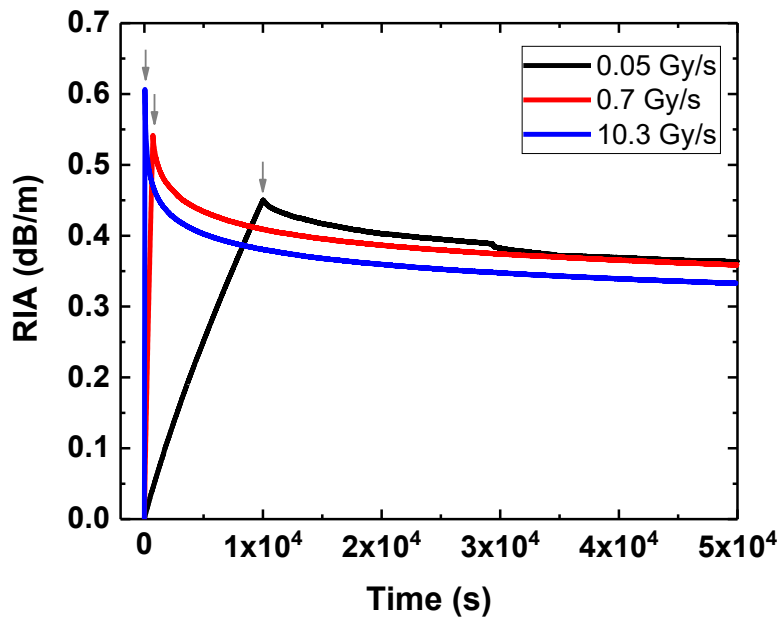


Figure 3.5 Comparison of RIA growth kinetics at 1550 nm of PCE samples irradiated up to 500 Gy at three different dose-rates as a function of the time. The grey arrows indicate the end of the irradiation.

It also appears that for PCE doped fibre the post-irradiation recovery changes with the different dose rates, especially in the first times after the end of irradiation. Higher dose rates seem to correspond to faster initial recovery.

Finally, the results obtained for the Al-doped OF are reported in Figure 3.6 and Figure 3.7. Here, the trend is similar to the one of the PCE-doped OF, the RIA value is higher for higher dose rates and decreases with it. Of course, in this case, the RIA spectra completely differ from the other two P-doped samples. Indeed, this fiber is more sensitive at 1310 nm than 1550 nm. We report the RIA growth kinetics at wavelengths in Figure 3.6 b). It is noteworthy to point out that the radiation sensitivity of Al-doped fibre is an order of magnitude higher than that of PCE-doped fibre and a factor 2 or 3 higher than that P-doped one.

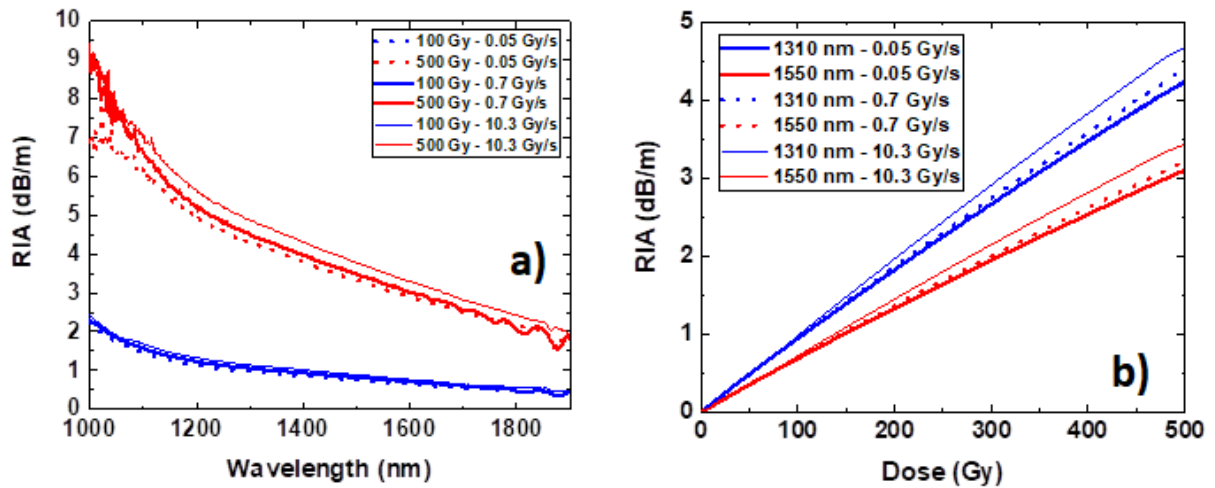


Figure 3.6 RIA spectra of Al-doped OF at three different dose-rates at cumulated doses of 100 and 500 Gy a); RIA Growth kinetics at 1550 nm of Al sample irradiated up to 500 Gy at three different dose-rates as a function of the dose b).

As with PCE-doped fibre, spontaneous recovery, although less pronounced, seems to be faster in the early phase and at higher dose rates, and then the recovery slows down at longer times.

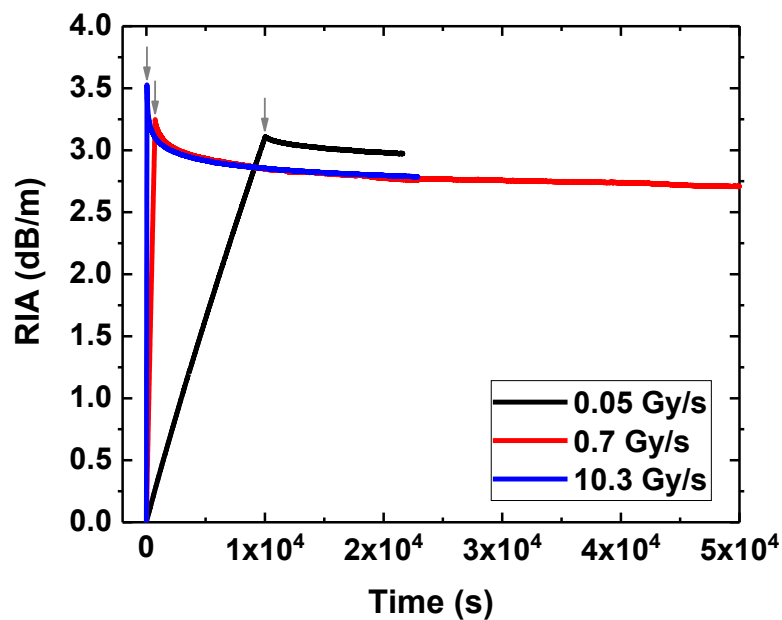


Figure 3.7 Comparison of Growth kinetics at 1550 nm of Al samples irradiated up to 500 Gy at three different dose-rates as a function of the time. The gray arrows indicate the end of the irradiation.

3.2.3 Effect of successive irradiations

In this section we present the results obtained performing consecutive X-ray runs with the aim of studying the three fibers' performances when subjected to different cycles of irradiation and verifying their behavior (*spontaneous recovery*) between the various cycles. We first present the results concerning the P-doped OF which is of primary importance from an application point of view, and then the results of the experiments carried out on the two other samples.

We studied the responses of the fibers when they are irradiated several times consecutively, varying the dose rates for the different irradiation phases. Here again, the dose-rate was modified by varying the X-ray tube current. In this way, the setup was not touched during the whole experiment series, reducing the uncertainties of our RIA measurement values. First, we have deposited 50 Gy three times at the same dose rate of 0.05 Gy(SiO₂)/s. After, we increased the dose-rate to 0.5 Gy/s and we again deposited 50 Gy three times. Between two irradiation steps, we let the fiber recover at room temperature for 10 min. Finally, we increase the dose-rate to 5 Gy/s for 4300 s to reach higher dose levels. At the end of this final irradiation, we monitored the fiber recovery during the following night. Figure 3.8 illustrates this protocol and the performed multistep measurements. We do not illustrate the RIA recovery in this figure, but after the whole night we observed a small change in the transmission signal at RT. The blue and grey rectangles indicate the three steps at 0.05 Gy/s and 0.5 Gy/s, respectively. In red, indeed, we have the last irradiation step at 5 Gy/s and then the long recovery phase.

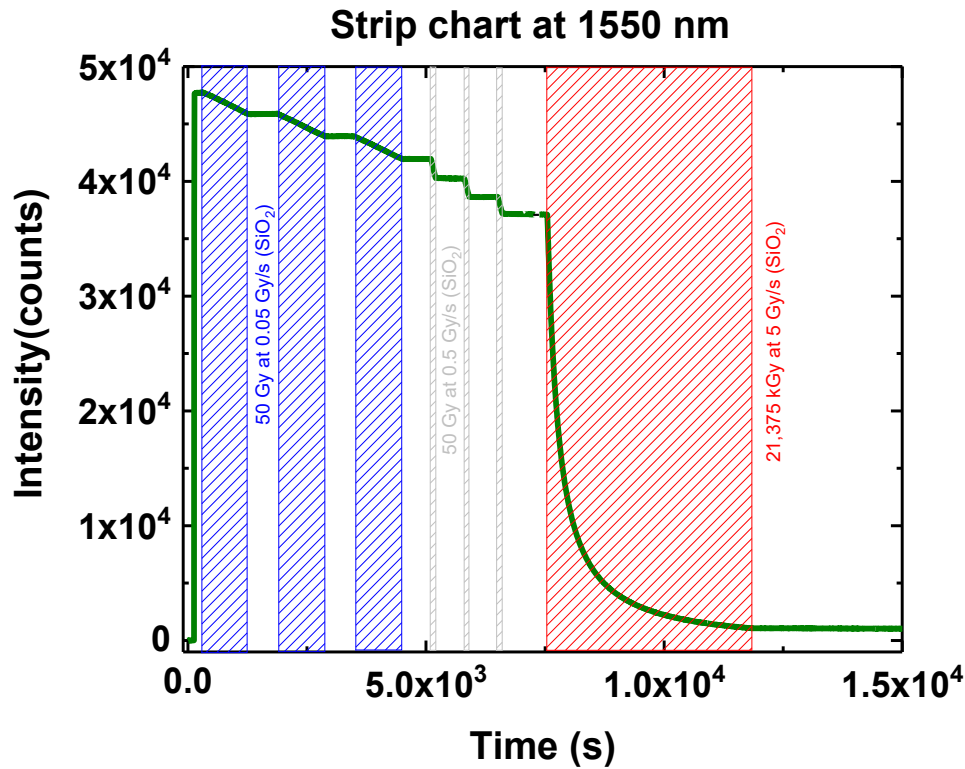


Figure 3.8 Strip chart at 1550 nm of the multi-step irradiation of the P-doped OF.

Figure 3.9 reviews the RIA kinetics measured during each irradiation step, at 1310 nm and 1550 nm. The measurements show a good repeatability of the fiber radiation responses, the larger differences observed at lower doses are probably associated to larger uncertainties in choosing the exact irradiation start time (especially for higher dose rate) or the RIA evaluation due to lower signal to noise ratio. Future additional experiments with longer fiber lengths are needed to better discuss this dose range.

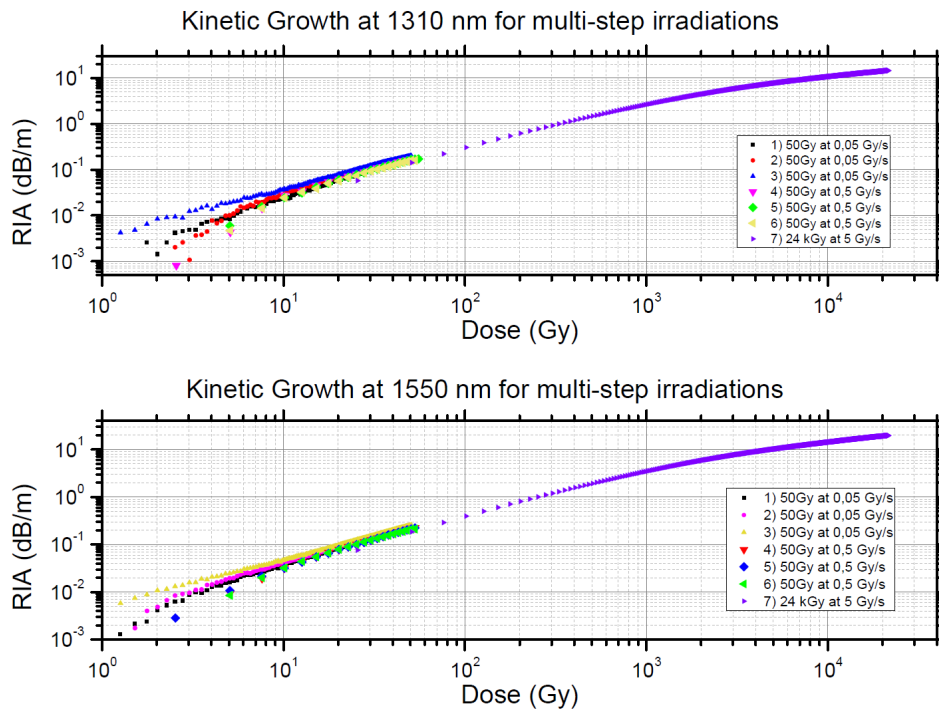


Figure 3.9 RIA Growth Kinetics for the multistep irradiated P-doped OF at three different dose-rates. Three steps at 0.05 Gy(SiO₂)/s, three at 0.5 Gy/s and the last step at 5 Gy/s (Related strip charts data are reported in the previous Figure 3.8).

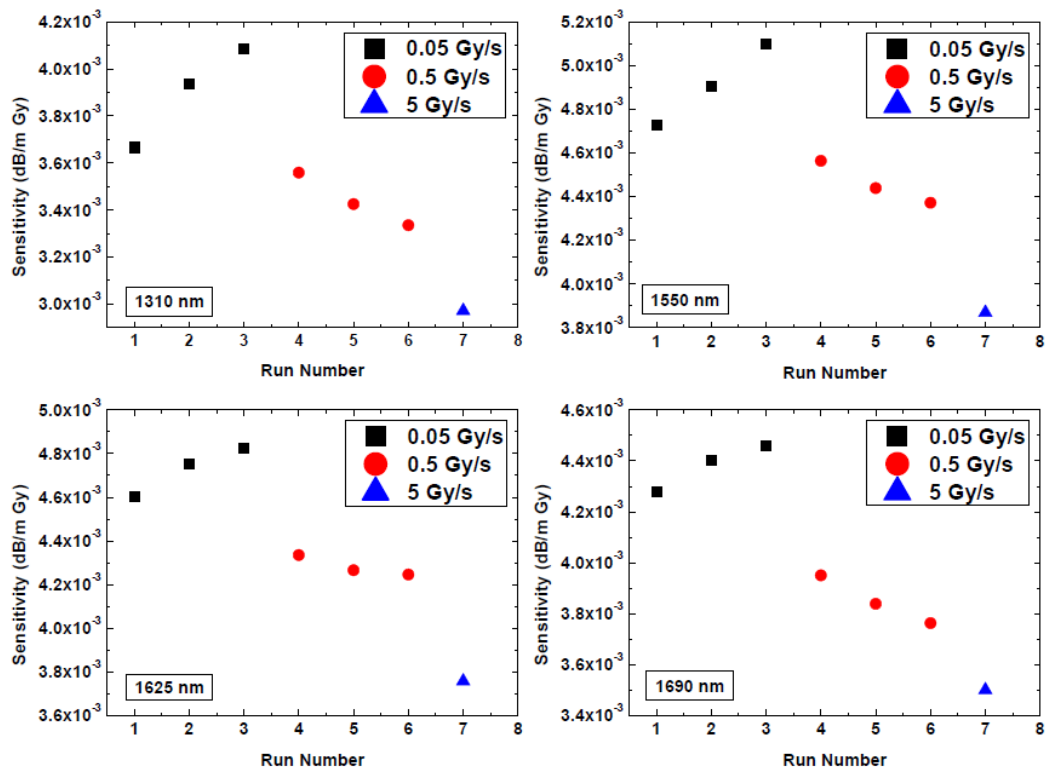


Figure 3.10 Radiation sensitivity of the P-doped OF as a function of the irradiation run numbers for the four wavelengths: 1310 nm, 1550 nm, 1625 nm and 1700 nm.

To study a bit more in depth the behavior of OF's radiation response we made a linear fit of the RIA for every irradiation steps and we report the sensitivity results in Figure 3.10. Concerning the last step at 5 Gy/s we made the fit in the range 0-500 Gy where we know the radiation response of the fiber to be linear. For the first three steps of irradiation at low dose rate, the sensitivity increases at each step then at subsequent irradiations at higher dose rate, the sensitivity decreases at each subsequent step. It is necessary to emphasize that the sensitivity of the fiber has a similar trend at all wavelengths that we studied. This is further confirmation of the hypothesis that in this spectral range RIA is due to a single point defect, the P1.

We repeat a similar experiment for the PCe-doped OF. Even in this case the protocol applied was very close: we deposited 50 Gy three times at 0.01 Gy(SiO₂)/s. After, we increased the dose-rate to 0.1 Gy/s and we deposited again 50 Gy three times. Between two irradiation phases, the fiber recovers for 30 min. Finally, we set the highest dose-rate to 1 Gy/s and quickly deposited again three times 50 Gy. The experiment duration was about 9 hours without considering the whole night of recovery following this last irradiation run. In Figure 3.11 we report the strip-chart recorded at four different wavelengths during the whole experiment as a function of the time; the night recovery is not shown for result clarity. It is evident from the figure that the PCe-doped fiber partially recovers between two consecutive irradiation steps. The 1550 nm RIA growth kinetics of every irradiation steps are compared in Figure 3.12. We can note how after the first few steps of irradiation the fiber radiation response seems more repeatable, especially for the last three steps at the highest dose rate of 1 Gy/s.

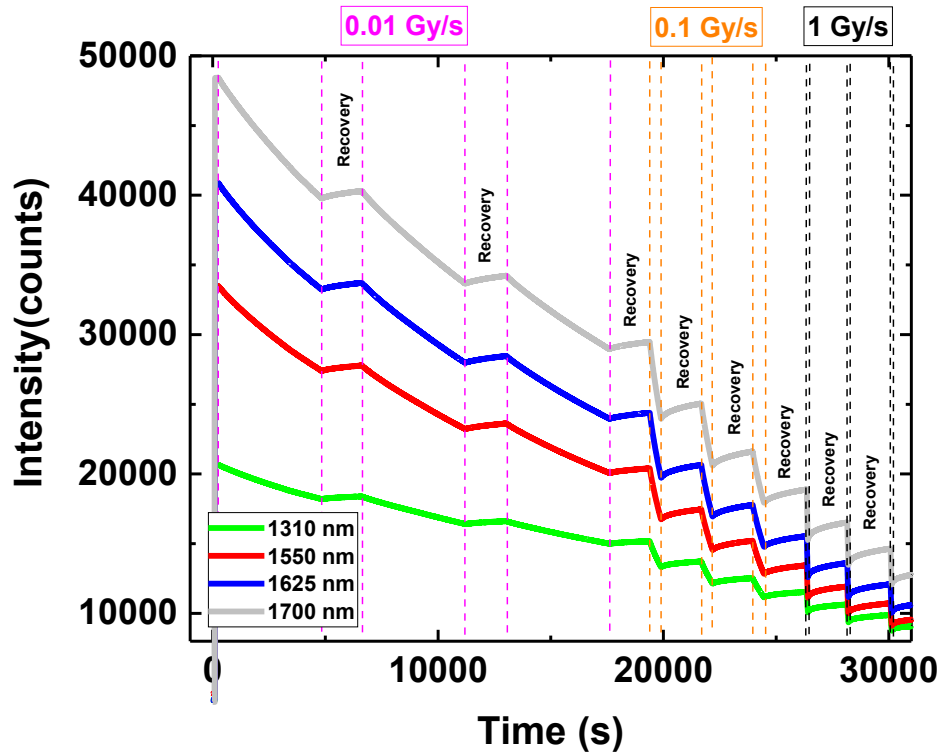


Figure 3.11 Strip chart with four different wavelengths of the multi-step irradiation of the PCe-doped OF.

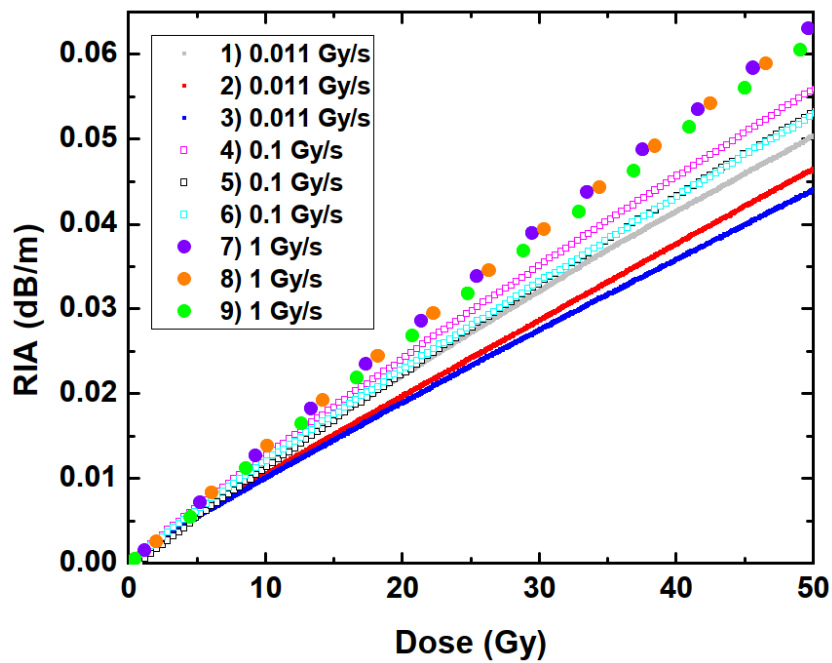


Figure 3.12 RIA Growth Kinetics for the multistep irradiated PCe-doped OF at three different dose-rates. Three steps at 0.011 Gy(SiO₂)/s, three at 0.1 Gy/s and the last three steps at 1 Gy/s (Related strip charts data are reported in the previous Figure 3.11).

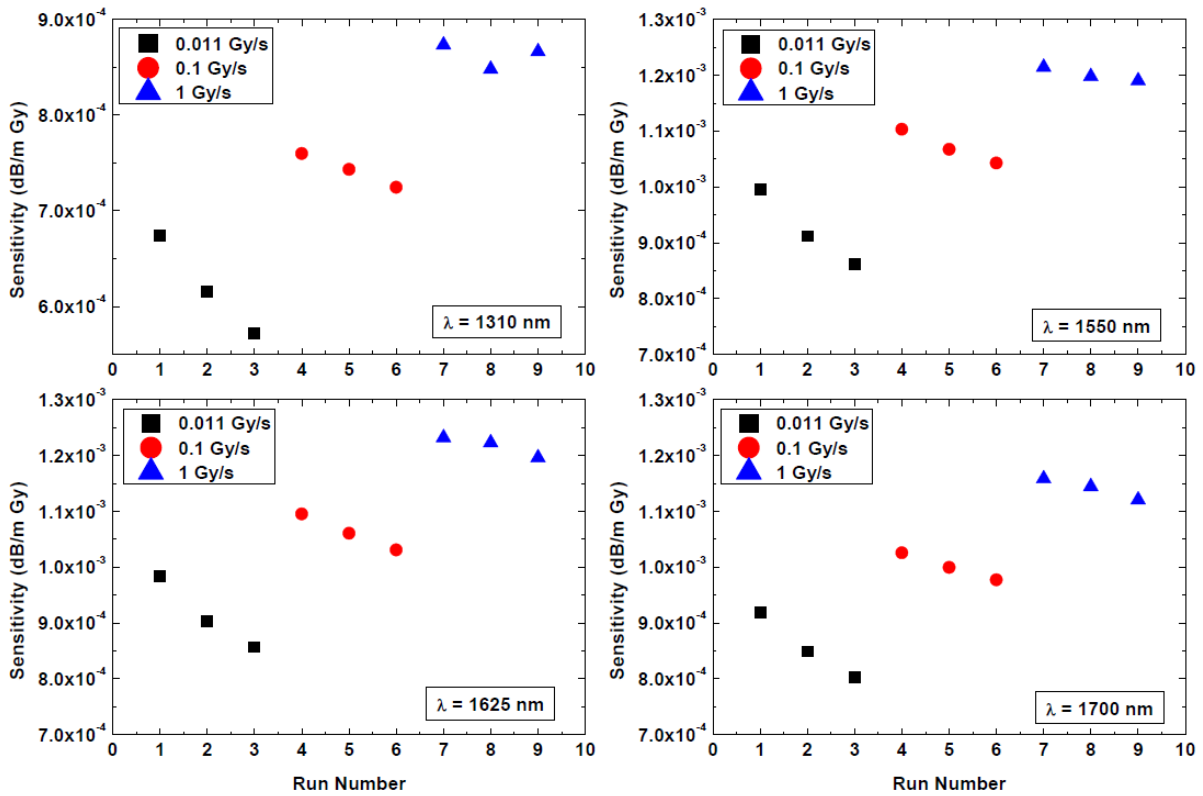


Figure 3.13 Radiation sensitivity of the PCE-doped OF as a function of the irradiation run numbers for the four wavelengths: 1310 nm, 1550 nm, 1625 nm and 1700 nm.

In Figure 3.13 we present the study of the sensitivity for the PCE-doped OF. The sensitivity decreases at each next irradiation with the same dose-rate but when the dose rate increases the starting value is higher with respect the previous ones. The response of fibers co-doped with Cerium differs from the one of the P-doped sample, especially at low dose-rates. Also, for this fiber the sensitivity trend is similar for all wavelengths studied.

The same experiment was performed with the Al-doped OF. In this case the steps at higher dose-rate were four instead of three. The strip charts as function of the time are shown in Figure 3.14 for the four IR wavelengths. From these results, it is clear that a spontaneous recovery occurring between the runs exists but remains lower than for the PCE-doped fiber case.

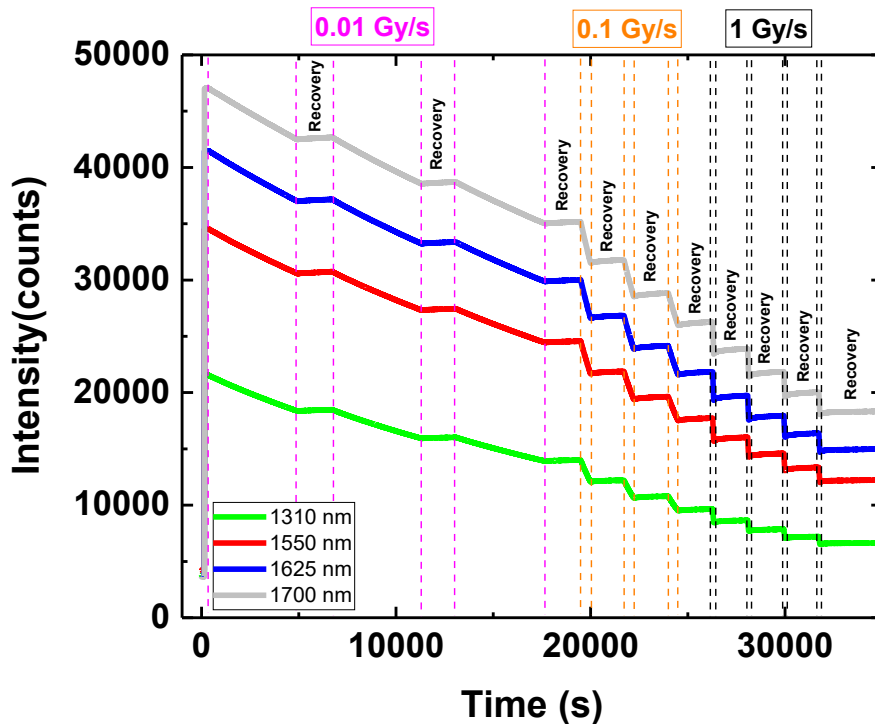


Figure 3.14 Strip chart with four different wavelengths of the multi-step irradiation of the Al-doped OF

With regards to its radiation response at these wavelengths, it seems to be stable during the different phases of irradiation at a constant dose rates; increasing the dose rate the response only slightly changes. Particularly, the RIA value increases as the dose-rate increases. The results showing these features are reported in Figure 3.15.

In Figure 3.16 we report the sensitivity study for the Al-doped OF. Also in this case the sensitivity behaviour is similar at all the studied wavelengths with some irregularity at lower dose-rate. For this fiber, sensitivity also decreases with each successive irradiation at a constant dose rate, whereas when the dose rate increases the starting value also increases. However, it is important to remember that the absorption spectrum of Al-doped fiber, in the studied spectral

range, is not a well-defined absorption band as for the fiber P and PCe cases, but is rather a monotonous curve decreasing with increasing wavelength.

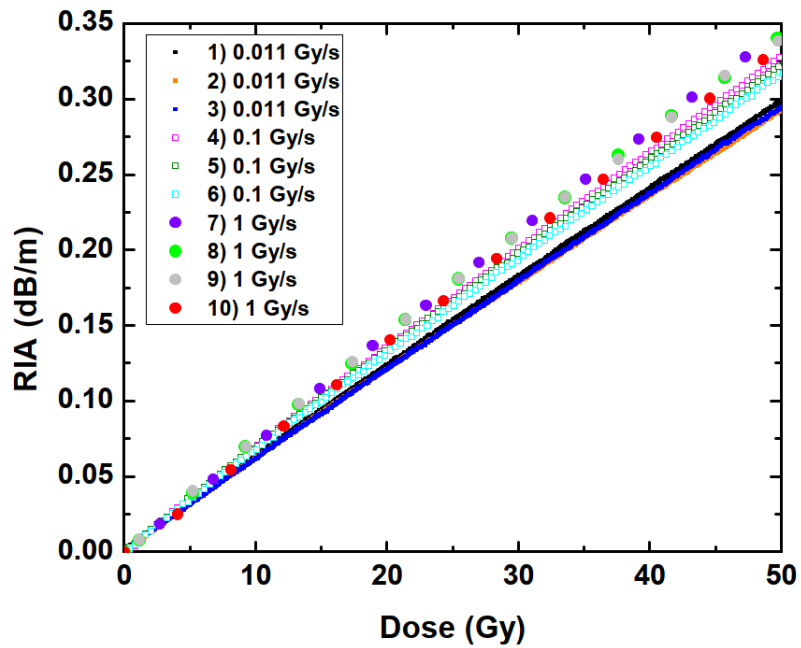


Figure 3.15 RIA Growth Kinetics at 1550 nm for the multistep irradiated Al-doped OF at three different dose-rates. Three steps at 0.011 Gy(SiO₂)/s, three at 0.1 Gy/s and the last four steps at 1 Gy/s (Related strip charts data are reported in the previous Figure 3.14).

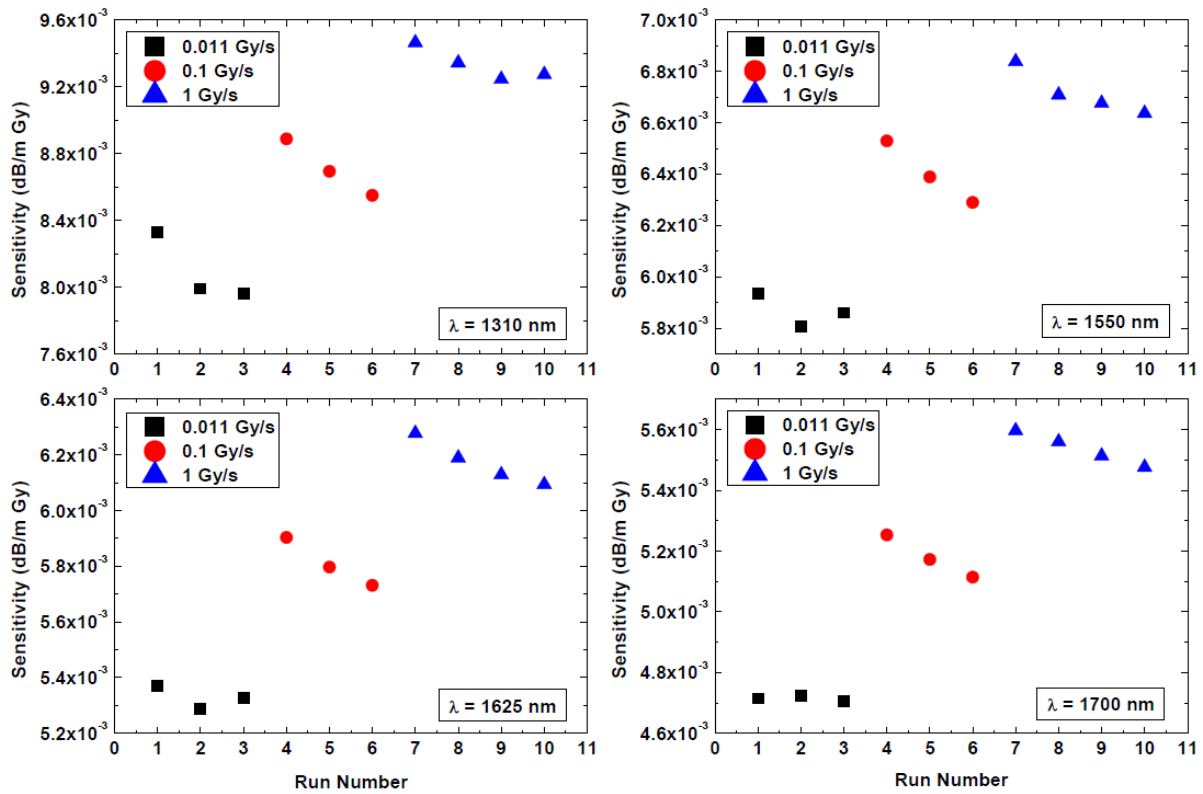


Figure 3.16 Radiation sensitivity of Al-doped OF as a function of the irradiation run numbers for the four wavelengths: 1310 nm, 1550 nm, 1625 nm and 1700 nm reported in Figure 3.14 and Figure 3.15.

To give a general idea of the results presented in this section, we compare the sensitivity of the three fibers at each of the four IR wavelengths. In Figure 3.17 we report, at various wavelengths viewed, the behaviour of our fibers at the successive irradiation steps at three different dose-

rates. Always in Figure 3.17 we report the average value (dashed line) and the variation interval of $\pm 10\%$ (solid line) within which all our results fall.

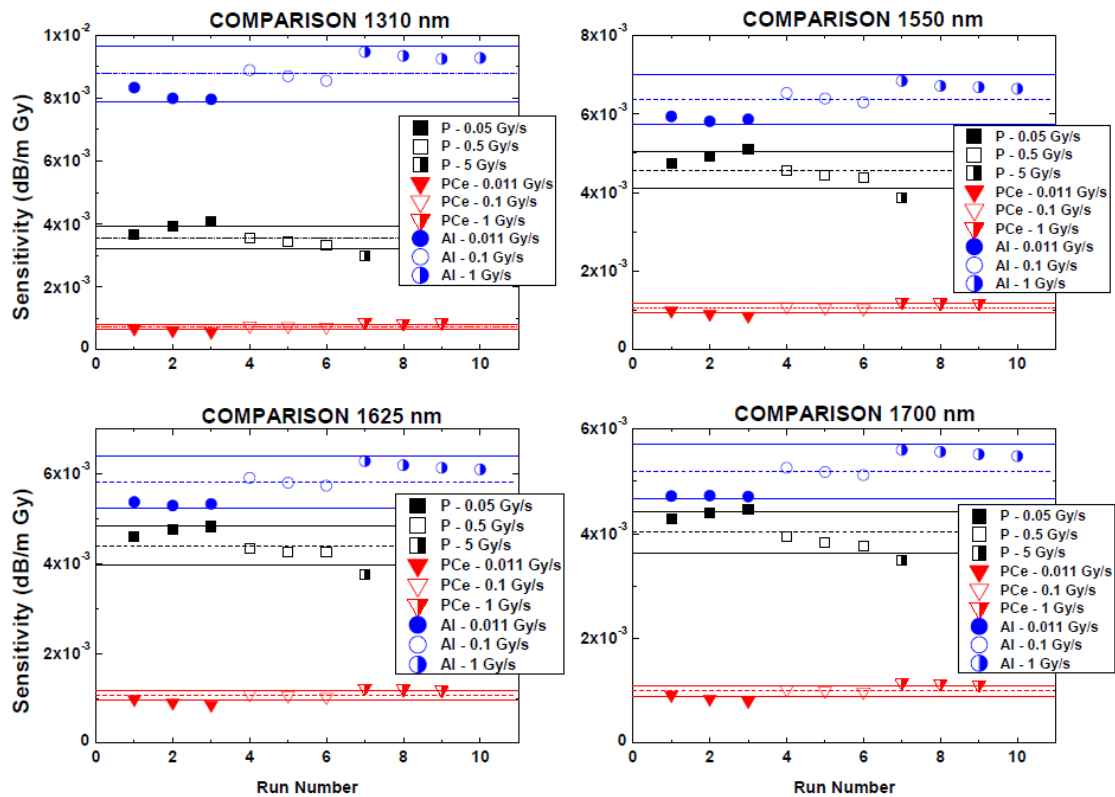


Figure 3.17 Comparison of the radiation sensitivity per wavelength for the three different OFs. The sensitivity average value is reported in the pictures (dashed line); the interval of $\pm 10\%$ of average value are even reported (solid line) for every wavelength of any sample.

Summary: Studying the impact of successive irradiation of the same sample conducted on all three fiber types reveals that their sensitivity changes into an interval of 10% with respect to the average value during the successive runs. The only value outside this 10% range is the last step irradiation of the P-doped sample but in this case larger final dose of 500 Gy was considered (instead of 50 Gy for the other fibers). We have even to note the different behaviors between the P-doped fiber, our reference, and the other two OFs. Further studies are needed to better understand the behavior of these fibers to successive irradiations especially during the recovery phases.

3.2.4 Temperature dependence for CERN applications

To test the stability response of the P-doped OF in the temperature range of interest for application at CERN, we carried out the following experiment irradiating several samples at temperatures ranging from room temperature (RT) up to 45 °C. The irradiations were performed with the X-ray machine at LabHC. During the three different experimental tests, the dose rate was always kept constant at 0.01 Gy(SiO₂)/s (estimated uncertainty 5%), whereas the irradiation temperature was varied. For the temperature monitoring, we used the TC-08 Thermocouple Data Logger of the “pico Technology” whereas the PicoLog 6 data logging software for TC-08 was used for the data acquisition, with a time acquisition of 1 s. Two thermocouples were used, one at the heating plate and another one to monitoring the temperature in the irradiation chamber.

In experiment 1 (exp. 1 in Figure 3.18), the RIA was performed at room temperature and it should be considered as the reference RIA test. In experiment 2 (exp. 2 in Figure 3.18), the fiber was stabilized at 35 °C for the whole duration of the experiment. In experiment 3 (exp. 3 in Figure 3.18), the irradiation started at room temperature, after 2000 s, the temperature was increased up to 35 °C and kept at this level for 4000 s. Subsequently, the temperature was further increased to 45 °C for additional 4000 s. Once the irradiation stopped, the temperature was maintained at 45 °C for the first 5000 s, whereas we let the heating plate cooling down afterwards. During the three experiments, the temperature measurement at the sample location was recorded with the TC and it is reported in panel a) of Figure 3.18. In panel b), we show the RIA growth kinetics at 1550 nm recorded with the OTDR.

The RIA response of the P-doped fiber under test is not influenced by the change of the irradiation temperature. Within the repeatability of the RIA experiment, it is not possible to discriminate the three RIA plots. It is also important to notice that no sign of recovery can be detected after the end of the irradiation even when the temperature is increased up to 45 °C.

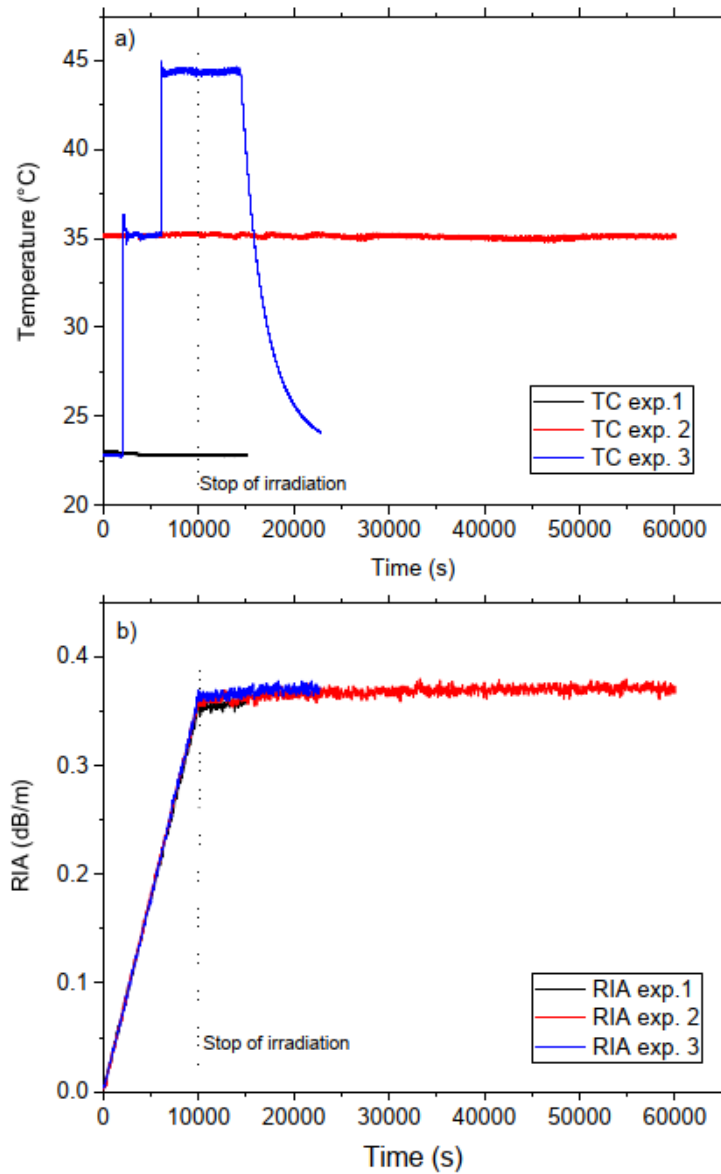


Figure 3.18 X-rays irradiation tests at different temperatures on the P-doped SMF. In panel a), we plot the temperature variation as a function of the time, whereas in panel b) we report the corresponding RIA growth kinetics at 1550 nm during the irradiation and its evolution after the irradiation stop [91].

Another test campaign was carried out to study the radiation response of the other two fibers of interest as a function of temperature. We took the opportunity to retest the fiber doped with phosphorus and use it as a reference for the other two fibers. In Table 3-1 we report the lengths of the irradiated samples. In the experiments, we recorded the transmitted spectra from which

it is possible to obtain the RIA by comparing the spectrum before the start of the irradiation with the ones at later times and applying Lambert-Beer law.

Table 3-1 Lengths of the samples and core dopant percentages of the CERN SMOFs used in the experiments [46].

Sample	RT Length (m)	35°C Length (m)	50°C Length (m)
P	0.606	1.53	1.525
PCe	20.24	20.25	20.51
Al	1.175	1.712	1.717

Figure 3.19 a) reports the RIA growth kinetics at the wavelengths of interest at all investigated temperatures for the P-doped OF. The investigated temperature change does not affect the IR (>1300 nm) radiation sensitivity as shown by the ratios between the spectra recorded at 100 Gy for the samples irradiated at 35 °C and 50 °C and the one acquired at RT.

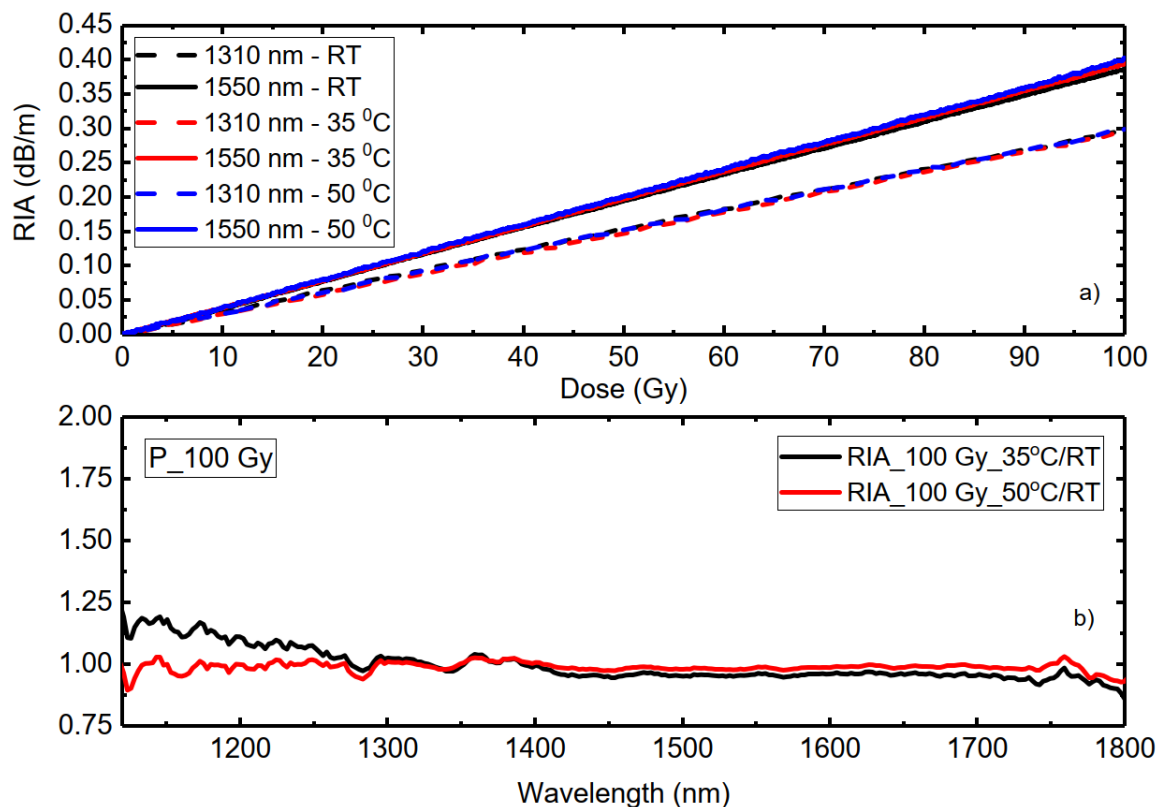


Figure 3.19 a) Dose dependence of the RIA at 1310 nm and 1550 nm for the P-doped OF; b), Ratios between the acquired RIA spectra at 35°C and 50°C and the one acquired at RT; a dose rate of 0.01 Gy/s was used for all irradiations[46].

The PCe fiber shows its greatest sensitivity at 1550 nm. The spread that we can see in Figure 3.20 a) is larger than the experimental error. We observed a decrease of the RIA at increasing temperature of irradiation. The RIA value at 50 °C is about 9% lower than the RT value. From Figure 3.20 b), it is evident that the RIA below 1100 nm is the largest at 35 °C.

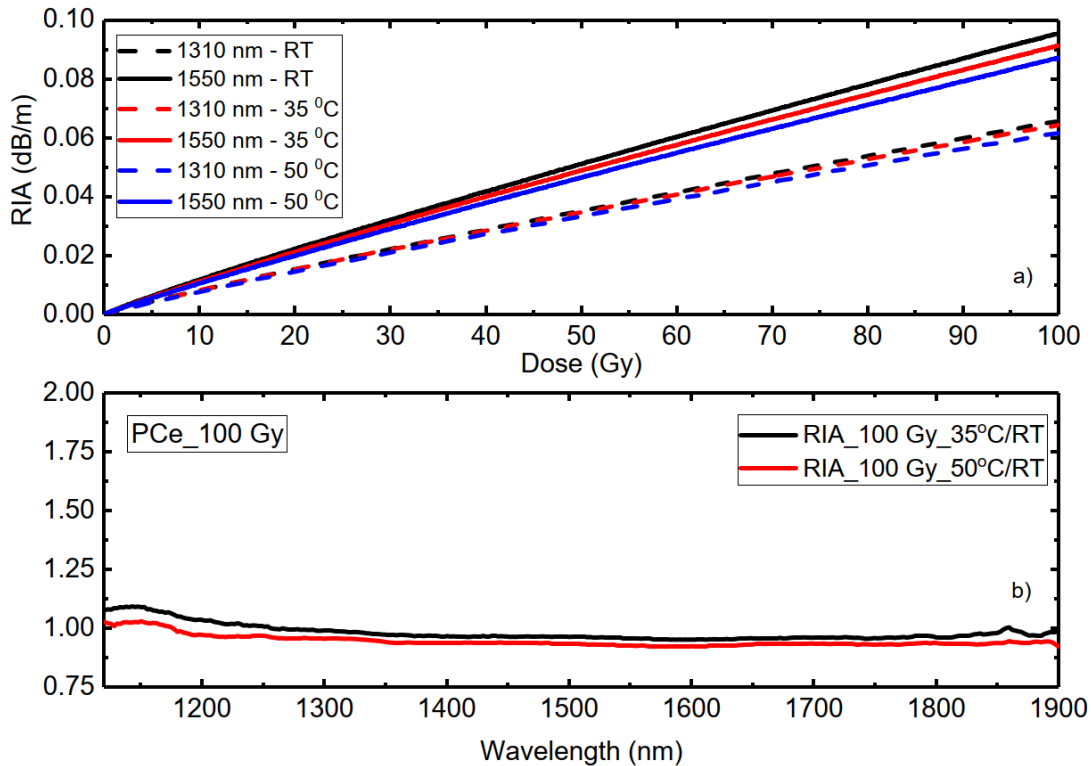


Figure 3.20 a) Dose dependence of the RIA at 1310 nm and 1550 nm for the PCe-doped OF; b), Ratios between the acquired RIA spectra at 35°C and 50°C and the one acquired at RT; a dose rate of 0.01 Gy/s was used for all irradiations [46].

Finally, in Figure 3.21, we report the same measurements on the Al-doped OF. Its behavior differs from the ones of P-doped fibers. This fiber is more sensitive at 1310 nm than 1550 nm. At 1310 nm, the 10% lower radiation sensitivity at 35°C and 50°C with respect to RT is comparable to the experimental error of the data recorded for this fiber (*see previous reported consideration*). Therefore, it is not possible to clarify from our data set if this effect is real or not, anyway if present this temperature effect has a slight impact. This is even more evident in Figure 3.21 b) where there is no difference in the ratio between the spectra acquired at 35 °C and 50°C and that one at RT.

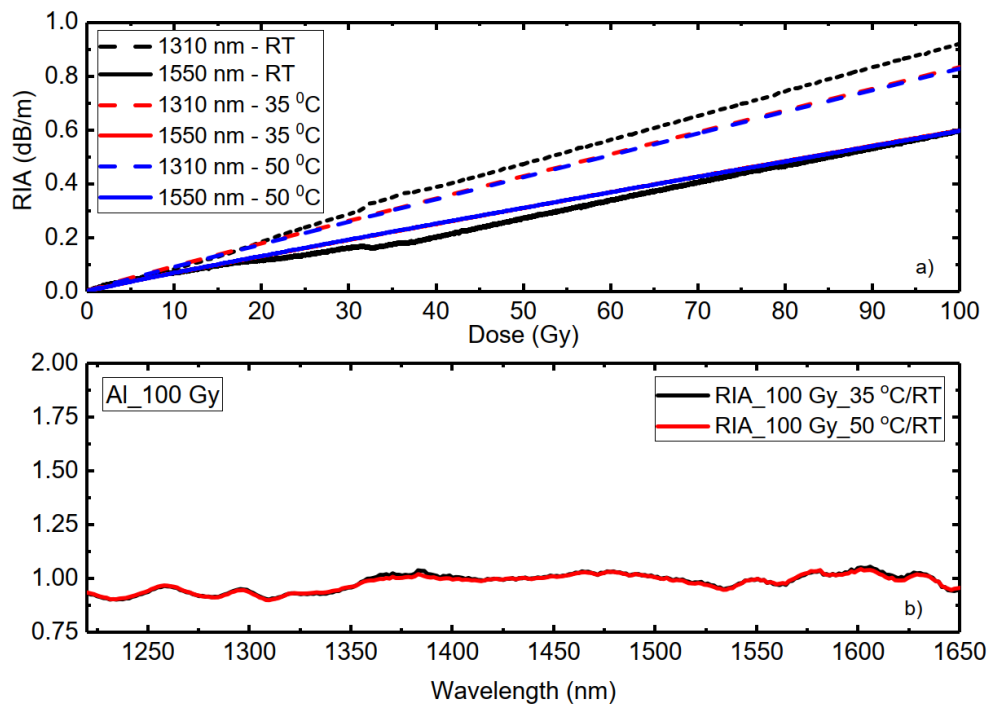


Figure 3.21 . a) Dose dependence of the RIA at 1310 nm and 1550 nm for the Al-doped OF; b), Ratios between the acquired spectra at 35°C and 50°C and the one acquired at RT; a dose rate of 0.01 Gy/s was used for all irradiations [46].

3.2.5 Temperature dependence of P-doped fiber from -80°C to 300°C

Those results have been published in the journal article [114]: A. Morana, C. Campanella, E. Marin, G. Mélin, T. Robin, G. Li Vecchi, et al., “Operating Temperature Range of Phosphorous-doped Optical Fiber Dosimeters exploiting Infrared Radiation-Induced Attenuation”, IEEE Transactions on Nuclear Science, 68(5), May 2021, pp 906 – 912 10.1109/TNS.2021.3053164 (ANNEX 2)

In [114], we investigate the temperature dependence of the radiation-sensitivity coefficients at 1550 nm (expressed in $\text{dB km}^{-1} \text{Gy}^{-1}$) of three phosphorus-doped single-mode optical fibers between -80°C and 300°C for TID ranging from 1 Gy to 1 kGy(SiO_2). Our measurements reveal the same temperature dependence of the calibration factor for the three fibers at the higher temperatures ($>120^\circ\text{C}$) where the P1 defects, at the origin of the IR-RIA, are metastable. However, the uncertainties on the TID measurements through the fiber-based dosimeter remain within the 15% for temperatures ranging from -80°C to 120°C for the three tested fibers. We

report in this paragraph the result obtained for a P-doped SMOF from iXblue, very close in terms of properties to the one discussed along this PhD thesis. Figure 3.22 reports the RIA (*measured with a white light source and a spectrometer [114]*) as a function of the dose during the various irradiation runs at different temperatures and as a function of the time after the irradiations end for the P-doped SMOF. For all the tested temperatures, the linear dependence of RIA with dose is maintained, whereas a slight change in the fiber sensitivity (*calculated through the slope of the RIA vs Dose curve*) is mainly observed. A particular behaviour is recorded above 200°C with a clear RIA reduction during the irradiation and an accelerated RIA recovery after the irradiation ends. No rapid recovery effect is evident after the irradiation end for temperatures up to 120°C: a slight RIA increase lower than 2% is observable after the irradiation end. Such phenomenon has already been reported in P-doped fibers and explained by a conversion mechanism of the POHCs absorbing in the UV-visible to IR-absorbing P1 defects [33].

For irradiation temperatures higher than 120°C, RIA at 1550 nm clearly decreases after irradiation: the bleaching efficiency increases with the temperature. Such result differs from the one reported by Griscom et al., who observed an increase of the P1 concentration when applying a thermal treatment at temperatures up to 300°C after an irradiation at 77 K [33]. However, we know that radiation and temperature combined effects are different from the ones observed by applying a thermal treatment after an irradiation performed at another temperature, in most cases RT [65]. Indeed, high irradiation temperature could cause the thermal bleaching of defects, as one can imagine and as it is observed during a post-irradiation treatment. However, the temperature can also induce defect conversion: from an unstable to a more stable one at the investigated temperature, as for the POHCs into P1 defects [65].

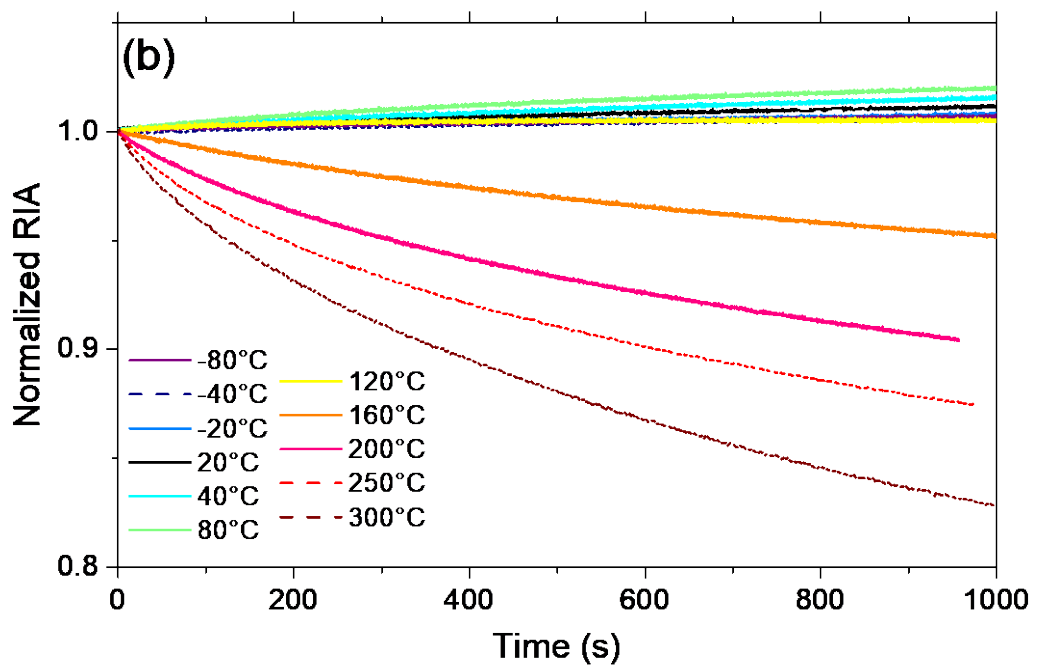
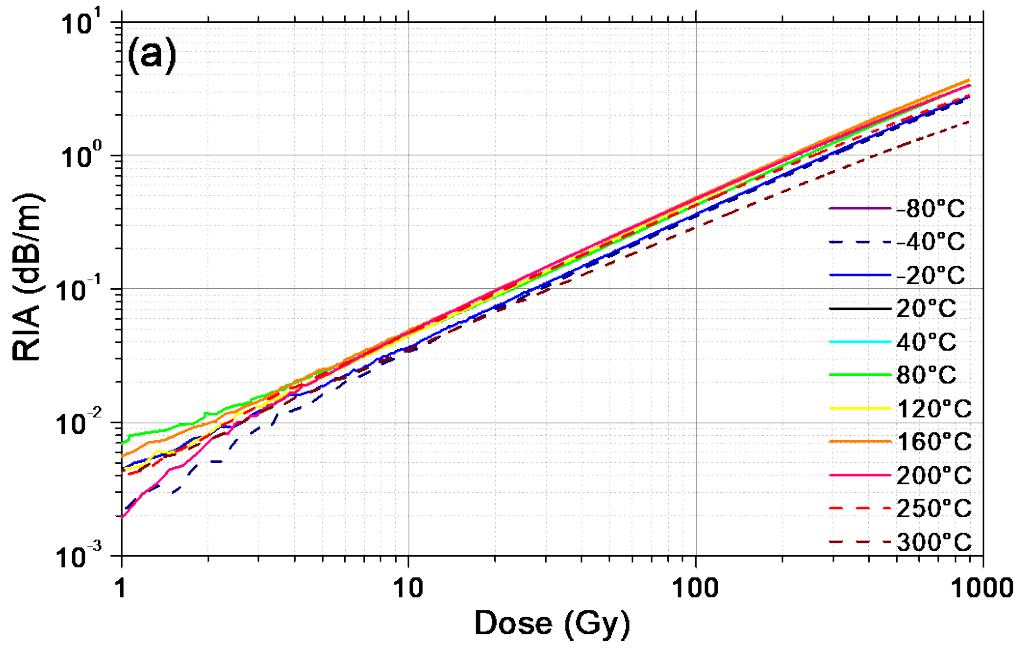


Figure 3.22 (a) 1550nm RIA as a function of the dose for different irradiation temperatures, up to TID of 1 kGy, dose-rate being 1 Gy/s, for the P-doped SMOF. (b) Normalized RIA time evolution after the irradiation end.

Figure 3.23 highlights the temperature dependence of the radiation-sensitivity coefficient of this fiber. This was obtained as the mean value of the slopes of several linear fits performed on different dose ranges, up to the TID of 300 Gy. The associated error is the standard deviation.

The results agree with the preliminary measurement done on the CERN P-doped fiber on a reduced temperature range: its sensitivity of $\sim 4 \text{ dB km}^{-1} \text{ Gy}^{-1}$ does not vary between 20 and 45°C. Moreover, the sensitivity does not change, within the associated error bars, for temperatures up to 80°C. As shown in this figure, the sensitivity increases with the temperature from -80°C to 160°C and decreases at higher temperatures. The sensitivity coefficients are within 10% only for temperature between -40°C and 80°C. Even if our experiments were all performed with the same conditions, it is important to note that the dosimetry of the MOPERIX irradiation chamber has an uncertainty of $\sim 10\%$.

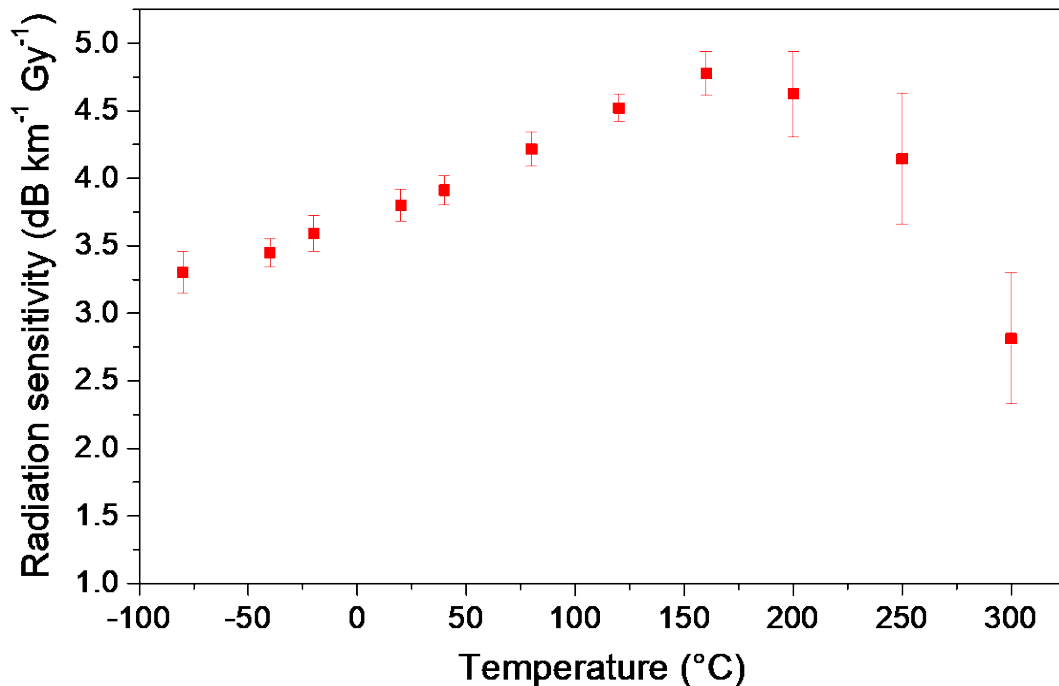


Figure 3.23 Radiation sensitivity of the iXblue P-doped SMOF calculated for doses lower than 300 Gy, as a function of the temperature.

To emphasize the effects of a calibration performed at different temperatures or in different temperature ranges, Figure 3.24 displays the sensitivity estimated varying the temperature range. The value was calculated by performing a linear fit on data set constituted by the ones at the temperatures between the extreme values of the range, whereas the associated bar is the maximal variation between the coefficients related to the different considered temperatures. Results obtained at temperatures higher than 120°C were not considered, since the observed temperature effects already invalidate the good performances of the dosimeter.

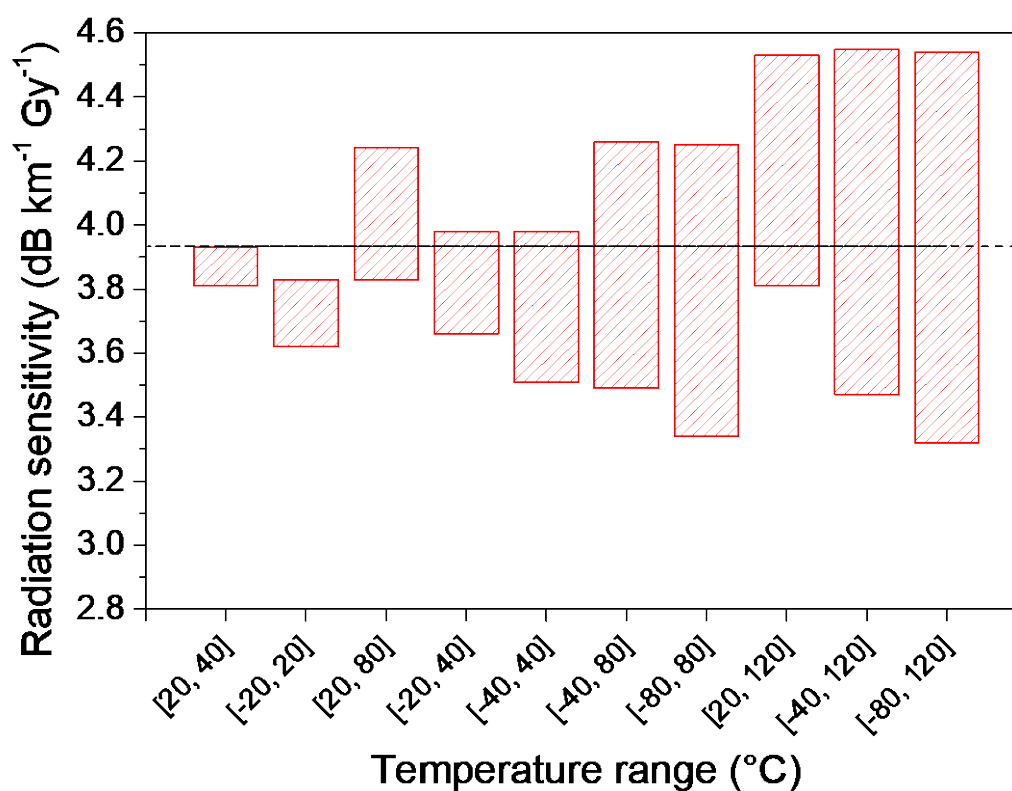


Figure 3.24 Radiation sensitivity evaluated in different temperature ranges for the P-doped SMOF. The line represents the mean value obtained for the larger range, between -80 and 120°C. The bars, instead, put in evidence the sensitivity variation range.

The sensitivity varies in the different temperature ranges and the associated variation bars increase when the extreme values are taken into consideration, above all -80°C and 120°C. However, such variations, in the worst case, are lower than 15%.

3.3 Discussion of the dosimetry potentials of the three fibers

We summarize the main characteristics of the three studied OF and briefly discuss about their potential for the design of radiation detectors or even dosimeters:

- All the fibers present a strictly monotone IR-RIA dependence At constant dose rate in the investigated dose range (linearity up to 500 Gy for the P-doped optical fiber) and can serve as radiation detectors.
- We observed no 1550nm RIA recovery after irradiation for the P-doped optical fiber; for the other two fibers doped with PCe and Al we found a significant post-irradiation recovery that tends to slow down over time. This absence of recovery is a strong advantage for dosimetry with P-doped fibers.
- concerning the dependence of the RIA to the dose rate; only a slight dose rate dependence is observed in the here reported experiments for the P and Al-doped fibers in the range studied; the dependence is more pronounced for the PCe fiber,. It should be noted that in [91], precise measurements under γ -rays showed that the P-doped fiber presents negligible dose rate dependence in the 0.048 to 5.76 mGy/s range. Regarding this parameter too, the P-doped fiber appears today as the most adequate candidate for dosimetry.
- P-fiber showed a radiation sensitivity independent of the fiber history (pre-irradiation) while PCe and Al-doped fibers exhibit a non-negligible spontaneous RIA recovery that strongly limits their its use as dosimeters;
- The P-doped fiber shows robustness against the effect of photo bleaching at 1550 nm during reported measurements and experiments;
- The P-doped fiber shows almost no dependence of the infrared RIA on the irradiation temperature in the 20 to 45 °C range.

All the mentioned properties were mostly investigated at 1550 nm, typical working wavelength of OTDR interrogators. At this wavelength we found a radiation sensitivity of $\sim 3.9 \pm 10\%$ dB·km⁻¹·Gy⁻¹ (SiO₂) for the P-doped optical fiber up to 500 Gy(SiO₂) in the -80°C – 120°C temperature range. Figure 3.25 compares the different responses of the three fibers to radiation at different dose-rates and the different behaviors of the various fibers at the end of irradiation (*spontaneous recovery*).

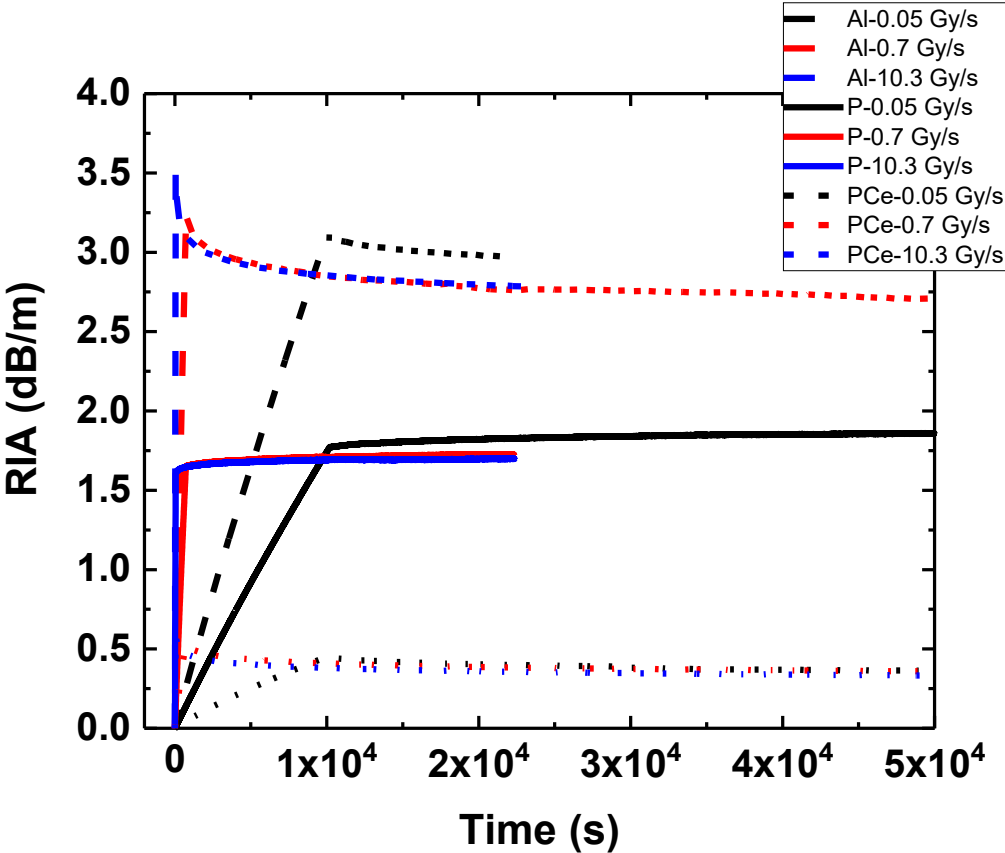


Figure 3.25 Comparison of the RIA growth kinetics at 1550 nm for the three samples irradiated up to 500 Gy at three different dose-rates.

Summary: The RIAs of the three different radiation sensitive OFs have been characterized under X-rays at three different temperatures. The first important result concerns the absence of a temperature dependence of the RIA at both 1310 and 1550 nm in the P-doped fiber, in the studied temperature range of interest for CERN (RT-50 °C), reinforces the idea to use it as radiation dosimeter [91,115]. Furthermore, we highlight that the RIA dose dependences of this OF showed no temperature dependence over the whole 1300 to 1800 nm spectral range. At shorter wavelengths, we observed a RIA increase at 35 °C compared to RT. This effect may correspond to the existence of an absorption band related to temperature-sensitive defects in this spectral region [47,116]. Further experiments are needed to better understand this effect.

For the Al-doped optical fiber, our experiments showed that this type of fiber is the most radiation sensitive around 1550 nm. Its dosimetric properties are less adapted than the ones of P-doped fibers due to a slight dose rate dependence and to a non-negligible RIA recovery post-irradiation.

For the PCe-doped fiber, we note a temperature effect on the IR-RIA larger than the error associated to its measurement. We can see a decrease of the radiation sensitivity of this fiber of about 9% when the irradiation temperature increases at 50 °C. The RIA value at 100 Gy for this fiber is about 4 times lower than in the P-doped sample. This is attributed to the presence of Ce co-dopant, which probably partially inhibits the formation of P1 defects [36] as it was previously observed in PCe-co-doped Erbium/Ytterbium OFs [117].

4 Chapter IV. P-doped Fiber Dosimetry in different radiation fields

4.1 Experiments done at CERN facilities

In this part of the work, we investigated the potential of the distributed fiber optic sensor to monitor the total ionizing dose in mixed field that is associated with complex radiation environments combining different types of radiation. Such complex environments are often encountered at CERN, for example in the Proton Synchrotron Booster (PSB) or in the Proton Synchrotron (PS) or around the LHC. To perform this investigation, we first performed preliminary passive investigations on the different classes of radiation-sensitive optical fibers (§ 4.1.1). As the P-doped fiber appeared as the best candidate, we then performed combined experiments at the CERN CHARM facility (see Chapter 2.3.1), with the P-doped based distributed dosimeter (§ 4.1.2).

4.1.1 Investigations based on post mortem measurements

For passive experiments done in CHARM on our radiation sensitive optical fibers, we calculate the errors done by comparing the dose evaluated through the fiber samples to those given by two different sets of RPLs installed with our fiber samples. The first set of RPLs was placed in the same bag as our samples during the experiment, while the second set of RPLs was installed in the same location as ours during the calibration of the facility, in the configuration used. We must remember that the RPL dosimeters have been calibrated with a ^{60}Co source, so in CHARM their measurements can be less accurate (25% error). We must distinguish between the measurements made at position T0 and those on the rack in position 13, see those positions in Figure 4.1. In the latter case, the radiation field is much more homogenous and we associate an error of about $\pm 3\%$ to the RPL measurements. In T0 position, we have a significant gradient

of field and consequently the uncertainty on the dose is larger. Probably the largest contribution, given the presence of a strong gradient, is due to a small difference in positioning of the samples on the table. We associate an error of about $\pm 25\%$ at measurements done on the table. In any case, remembering that in CHARM we have a mixed field, be aware that the RPL results give the photon dose in air (dosimeters are calibrated with Co-60 source) and the resulting effect is compared to the calibration curve to estimate the measured dose.

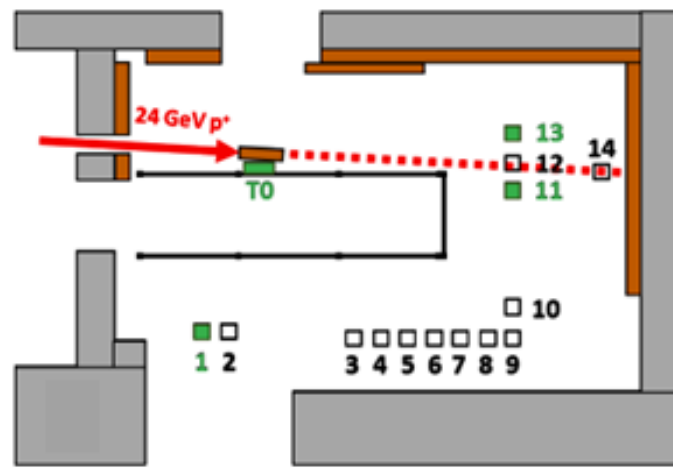


Figure 4.1 Schematic layout of the CHARM facility with the names of the locations for sample testing.

Below we show the results of the post mortem attenuation measurements of samples irradiated at different doses in the CHARM facility. In Figure 4.2 we report a semi-logarithmic optical attenuation spectrum at different doses. The measurements were carried out with the cut-back technique described in 2.4.2. We notice that the RIA spectra are a bit different at the lower doses. The selected sample length was too small to get a good measurement.

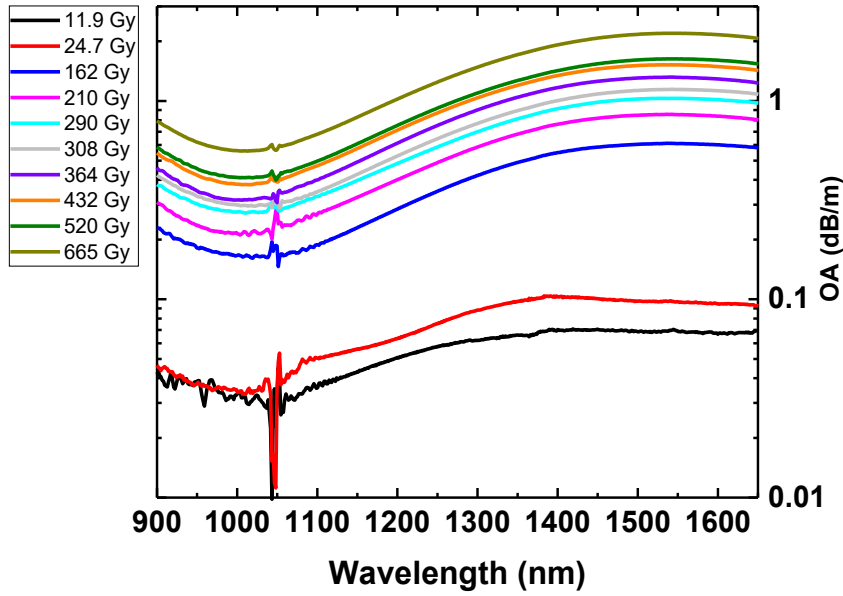


Figure 4.2 RIA spectra at different doses of the P-doped sample which was irradiated in CHARM.

In Figure 4.3 a) and b), we plot the dose dependence of the RIA acquired at 1310 nm and 1550 nm respectively. We made a linear fit of these points and the value of the slope of the straight line gives us the sensitivity of the fiber at that wavelength. The fits were made imposing the passing to 0.00105 dB/m (1.05 dB/km) and 0.00266 dB/m (2.66 dB/km), which correspond to the pristine attenuation of the OF at the wavelength of 1310 nm and 1550 nm, respectively.

The extracted values for the radiation sensitivity coefficients are:

- $2.24 \pm 0.08 \text{ m dB m}^{-1} \text{ Gy}^{-1}$ at 1310 nm;
- $3.23 \pm 0.1 \text{ m dB m}^{-1} \text{ Gy}^{-1}$ at 1550 nm;

We also report the fit values imposing the passing to zero, in red. The errors associated with these measurements are those returned by the program used to make the fit, which are obviously an underestimation of the experimental error.

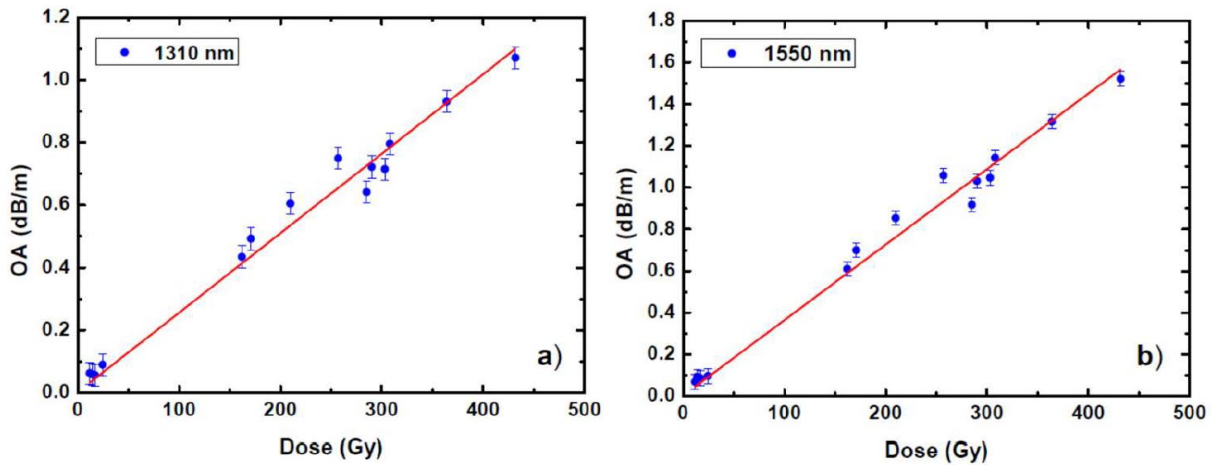


Figure 4.3 RIA values after the irradiation in CHARM for the P-doped sample at 1310 nm in a), at 1550 nm in b) and the respectively linear fit.

Comparing the value found here with those obtained in the online measurement we obtained a good agreement, also remembering that the post mortem measurements were carried out after three months of the irradiation. This is a further confirmation of the spontaneous recovery absence of the P-doped OF.

PCe-doped

Similar radiation tests were carried out for the PCe-doped OF. Based on previous investigations of similar OFs, we must consider that spontaneous recovery processes at room temperature may be present for this OF and a dedicated study is needed before we can associate an error with our measurements. In Figure 4.4 there are the OA spectra of PCe-doped samples that were irradiated at CHARM. The differences between these spectra and those obtained for the P-doped sample are quite evident. With post mortem measurements, this fiber is about 10 times less sensitive, which increases the difficulty of the cut-back measurements on the selected fiber lengths. The linear fit of these points and the value of the slope of the straight line, illustrated in Figure 4.5, gives us the sensitivity of the fiber at that wavelength. The fits were made imposing that at $D=0$,

the losses should be of 0.0086 dB/m and 0.005 dB/m, respectively, which correspond to the pristine attenuation of the OF at the wavelength of 1310 nm and 1550 nm, respectively.

For the PCE-doped fiber, we found that the “post-mortem” sensitivity coefficients are:

- $0.22 \pm 0.013 \text{ mdB m}^{-1} \text{ Gy}^{-1}$ at 1310 nm;
- $0.34 \pm 0.02 \text{ mdB m}^{-1} \text{ Gy}^{-1}$ at 1550 nm;

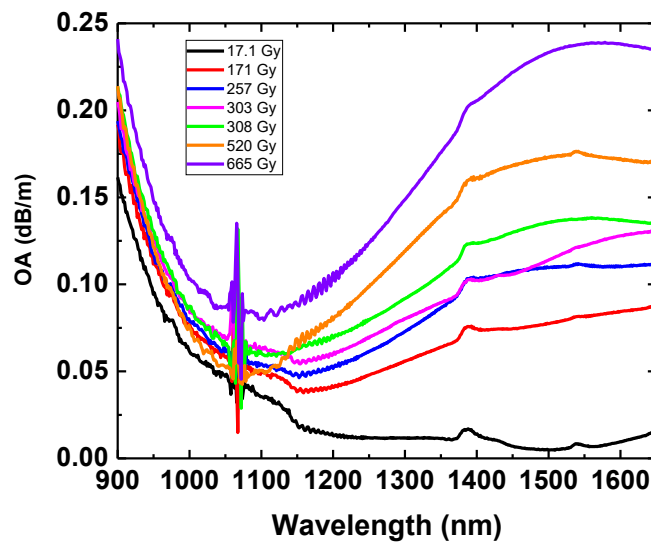


Figure 4.4 RIA spectra at different doses of the PCE-doped sample which was irradiated in CHARM.

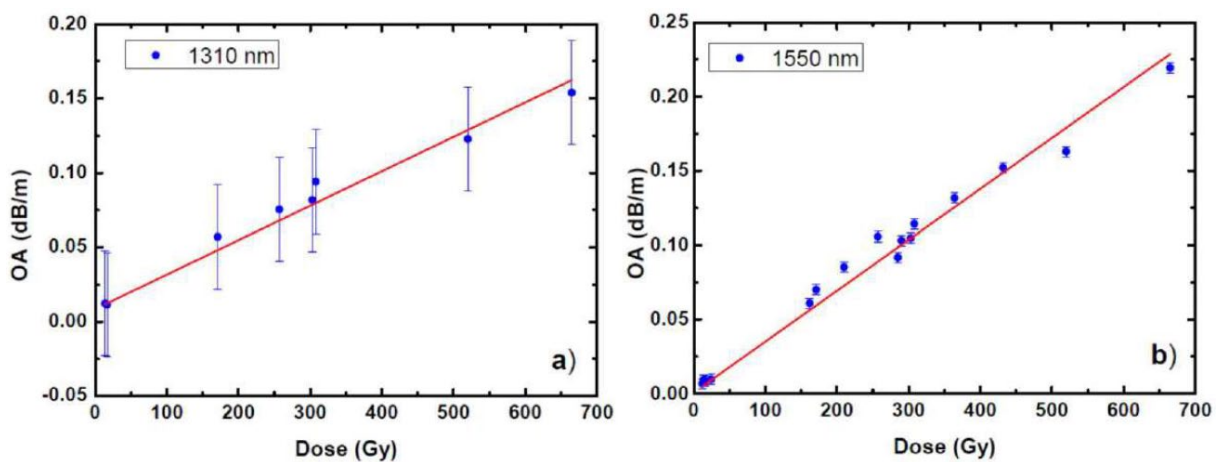


Figure 4.5 RIA values after the irradiation in CHARM for the PCE-doped sample at 1310 nm in a), at 1550 nm in b) and the respectively linear fit.

The sensibility values for the P-Ce-doped OF were obtained after a three months delay from the irradiation and then these values are an underestimation because of the spontaneous recovery of this fiber that becomes immediately visible and measurable as soon as when the irradiation is stopped.

The results presented here, demonstrated the highest potential of the P-doped optical fibers for the CERN application, explaining that in-situ measurement with OTDR were limited to this class of optical fibers.

4.1.2 Experiment at the Proton Synchrotron Booster (PSB)

After providing a proof of the potentialities of the DOFRS in a mixed-field radiation environment [81], an operational prototype was finally deployed in the proton synchrotron booster (PSB) during the last end-of-the-year technical stop (EYETS 2016/2017). The DOFRS prototype, exploiting at that time a multimode phosphosilicate optical fiber operated at 850 nm and identified by Dr. Iacopo Toccafondo [81], has been acquiring data in the real-case scenario of PSB since the beginning of the recommissioning. Unfortunately, this fibre suffered by non-negligible recovery which led to systematic errors in the measurement of the dose in the PSB in 2017. The obtained results have been published first in [82] and in [83].

D. Di Francesca, I. Toccafondo G. Li Vecchi et al., “Distributed Optical Fiber Radiation Sensing in the Proton Synchrotron Booster at CERN”, IEEE Trans. Nucl. Sci., vol. 65, no. 8, pp. 1639–1644, Aug. 2018, doi: 10.1109/TNS.2018.2818760. **(ANNEX 3)**

G. Li Vecchi, M. Brugger, S. Danzeca, D. Di Francesca, et al. , “Distributed Optical Fiber Radiation Sensing at CERN”, Proceedings of the 9th Int. Particle Accelerator Conf., IPAC2018, Vancouver, BC, Canada, 2018, doi: 10.18429/jacow-ipac2018-wepaf083. **(ANNEX 4)**

To highlight the main results, Figure 4.6 compares the dose distribution, calculated from the RIA measured by OTDR, along the OF sensor about 250 days from the beginning of data acquisition at PSB. The estimated dose is directly compared to the dose values provided by the

passive point dosimeters installed at different locations along the same fiber. As it can be seen, the different radiation monitor technologies provide the same values for the deposited dose.

Furthermore, as the DOFRS allows in situ measurements during the PSB operation, it is possible to draw the time map of the deposited dose along the sensitive optical fiber. Such a map is illustrated in Figure 4.7 that illustrates the evolution of the dose within the PSB during the 250 days of operation.

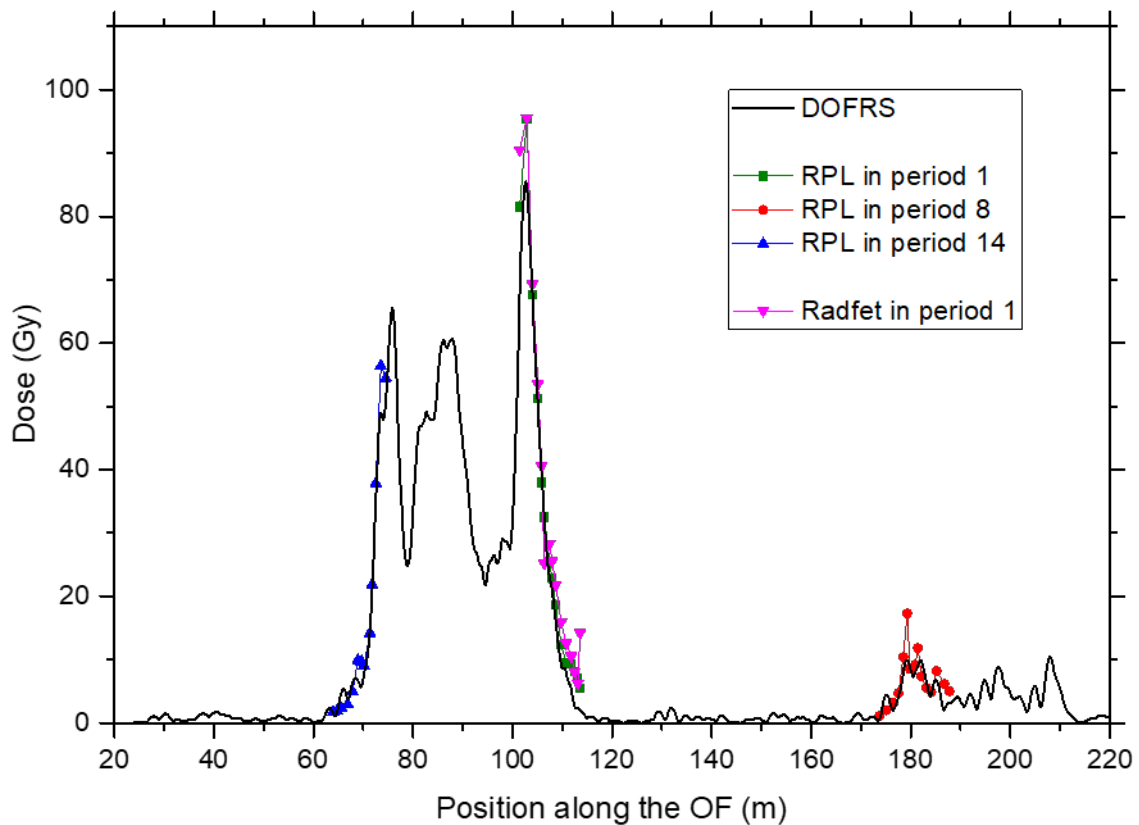


Figure 4.6 Comparison between the cumulated radiation doses measured by the DOFRS in PSB at the end of 2017, and the passive dosimeters installed at the OF cable location [83]. It should be noted that the multimode P-doped fibre had a non-negligible recovery that leads to a 30% error in the measurement. The trace has been rescaled considering this effect in the fiber calibration.

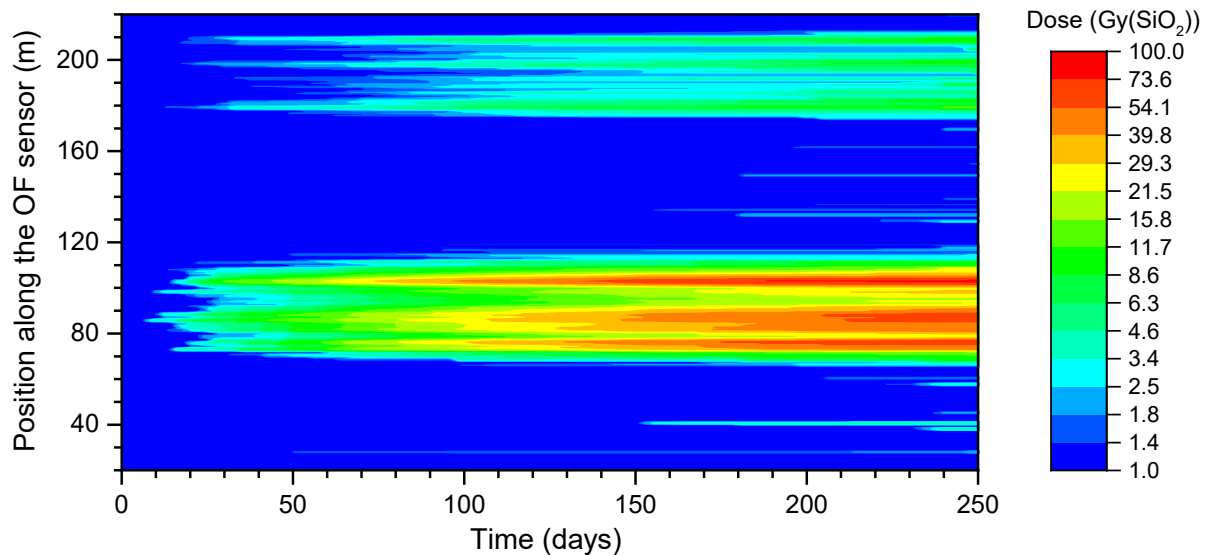


Figure 4.7 Spatial/temporal color map of radiation dose levels in the PSB during 2017 [83].

Beside the online and distributed measurement capabilities, the implementation of the DOFRS in large facilities such as CERN's accelerators offers some other practical advantages. 1) All the needed electronics are located in a remote/non-hazardous location, which allows intervention at any time. 2) After the initial installation of the cable duct and microducts, the cable-blowing technique allows replacement of a depleted cable directly from the rack location. No other access to the radiation environment is needed. 3) The information on the deposited radiation dose is safely stored on the OF sensor itself. An interruption of data acquisition would not cause information loss of the total accumulated dose. 4) A single cable can contain different radiation sensitive OFs, with the possibility to measure both low and high dose levels.

After the first implementation of the DOFRS in the PSB, the deployment in the PS (during YETS 2017/2018), SPS and part of LHC (during the Long Shutdown 2) has been achieved in by 2020. The experimental radiation profiles measured with the OF sensor could be coupled with 3-D FLUKA simulation to improve the estimates of dose also in those critical locations of the machines where the radiation cannot be probed experimentally.

4.2 Experiments at TRIUMF Facilities

4.2.1 Experiment at PIF facility: 480 MeV protons

In addition to the ^{60}Co γ -ray and X-ray irradiation tests that were carried out at CERN and UJM, additional proton irradiation experiments were carried out at the PIF facility of TRIUMF in Vancouver, Canada. The proton energy was set to 480 MeV and total irradiation time was ~ 58 minutes. During the irradiation run, a total fluence of $1.2 \times 10^{11} \text{ p}\cdot\text{cm}^{-2}$ was attained, and a corresponding total dose of 45 Gy(Si) was deposited in the sample, with an associated uncertainty of 5% (although the facility is equipped to provide the dose in silicon, at such energy the difference between Gy(Si) and Gy(SiO_2) is negligible). In the case of the proton irradiation, the experiment was carried out at room temperature using the classical RIA experimental setup described above. We used a halogen lamp as light source (DH2000 from Ocean Optics) and a NIR spectrometer (NIRQUEST from Ocean Optics) for the spectral measurement.

Figure 4.8 reports the result of the RIA tests carried out under 480 MeV proton irradiation. A ~ 10 m long OF spool (6 cm in diameter) was exposed to the constant and homogeneous proton beam. The irradiation was done with a dose rate of 12.9 mGy(SiO_2)/s (5% associated uncertainty), slightly higher than the ones investigated under ^{60}Co γ -ray. As we can see, the 1550 nm RIA growth kinetics is compatible with the one recorded under γ -rays. More precisely, under proton irradiation the fiber showed a linear response with a sensitivity of $4.1 \text{ dB}\cdot\text{km}^{-1}\cdot\text{Gy}^{-1}(\text{SiO}_2)$.

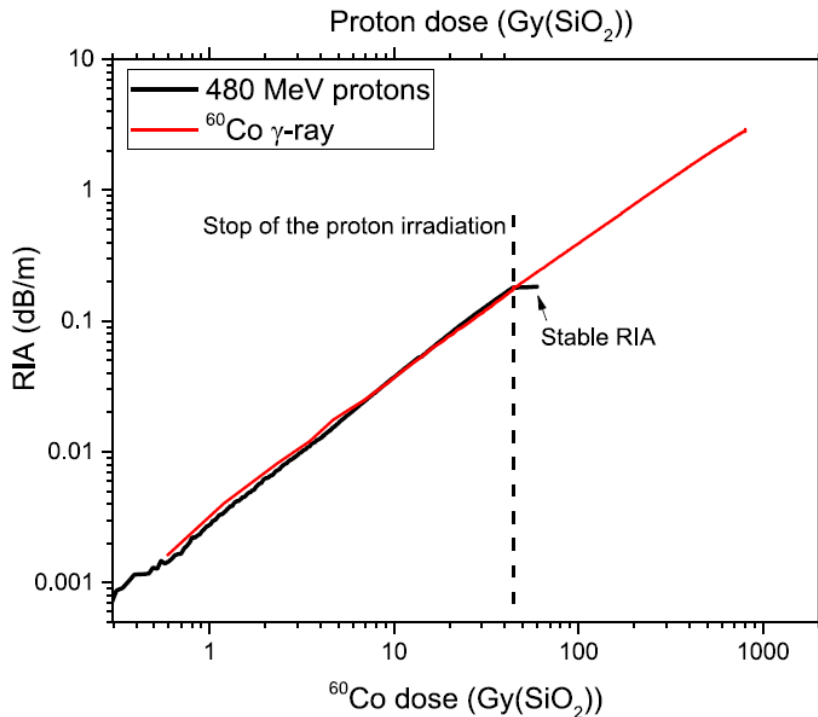


Figure 4.8 Comparison of the 1550 nm RIA growth kinetics under 480 MeV proton irradiation and ^{60}Co γ -ray. In both cases, the irradiation was performed at room temperature [91].

4.2.2 Experiment at TNF facility: atmospheric neutrons

The results presented in this work have been published in [120]: S. Girard, A. Morana, C. Hoehr, M. Trinczek, J. Vidalot, P. Paillet, C. Bélanger-Champagne, J. Mekki, N. Balcon, G. Li Vecchi, et al., “*Atmospheric Neutron Monitoring Through Optical Fiber-Based Sensing*”, *Sensors*, 20, 4510, 2020 <https://doi.org/10.3390/s20164510>. (ANNEX 5)

The RIA evolution at 1625 nm of the P-doped SMOF has been measured with an embedded OTDR (e-ODTR) from Viavi Solutions at TRIUMF Neutron Facility (TNF) facility in Vancouver [118]. At this facility a 480 MeV proton beam is employed for experiments in the high-intensity beam line BL1A. After traversing several experiments, the protons are stopped in a beam dump on an aluminum plate absorber surrounded by a water moderator. Neutrons are produced from spallation reactions and are subsequently channelled through the shielding

surrounding the TNF [118]. The resulting neutron spectrum, is close to the JEDEC standard JESD89A of terrestrial cosmic rays [119].

The experiments were performed in 2019, the 18 m long P-doped fiber under test was exposed to a neutron flux of $3.35 \times 10^6 \text{ n cm}^{-2} \text{ s}^{-1}$. The detailed results are available in [120].

The induced losses at 1625 nm evolve linearly with the deposited fluence (integrated between 10 and 400 MeV by the TRIUMF monitor count). This RIA growth is illustrated in Figure 4.19. Looking at the inset of this figure, we estimate that using this length of P-doped SMOF, it is possible to detect fluences above 10^9 n cm^{-2} with this e-OTDR (it should be hereby considered that some of the beam-flux fluctuations shown in the inset of Figure 4.9 occurred during the first hours of our tests, and were due to beam instabilities during the 520 MeV cyclotron operations). These results confirm the potential of a radiosensitive fiber to monitor the dose deposited by neutron integrated fluence in real time, even in complex environments with wide neutron-energy spectra as in the case of atmospheric neutrons.

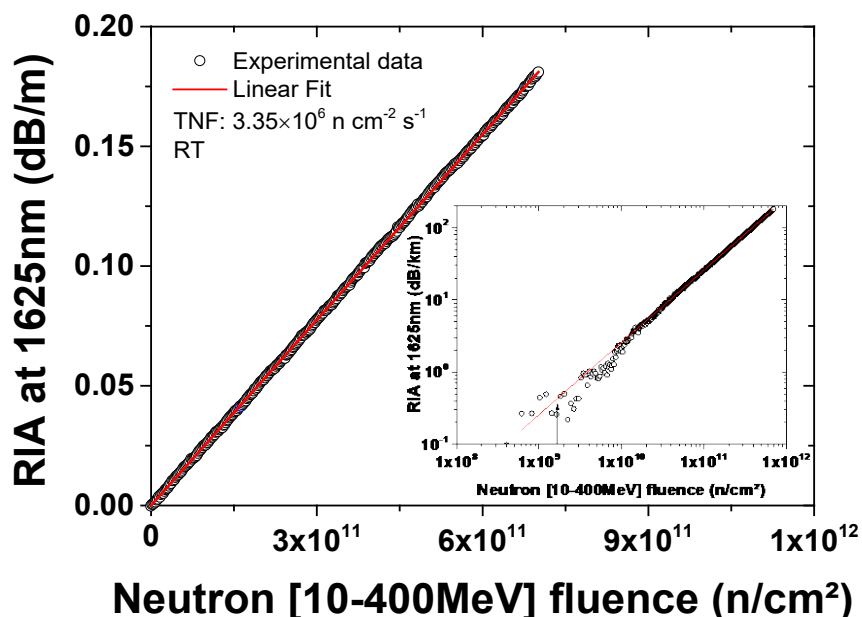


Figure 4.9 RIA growth at 1625 nm in an 18 m long coil of the P-doped fiber exposed to the TNF neutron [10-400 MeV] at room temperature (RT). In the inset are the same results illustrated in a log-log scale.

Several previous studies have shown that the main process leading to the generation of point defects in silica-based optical fibers is ionization, whereas displacement damage only marginally contributes to the generation of point defects, except at very high neutron fluences ($>10^{16}$ n cm⁻²) [6,121,122]. In the case of P-doped fibers, we showed in the previous paragraphs that the infrared optical losses are similar for equivalent doses (usually calculated with Geant4 or FLUKA Monte-Carlo packages) of X-rays, γ -rays, protons or the complex mixed environments of the CHARM facility [80]. It is then possible to measure the ionizing dose with the optical fiber regardless of the complexity of the considered environments in terms of a particle's nature. For this experiment and thanks to the FLUKA simulation of the TNF facility, we can determine the 1625 nm RIA dependence versus the equivalent dose deposited by the atmospheric neutrons and verify the ability of the fiber to act as a dosimeter in the TNF facility. It should be noted that the neutron capacity to ionize silica is only indirect, i.e., via the creation of secondary particles through nuclear reactions. These secondary particles interact with the atomic electrons and ionize them [123]. The RIA dose dependence is illustrated in Figure 4.10. and compared to the one measured at the same wavelength under X-rays (at a dose rate of 15.5 Gy/h, average photon energy of 40 keV) from the MOPERIX facility of the LabHC, France. For the neutron tests, we found a radiation sensitivity coefficient at 1625 nm of ~ 3.36 dB km⁻¹ Gy⁻¹ for this fiber very close to the coefficient obtained at the same wavelength under X-rays: 3.80 dB km⁻¹ Gy⁻¹. The small difference between those coefficients cannot be discussed as it remains within our experimental and theoretical uncertainties. This demonstrates the ability of the fiber sensor to monitor the equivalent dose associated with the atmospheric neutrons.

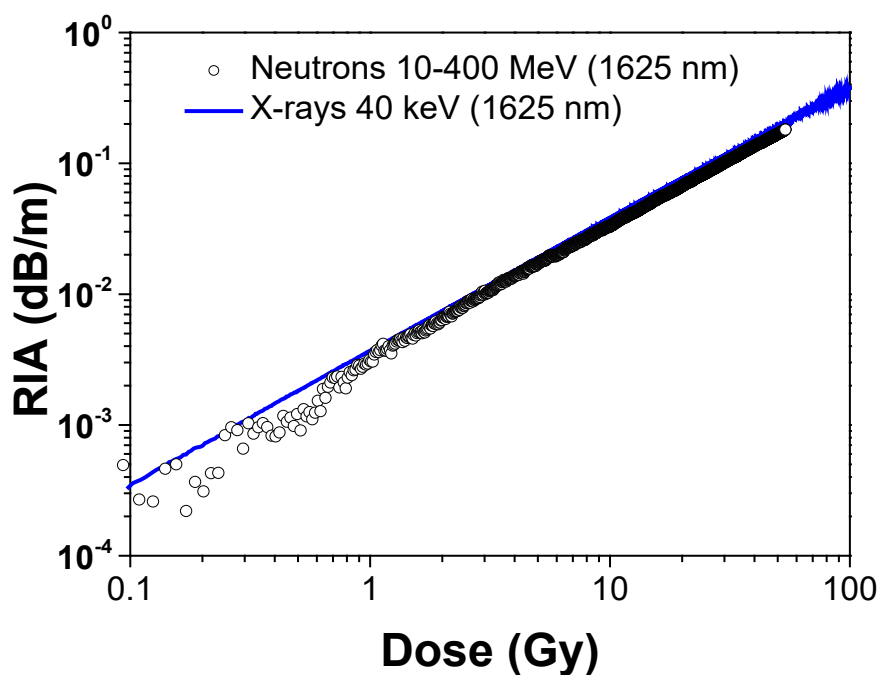


Figure 4.10 Comparison between the dose dependence of the RIA induced at 1625 nm by 40 keV X rays and atmospheric neutrons in a phosphorus-doped single-mode optical fiber.

Summary: We report mixed-field results for our P-doped OF dosimeter and their comparison with the RPL data. Post-mortem data acquired at CHARM are also reported. The results confirm the potential of the P-doped OF as a point and distributed dosimeter even in a mixed radiation field. The measurements carried out in Canada confirm a further potential application of our dosimeter in protons or atmospheric neutrons rich environments for different kinds of applications.

5 Chapter V. Towards Optimized P-doped Optical Fiber Dosimetry

We could imagine to improve even more the performances of the distributed fiber dosimeters exploiting the RIA monitoring of phosphosilicate single-mode optical fibers. In this chapter, we investigated three possible ways to improve our sensor:

- First, we studied how the IR light guidance properties influence the radiation response of the P-doped SMOF. A better understanding of the impact of the light modal distribution at 1550 nm could improve our understanding of the cladding contribution to the global fiber radiation response. This work has been published in [46].
- Second, we evaluate the potential of two post-irradiation treatments of the P-doped SMOF to reset the dosimeter, by bleaching the IR-RIA around 1.55 μm and related to P1 defects. Indeed, one of the last challenges, especially for distributed measurements, concerns the lifetime of the dosimeter. When the RIA approaches the sensor optical budget, the measurements become strongly degraded. For distributed measurements, it becomes eventually no longer possible to probe the full sensor length. Today's best solution is to replace the irradiated OF sensors with new ones, as it is currently done at CERN. Although this is a relatively simple and fast operation thanks to modern cable jetting, the production of new cables and replacement operations require careful long-term planning and are associated with non-negligible costs. Furthermore, a partial calibration is required for each new OF. To be of practical interest, we should also ensure that after this resetting treatment, the dosimeter keeps the same calibration for future irradiations. We discussed here the performances of two different fiber treatments:
 - First, we discuss the potential of a hydrogen-loading of the irradiated fibers to reset the dosimeters. This treatment was selected as it is today well known that hydrogen

is able to easily migrate to the fiber core and is able to passivate most of the radiation-induced defects. This work has been published in [115] and is based on preliminary studies conducted during my master's thesis [109].

- Second, we investigated the potential of photobleaching (PB) procedure in the visible – near IR domain to bleach the RIA around 1550 nm and to reset the dosimeter. This work is detailed in [124].
- Third, we performed a preliminary investigation of the potential of changing the OTDR interrogator for an OBR4600 from Luna Technologies. In this OFDR, better resolution can be achieved along the radiation sensitive length but as the measurement principle is clearly different, the RIA measurements are less direct than in the case of OTDR.

5.1 . Role of the guiding properties

The results presented in this work have been published in [46]: G. Li Vecchi et al., “Infrared radiation Induced attenuation of radiation sensitive optical fibers: influence of temperature and modal propagation”, *Opt. Fib. Tech.*, vol. 55, p. 102166, Mar. 2020, doi: 10.1016/j.yofte.2020.102166. **(ANNEX 6)**

In a SMOFs only the fundamental mode (noted as LP_{01}) is guided for wavelengths above the cutoff one. Most of the LP_{01} mode power remains confined in the core but an evanescent part of the wave is travelling in the fiber cladding. The Confinement Factor (CF) is wavelength dependent, increasing at decreasing wavelengths in the single-mode regime. The LP_{01} spatial distribution explains that the RIA strongly depends on the cladding co-dopants even for identical core materials [17,89,90]. For our radiation sensitive OFs, the dopants (P, Al) are incorporated only in the core whereas the cladding is made of more radiation tolerant pure silica, (see [33] for more detailed comparison). Therefore, during the irradiation most of the point defects causing the RIA will be located in the core. The different radiation responses of the core and cladding materials imply that the absorption bands associated with point defects can be

modulated in SMOFs with respect to the case of a homogeneous bulk sample. The main purpose of this paragraph is to evaluate the influence of modal propagation on the RIA spectra [17].

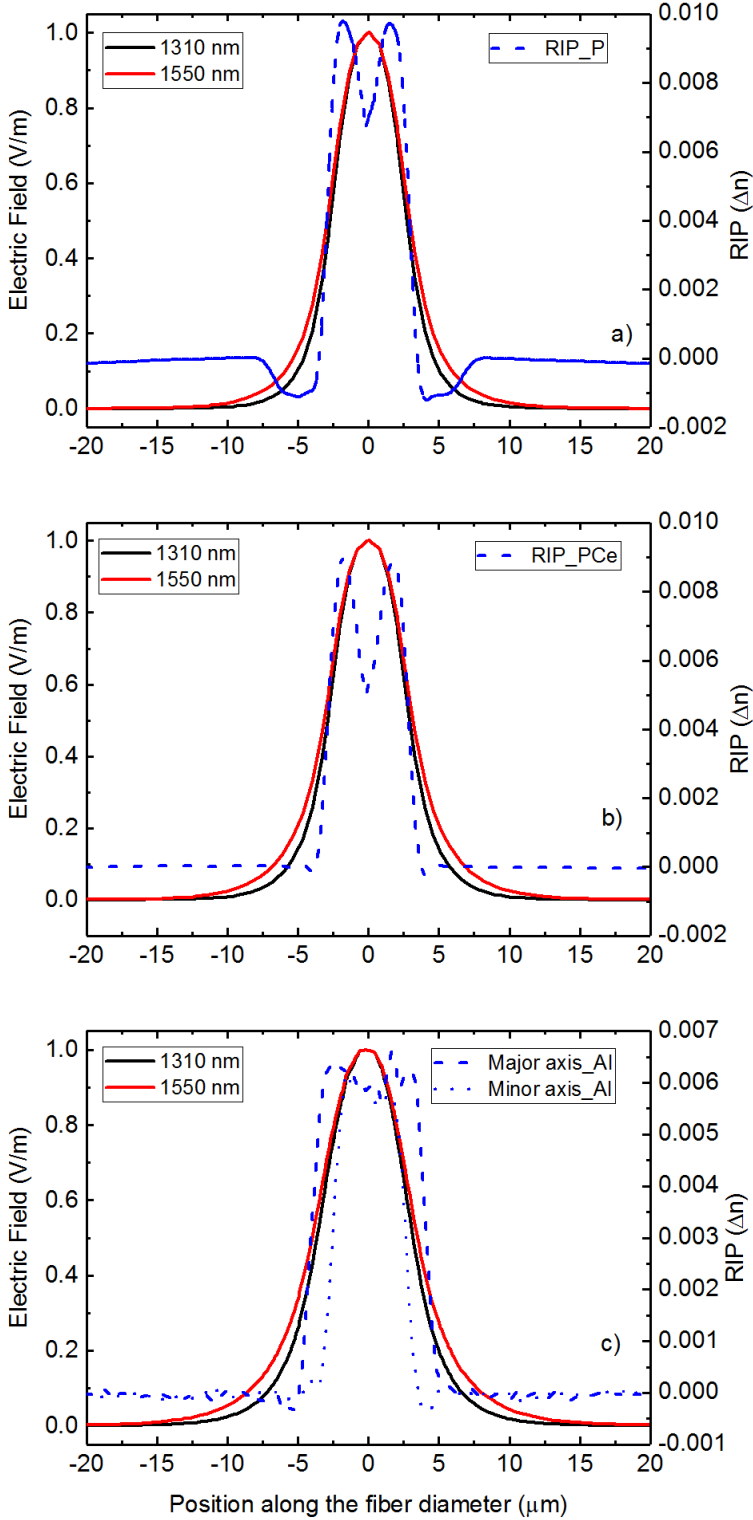


Figure 5.1 Refractive index profiles of the three SMOFs as a function of position along the fiber diameter (center of the OF at zero) and normalized fundamental modes at 1310 and 1550 nm. a), b) and c) refer to P, PCe and Al-doped OFs, respectively [46].

To characterize the guided mode(s) we solved the following optical propagation equation [14]:

$$\nabla_t^2 E_{(x,y)} + (2\pi / \lambda)^2 (n_{(x,y)}^2 - n_{eff}^2) E_{(x,y)} = 0$$

where ∇_t^2 is the transverse Laplacian operator, $E_{(x,y)}$ is the spatial distribution of the electric field, $n_{(x,y)}$ is the Refractive Index Profile (RIP), n_{eff} the effective index of the optical mode, and λ the wavelength. Based on these RIP measurements, the properties of the propagating mode(s) have been calculated with COMSOL Multiphysics for wavelengths ranging from 1100 nm to 2200 nm with a step of 20 nm. The spatial distributions of the normalized fundamental mode LP_{01} are illustrated in Figure 5.1 for the three OFs and compared to their RIPs. As it can be seen, the optical mode LP_{01} is more confined in the core at shorter wavelengths, meaning that the relative contribution to the RIA of the point defects located in the cladding increases at larger wavelengths. Regarding Figure 5.1 a) and b) we can see how the RIP profiles for the P and P_{Ce}-doped fibers are similar. These RIP are characterized by a higher value in the core than the cladding (mandatory to achieve the light guidance) with a depression at the center of the fiber core that is known to occur during the collapsing phase of the preform fabrication. Other fabrication parameters such as P concentration, drawing parameters, coating types are similar for the two fibers. In this case, we could assume that the difference in their radiation responses will be only related to a chemical difference. The double RIP we can see for the Al-doped OF in Figure 5.1 c) is due to the particular geometry of this fiber core that is slightly elliptical and therefore presents two axes of symmetry. For this reason, the RIP of the Al-doped fiber are given for both the major and minor axis of the core geometry. The elliptical shape of the core is due to the production process. For this fiber, an approximated fundamental mode has been considered, using an average core radius of 4.3 μm .

5.1.1 Spectral study of the RIA in the selected OFs (NIR)

For the interpretation of the spectral results, we will only consider wavelengths longer than the cut-off one. Therefore, assuming that the RT spectrum of the Al-doped OF is affected by a problem occurred during the acquisition of the measurements, we can see that the spectra at 35 °C and 50 °C follow the same trend (red and blue dashed lines). Faustov et al. have seen a reduction of ~25% of the 1.55 μm RIA saturation level at 80 °C compared to the one measured at 30 °C in Al-doped fibers irradiated at 73 kGy. However, at lower doses, the positive effect of the temperature on the induced losses seems much more limited [47], in agreement with our results. The application of the CF to the spectra acquired at RT temperature remarkably modifies the RIA spectra, inducing an apparent “blue-shift” of the maximum of attenuation for the P-doped sample. It is important to underline the fact that we have applied a smoothing to the spectra of P- doped sample shown in Figure 5.2, to better highlight the peak displacement due to the guiding properties. We show the result obtained for the PCe-doped OF in Figure 5.3. As for the P-doped fiber, we detect an apparent “blue-shift” of the maximum of ~45 nm when we consider the CF. This is consistent with the fact that the two fibers have a similar RIP and with the hypothesis that the distribution of defects in the core is homogeneous. For the PCe sample, thanks to a more appropriate choice of sample length, it is possible to extend the spectra up to 1900 nm and see how seems to appear another IR spectral component, in addition to the P1 band. The application of CF for the Al-doped OF at the spectra acquired at RT is not easy to interpret, because of the source fluctuation previously mentioned. What we can see, however, is a substantial match between the 35 °C and 50 °C spectra reported in Figure 5.4.

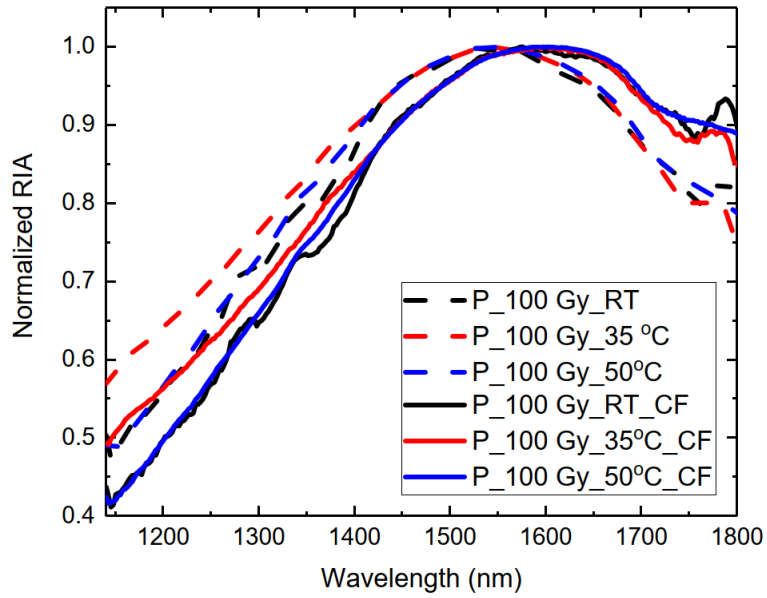


Figure 5.2 Normalized RIA spectra of P-doped OF at 100 Gy before (dash line) and after (solid line) CF correction [46].

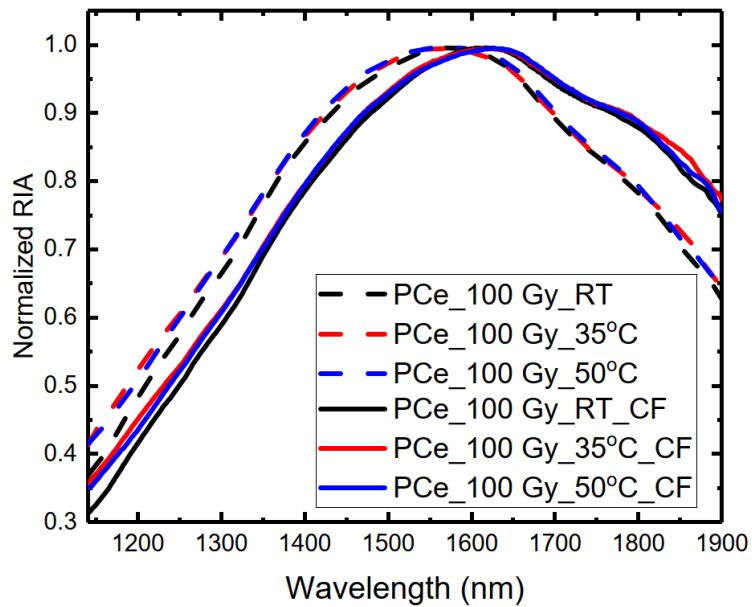


Figure 5.3 Normalized RIA spectra of PCe-doped OF at 100 Gy before (dash line) and after (solid line) CF correction [46].

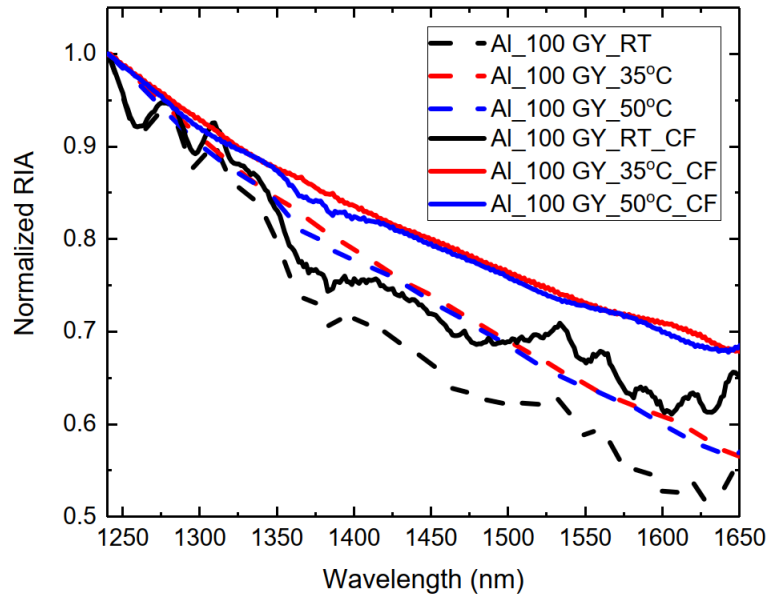


Figure 5.4 Normalized RIA spectra of Al-doped OF at 100 Gy before (dash line) and after (solid line) CF correction [46].

The simulation of the guiding properties of the fiber has highlighted a “blue-shift” of about 45 nm at the maximum of the absorption spectra for the P and PCE-doped fiber. We obtained a good agreement for the P1 band on the fibers doped with P irradiated to RT by applying the CF and the value reported in the literature.

Concerning the Al-doped fiber investigated, the CF application highlighted a relative increase of the absorption with the wavelength, however preserving the monotonic trend of the RIA spectrum.

Summary: We investigated how the light guiding properties of the tested single mode optical fibers affects the optical absorption bands related to P-, PCE and Al-related defects absorbing in the infrared domains. By considering the confinement factor and making the hypothesis that the RIA is mainly caused by the absorption bands of point defects located in the fiber core, we could reconstruct the optical absorption band than we could observe in a bulk homogeneous sample of the same composition than the core. In the future, to optimize the dosimetry properties of fibers, considering their guiding properties could be an asset.

5.2 Regeneration of the dosimeter through H₂

Building on the work done during my master's thesis [109] and subsequently published in [115], in this paragraph we present the online spectral analysis of the RIA for the single-mode P-doped and P_{Ce}-doped OFs in the infrared domain, and in particular, at 1550 nm. In the following, we also explore the feasibility of regenerating the OF properties via an H₂ treatment at room temperature. The interest of such study was twofold: investigating the possibility of producing hole-assisted OFs, which allow on-site regeneration of the OF only by accessing one end, as we have previously shown in [30] and investigating the possibility of resetting the OF sensor for a second irradiation run. For the latter reason, we also report, in the following sections, on the RIA of irradiated and subsequently H₂-recovered OFs.

The RIA experiments were performed by irradiating the fiber samples up to doses of 100 kGy(SiO₂) with the X-ray MOPERIX machine whose set-up is described in Chapter 2.3.3. During the irradiation run, the temperature was ranging between 23 °C and 27 °C and the dose rate was fixed at 10.7 Gy(SiO₂)/s. This dose rate allowed us performing the experiments in a relatively short time frame and to compare the RIAs of the different samples up to 100 kGy. The transmitted spectrum is recorded every few seconds while a small spool (6 cm in diameter) of ~0.3 m length of the OF under study is homogeneously irradiated. The RIA spectrum can then be calculated by comparing the transmission spectrum before the irradiation with the ones associated with a certain accumulated dose. The light power injected into the OF was kept as low as possible (about 1 μW level on the whole spectrum) in order to prevent photobleaching processes [125]. We carried out the H₂ treatments by placing the fiber under test in a Parr reactor and filling it up with 150 bar of H₂ at room temperature. The diffusion process inside the OF takes place transversally along the fiber cross section, as described in Chapter 2.4.4. Special custom-made connectors allowed the extremities of the OF to be externally accessible. It was then possible to monitor the evolution of the optical attenuation. Based on preliminary

investigation [109], the duration of the H₂ loading was set to the minimum necessary to permeate the OF cross section (no saturation was reached) and recover all the radiation-induced losses. Before the second irradiation, the H₂-recovered sample was left for 25 days at room temperature in air atmosphere to let the excess interstitial H₂ desorb. The dopants concentration profiles of the two studied OF samples were measured via energy-dispersive X-ray spectroscopy and are shown in Figure 5.5.

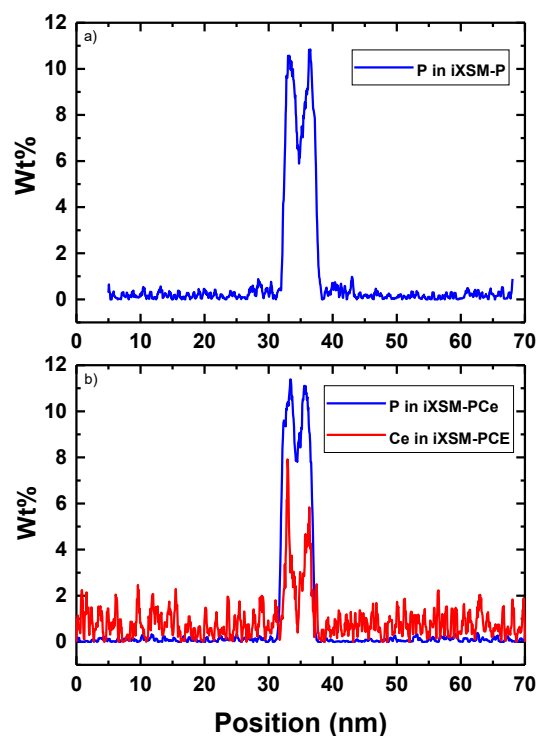


Figure 5.5 Dopant concentration profiles in the two studied samples. a) iXSM-P. b) iXSM-PCe.

The sample names with the corresponding dopants and average concentrations in core and cladding zones was reported in Table 2-1.

The study of our two fibers starts by analyzing the radiation response of the pristine fibers. In Figure 5.6, we report the growth kinetic curves during and post the irradiation. It is immediately

visible that the iXSM-P OF is the more radiation sensitive between the two. Both radiation responses are nonlinear with the dose. The radiation sensitivity at low radiation doses is the highest and decreases gradually with increasing dose. The iXSM-P has got a mean radiation sensitivity of about $0.28 \text{ dB km}^{-1} \text{ Gy}^{-1}$ over 100 kGy, whereas for the iXSM-PCe it is about $0.1 \text{ dB km}^{-1} \text{ Gy}^{-1}$. Obviously, the monotonicity of the RIA curves (no saturation is reached in the studied dose range) is a desirable feature for the retrieving of correct dose measurements. Finally, a remarkable difference between the iXSM-P and iXSM-PCe is that the first OF presents a negligible post-irradiation increase of the RIA, whereas the second one shows a noticeable recovery process. The latter phenomenon is usually present in OFs whose radiation response is also dose-rate dependent.

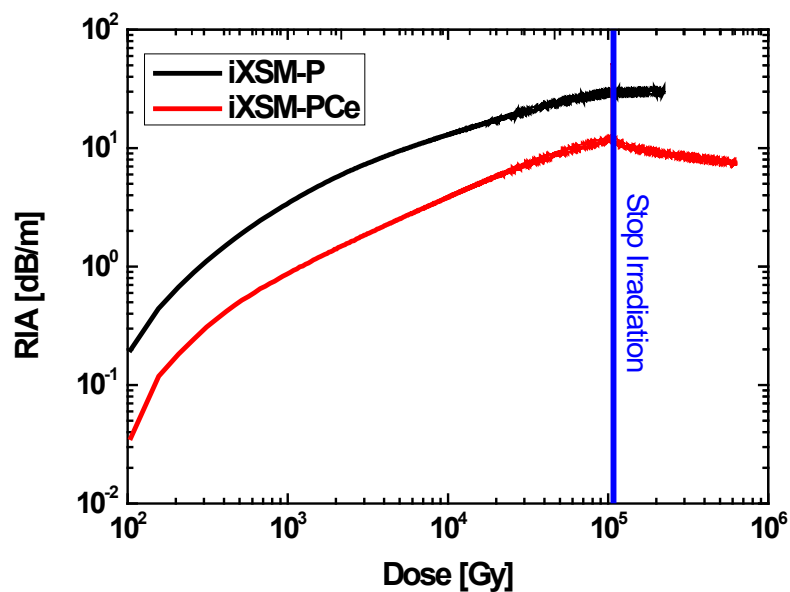


Figure 5.6 1550 nm RIA growth kinetics as a function of the dose for the two investigated OF samples; adapted from [115].

Figure 5.7 shows the spectra acquired at different times from the beginning of the H_2 loading of the iXSM-P irradiated fiber. The first effects are observed about 15 hours after the start of hydrogenation and lasts about 7 hours. This latter time reasonably agrees with the core size (3

μm radius) and the expected time to cover this length from diffusion coefficient of molecular hydrogen in silica at RT ($3.78 \times 10^{-11} \text{ cm}^2 \text{ s}^{-1}$) as reported in the literature [126]. In the spectra, we find a signal recovery around 1600 nm and the appearance of a feature at about 1876 nm. In the literature we find that at about 1876 nm an absorption band is associated to H_2 so enabling us to attribute the found feature to the presence of this latter molecule in the core of the fiber [127]. The recovery effect rises with increasing the hydrogen exposure time as well as the band amplitude at about 1876 nm. As we can see from the same figure, we can distinguish two phases during H_2 loading. In the first phase (Figure 5.7 on the left), the hydrogen interacts with P1 defects and removes them, bleaching the 1600 nm band; in the second phase (Figure 5.7 on the right) the band around 1870 nm keeps on growing. As already pointed out in Figure 5.7 after about 22 hours, 97% of P1 defects have been destroyed and the light at the 1550 nm wavelength is not affected by the increasing amount of hydrogen penetrating the fiber core.

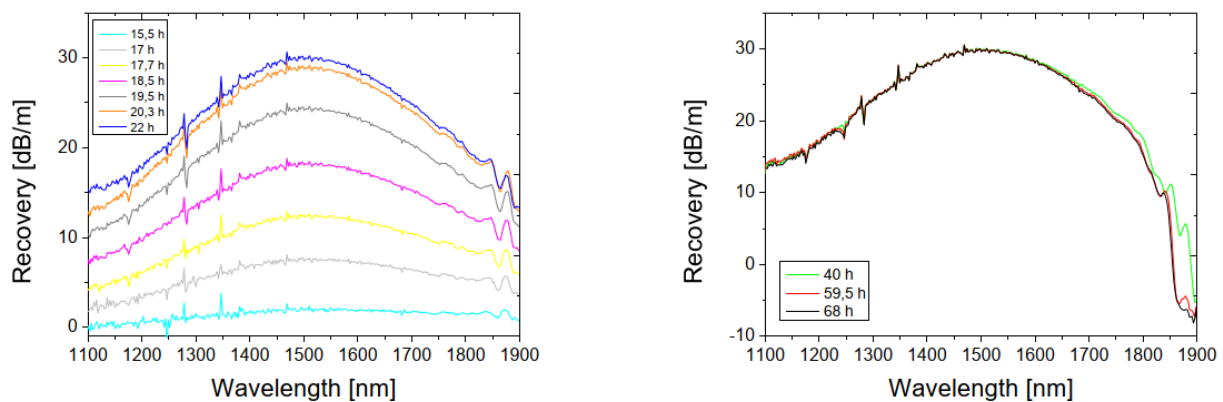


Figure 5.7 Spectra acquired during the H_2 loading of iXSM-P fiber previously irradiated at 100 kGy by X-rays. On the left we see the effects of H_2 loading up to 22 h on the RIA; on the right from 40 h up to 68 h [109].

Figure 5.8 reports the recovery spectra acquired during H_2 loading of the iXSM-PCe sample irradiated at 100 kGy. In the left figure, we note that we have a recovery in the range around 1600 nm, which we can attribute to the destruction of P1 defects, as for the iXSM-P sample. In the right figure, instead, we note the appearance of bands at 1245 nm, 1690 nm and 1867 nm

attributed to absorption of H₂. We note that the 1245 nm band could be first seen only in the difference spectra because the RIA component of P1 was much more intense.

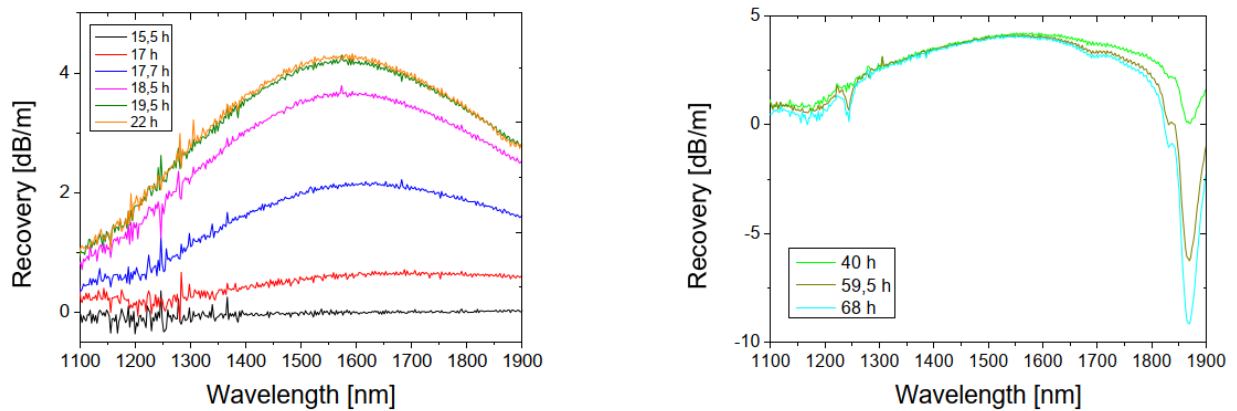


Figure 5.8 Spectra acquired during the H₂ loading of iXSM-PCe fiber previously irradiated at 100 kGy by X-rays. On the left we see the effects of loading up to 22 h; on the right by 40 h up to 68 h [109].

The H₂ bands start to become clearly noticeable after about 40 h of hydrogenation. Since one of the objectives of the present experimental investigation was to irradiate a second time the H₂-recovered samples without left-over H₂ dissolved into the silica matrix, the fibers were kept at room temperature in air for 25 days before carrying out the second irradiation.

In Figure 5.9, we show the second RIA spectra of the iXSM-P sample which was first irradiated up to 100 kGy and then recovered by H₂ diffusion and the RIA of the pristine irradiated sample. During the second irradiation, all experimental conditions were unchanged with respect to the first one in order to allow a meaningful comparison between the two responses. Similarly, in Figure 5.10 the RIA spectra comparison of the iXSM-PCe OF are displayed. In both Figure 5.9 and Figure 5.10, the RIA spectra are dominated by the presence of the P1 defect. However, after the H₂-recovery treatment, the radiation response of the two OFs is more complicated. This is quite evident by looking at the RIA growth kinetics at 1550 nm shown in Figure 5.11.

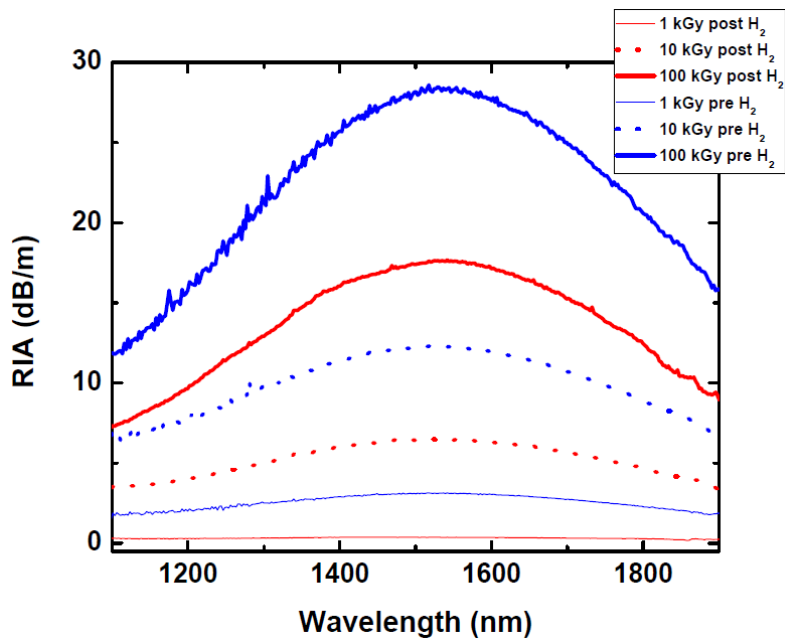


Figure 5.9 RIA comparison of iXSM-P-doped OF before and after H₂ loading.

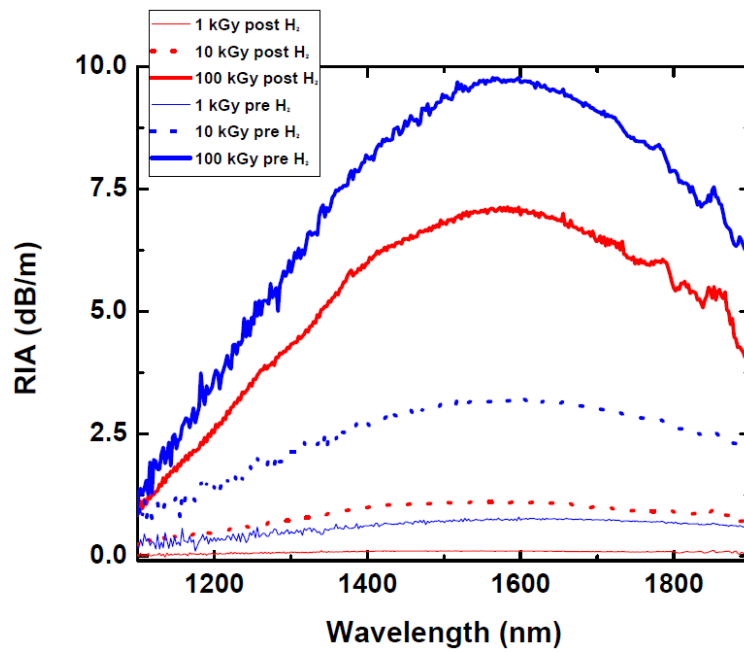


Figure 5.10 RIA comparison of iXSM-PCe-doped OF before and after H₂ loading.

Considering the double-logarithmic plot, both samples present a sublinear dependence on the dose at low and high radiation doses, with a transition range in which the radiation response is

superlinear. A part from the very different response of as-received and H₂-recovered samples, the radiation sensitivities are in general lower in the H₂-recovered ones. Moreover, similar to the data reported in Figure 5.6, after irradiation the H₂-recovered iXSM-PCe fiber shows a quite evident spontaneous recovery, which takes place at room temperature. The same phenomenon, which was not observed after the irradiation of the as-received iXSM-P sample, can be detected on the H₂-recovered iXSM-P. However, it should be pointed out that it is much weaker in the H₂-recovered iXSM-P fiber than iXSM-PCe.

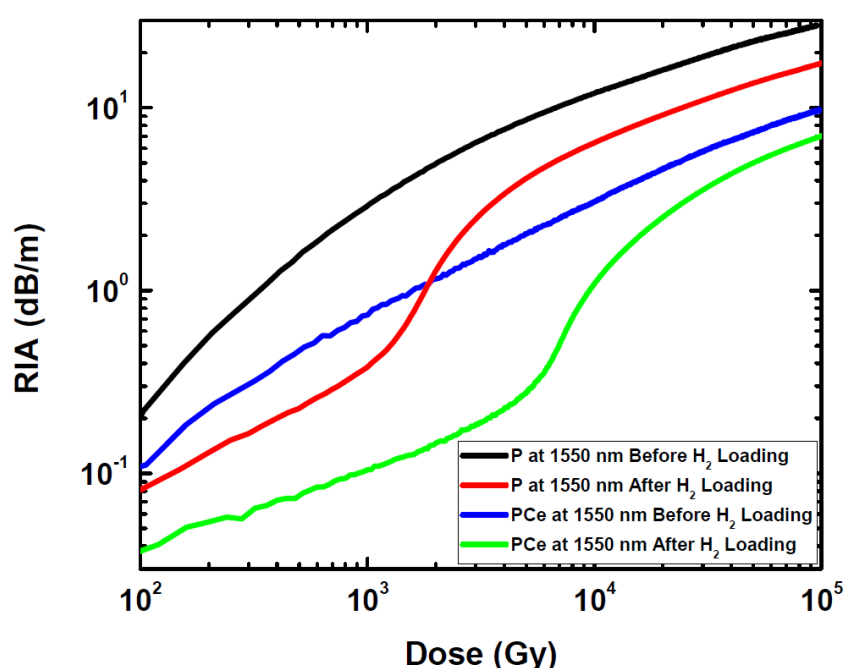


Figure 5.11 RIA growth kinetics comparison between iXSM-P and iXSM-PCe-doped OFs before and after H₂-loading.

The high pressure H₂ treatment at room temperature successfully recovered the losses induced by the first deposition of 100 kGy in the samples. This clearly implies that, at room temperature, interstitial H₂ molecules can react with the radiation-induced defects and directly or indirectly bleach all P1 defects. Some previous tests had shown that if the second irradiation is performed immediately after the H₂ treatment, without waiting a period for the desorption waiting for the outgassing to take place, the second irradiation leads to the creation of intense H-related

absorption peaks [30], [109], with a total change of the spectral radiation response in the infrared domain. In the present investigation, we decided to minimize the amount of H₂ diffused into the OFs in order to check if we still can observe a change in the radiation response. Therefore, after a 22-h-long treatment, we let the OFs desorb all excess interstitial H₂. During the second irradiation, P1 associated absorption band is, once again, the major contribution to the RIA in the near-infrared domain. Moreover, no H-related bands are detectable, which confirms the absence of significant amount of interstitial H₂ in the glass matrix. Although, from a spectral point of view, the response is quite similar to the one recorded during the first irradiation, the RIA growth kinetics and sensitivity changes remarkably. Such phenomenology might involve point defects other than P1 that were created during the first irradiation and that affect the generation rate of P1 at low doses during the second irradiation. These same defects might also have interacted with H₂ during the recovery treatment.

Summary: We have reported some experimental results concerning the radiation effects of two types of single-mode phosphosilicate OFs that differ for the presence of Ce codopant. Only the simply P-doped OF is of interest for dosimetry applications. We also investigated the potential of an H₂ loading treatment, at room temperature, to regenerate the irradiated OF samples. On one hand, the diffusion of molecular hydrogen in the glass matrix is able to bleach the radiation-induced losses. On the other hand, we showed that the same treatment cannot reset the fiber dosimeter to its initial state. The recovered fibers preserves some radiation detection capabilities, but the calibration curve of the pristine OFs cannot be used to determine the radiation dose in the following irradiation run.

5.3 . Regeneration of the dosimeter through photobleaching

The results presented in this work have been published in [124]: G. Li Vecchi et al., “In-situ regeneration of P-doped optical fiber dosimeter”, Opt. Lett., vol. 45, no. 18, p. 5201, Sep. 2020, doi: 10.1364/OL.402382.

In the previous chapters, we demonstrated the suitability of the selected P-doped SMF operated at 1550 nm to act as a point or distributed dosimeter. Indeed, using an OTDR it is possible to

measure the RIA evolution all along the OF sensor, and monitor online the radiation dose levels with one-meter spatial resolution. Commercial SM-OTDRs typically operate at 1310 nm, 1550 nm and 1625 nm. Around these wavelengths, silica-based SMFs usually have their minimum of intrinsic optical attenuation. In the same spectral domain, the P-doped OFs exhibit a well-known radiation-induced absorption band peaking very close to 1550 nm that is associated with the paramagnetic P1 point defect. Around RT, P1 is not affected by spontaneous recovery usually occurring after the irradiation, and shows no sign of Photo-Bleaching (PB) induced by the OTDR probing light at 1550 nm.

One of the last challenges, especially for distributed measurements, concerns the lifetime of the dosimeter. When the spatially integrated RIA approaches the OTDR optical budget, the measurements become strongly degraded, and eventually it is no longer possible to probe the full sensor length. As mentioned at the beginning of the Chapter, the best solution is to replace the irradiated OF sensors with new ones, as it is currently done at CERN. Although this is a relatively simple and fast operation thanks to modern cable jetting, the production of new cables and replacement operations require careful long-term planning and are associated with non-negligible costs. Furthermore, a partial calibration is required for each new OF. In this paragraph, we investigated the capability of the PB effect to ‘reset’ the dosimeter by achieving the IR-RIA recovery all along the irradiated length. As shown by several authors [128,129,130], injecting light into irradiated OFs can sometimes induce a remarkable RIA restauration. PB results from the release of trapped carriers forming point defects in the silica network or, alternatively, from the recombination of free carriers with more thermally stable defect states [67]. If the PB successfully bleaches the IR-RIA of our radiosensitive fiber, it is also crucial to check that the radiation sensitivity of the OF remains unchanged for the future dose measurements. This last point was the limiting factor of the previously studied H₂ loading technique described in Chapter 2.4.4. Indeed, H₂ treatment was able to bleach the IR-RIA but

the radiation response of the treated OF was affected and its initial calibration response modified. To evaluate the potential of PB, we followed a multistep approach. First, systematic PB tests on irradiated P-doped samples have been performed with fiber-pigtailed laser diodes emitting at different wavelengths and having quite large output powers. Second, more specific PB tests have been performed under excitation at 514 nm with cw Argon-ion laser on a 30 m long P-doped sample X-ray irradiated at 100 Gy(SiO₂). Finally, we re-irradiated the regenerated samples to investigate if their dosimetry properties are maintained after the reset procedure.

A sample of the P-doped SMF from iXblue was irradiated at RT with γ -rays in the ⁶⁰Co facility at CERN up to 1170 Gy(SiO₂) with a dose rate of 12 mGy/s. We also irradiated 30 m of P-doped OF at 0.1 Gy/s up to 100 Gy(SiO₂) with the MOPERIX X-ray machine. In this case, OTDR acquisitions at 1550 nm (*2ns pulse duration, 4cm sampling, 2 minutes of acquisition time*) were recorded during the irradiation run. The attenuation spectra of irradiated samples have been measured in the UV-VIS and NIR spectral region through the cutback technique. In Figure 5.12 a.), we report as example the UV-VIS RIA spectrum of a multi-mode (MM) P-doped OF irradiated up to 2 kGy (adapted from [131]) and in Figure 5.12 b) the IR-RIA spectrum of our P-doped SMF irradiated at 1170 Gy. The UV-VIS spectrum demonstrates the presence of several absorption bands that are associated with P-related point defects reported in the literature [34,130]. However, in the IR domain, the P1 defect, peaking at 0.79 (FWHM = 0.29) eV, is the main contributor [33,34,35].

Finally, it is worth to mention that these defects cannot be detected by OA measurements in the not-irradiated P-doped OF, whose attenuation spectrum is reported in the inset of Figure 5.13.

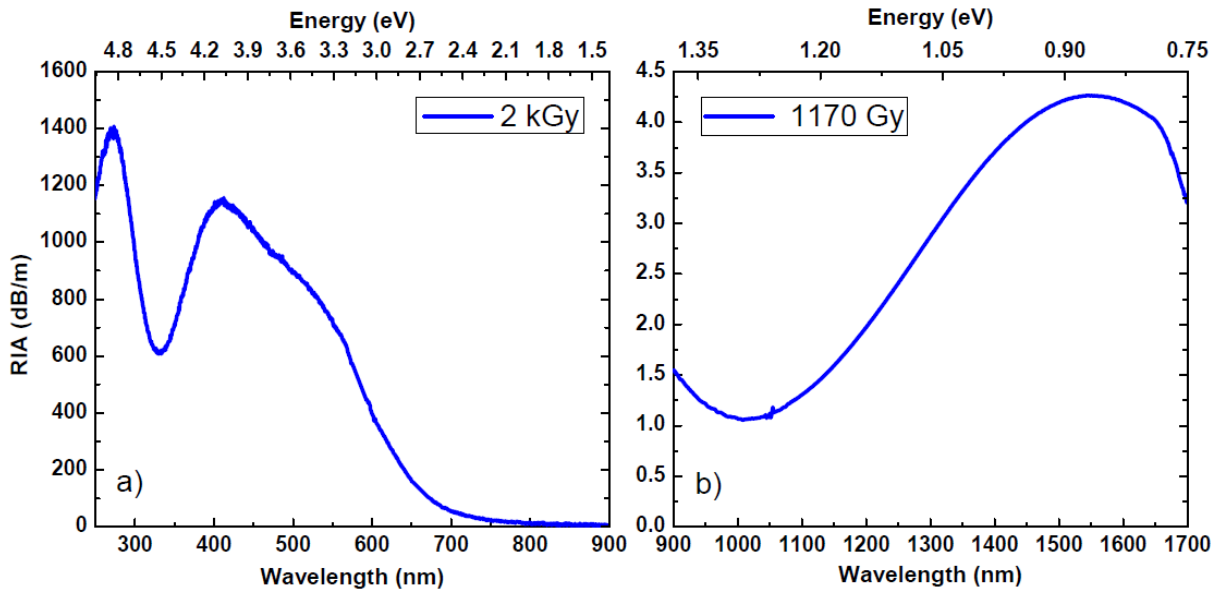


Figure 5.12 a) UV-VIS spectrum for a multi-mode (MM) P-doped OF irradiated at 2 kGy (adapted from [124]). b) IR-RIA spectrum of our P-doped SMOF sample irradiated at 1170 Gy.

We used the setup described in Chapter 2.4.3 to characterize the efficiency of several different laser sources in the visible and near-IR domains to bleach the RIA at 1550 nm in this fiber sample. As an example, Figure 2.14 illustrates the PB efficiency of a 514 nm Argon-ion laser line (430 mW) for different exposition times of the 1170 Gy irradiated sample. Such experiment has been repeated numerous times, varying the PB laser diode and estimating the percentage of RIA recovery for each configuration. The obtained results are summarized in Figure 5.13 that reports the recovery percentage of the RIA at 1550 nm of P-doped samples irradiated at 1170 Gy, as a function of the PB laser wavelength as well as the most important parameters of the employed laser sources. It should be noted that the given laser powers correspond to the light levels in the FUT. To investigate the PB efficiency at different wavelengths, a new irradiated sample is used at each time, all samples originate from the same uniformly irradiated OF. Our tests show that the 405.5 nm laser signal was the most efficient one for a one-hour treatment, even if its injected power was the lowest. The 514 nm laser light also gives good and

interesting results at relatively high power. The PB efficiency is strongly wavelength dependent, as already reported for some fiber typologies [128,129,132]: we observe a light transmission increase at 1550 nm (roughly 75%) with the laser at 405.5 nm, whereas using the laser at 912.6 nm we see a reverse effect with a slight increase of the IR losses. Subsequently, we carried out another experiment with a longer (30 m) sample that was X-ray irradiated at the lower accumulated dose of 100 Gy. Following the same experimental procedure, we injected the more powerful 514 nm light from a cw Argon-ion laser into the sample (430 mW), we did this alternately from both the FUT sides, firstly on one end and then on the other, to accelerate the PB process, and the results are reported in Figure 5.14. The black curve is the trace acquired before the beginning of the laser light injection, while the others are the OTDR traces recorded at different times during PB experiments.

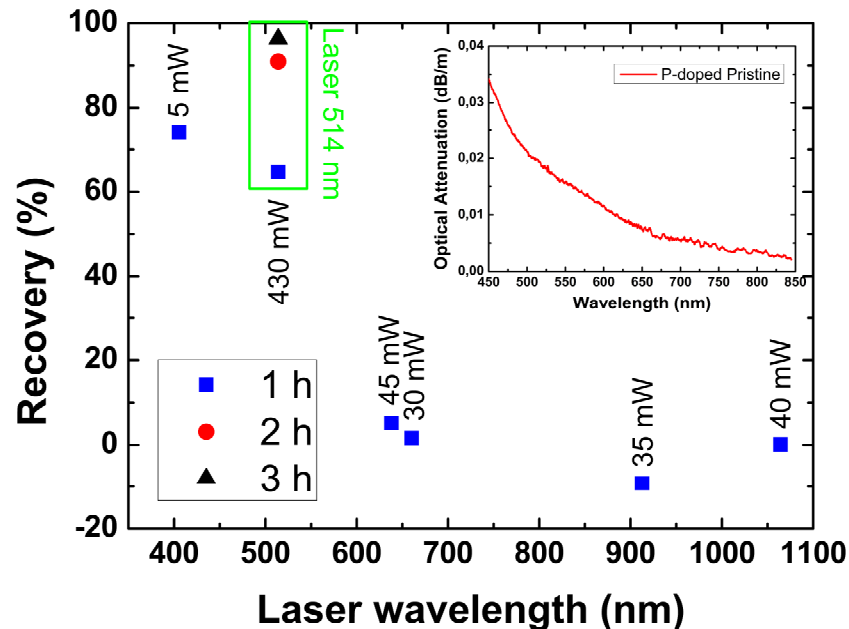


Figure 5.13 PB induced RIA recovery percentages at 1550 nm of P-doped OF samples, irradiated up to 1170 Gy with lasers varying in wavelength and powers. The inset shows the UV-VIS loss spectrum for the not irradiated P-doped SMOF.

Figure 5.14 highlights how the vertical jump, between the two reference spools, decreases with the increasing light injection time as well as the improvement in the signal-to-noise ratio. We bleached the FUT twice and irradiated it three times. The irradiation runs were followed by measurements using the OTDR and from the acquired traces we calculated the dose dependence of the RIA at 1550 nm reported in Figure 5.15. The irradiations induce very similar RIA dose dependences, demonstrating that the regenerated P-doped OF maintains its initial radiation sensitivity, or calibration, even after several PB processes. It is interesting to understand the basic mechanisms at stake during the PB process. In [33] Griscom *et al.* described the microscopic processes that are activated by isochronal annealing of samples irradiated at 77 K.

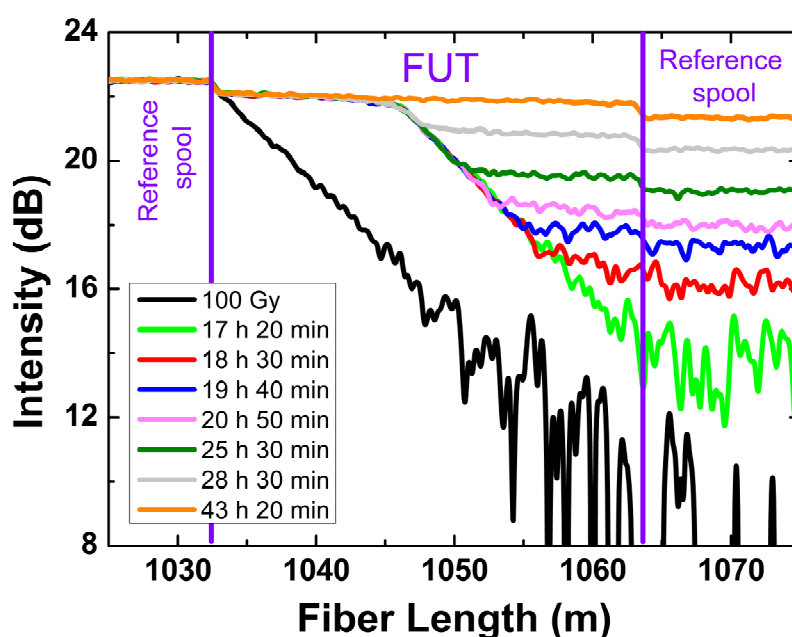


Figure 5.14 OTDR traces of the 30 m long P-doped sample, irradiated up to 100 Gy and bleached with 514 nm cw Argon laser line (430 mW) at different times after the beginning of the laser light injection.

In particular, they suggested the conversion of Phosphorus Oxygen Hole Centre (POHC) into P1 as both point defects are hole centres and basing on the observed opposite concentration kinetics as the temperature was increased. Other authors have corroborated this hypothesis by

noticing that, at room temperature, it is not unusual to observe a slight loss increase at 1550 nm after the end of an irradiation in P-doped OF [132,133]. Such mechanism could be related to the lower thermal stability of POHC with respect to P1. Another temperature activated mechanism that Griscom *et al.* put forward involves the P2 defect, which is an electron centre. In this case the increase of temperature would allow the trapped electrons to migrate and recombine with the hole defects. In our case, the two laser probe signals at 405.5 nm and 514 nm are clearly located in the absorption band of the metastable-POHC, but they do not produce an increase of P1 signature.

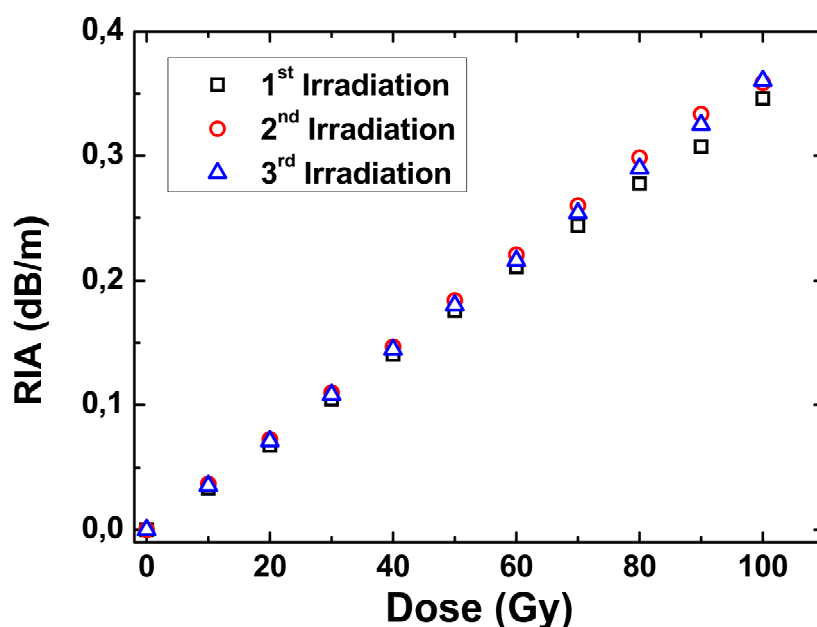


Figure 5.15 1550 nm RIA Vs Dose of the three irradiations after the two PB sequences of the 30 m P-doped sample carried out with 514 nm cw laser light.

On the contrary the P1 are significantly reduced. It is possible to imagine that both lasers at 405.5 nm and 514 nm are sufficiently close to the absorption bands of electron centres, such as the P2, to allow some of the trapped electrons to be released and recombine with the hole centres defects. Although the P2 absorption band is relatively far, as it peaks at 4.6 eV (270 nm), it has a very large FWHM ~ 1.27 eV [33]. Moreover, the electron paramagnetic resonance studies on

P-doped OFs irradiated at room temperature [46] and at liquid nitrogen temperature [33] have shown that, at the dose levels investigated in this work, the concentration of P2 centres is usually significantly higher than those of POHC and P1. Indeed, Griscom et al. have suggested an annealing induced recombination mechanisms such that $[POHC]+[P1]+[P4] \sim [P2]$ (at temperature below ~ 625 K). In our case, similar mechanisms could contribute during the PB treatment at RT. If this is correct, the PB effect should actually extend from the UV (using green light) to the IR domain.

Although we have not investigated the effects of PB phenomenon in the UV-Visible domain, we had during our tests a visual confirmation of the gradual PB effect due to the injected laser thanks to the radial light scattering observation along the OF samples. This is illustrated in Figure 5.16 that illustrates the gradual increasing propagation efficiency of the 514 nm laser light in the irradiated P-doped sample.

The same hypothesis is also strongly corroborated by another recent work reported in Ref. [134]. Based on these considerations, one might expect that the use of a shorter laser wavelength (resonant with the P2 absorption band) could maximize the bleaching effect. At the same time, from an application point of view, using very short wavelength would be quite limiting in terms of maximum OF length due to the intrinsic losses of the OF. For this reason, we consider the 514 nm cw Argon laser line as a good compromise for practical applications.

In conclusion, we presented a regeneration study of a radiation sensitive OF used for distributed dosimetry applications. The regeneration is obtained via PB effect, through the injection of visible cw-laser light. The most efficient PB was achieved with 405.5 nm laser light. In this case, it was possible to reach a recovery value of about 75% after one hour of light injection (5 mW) over a 1 m long OF irradiated at 1170 Gy. With the 30 m long sample irradiated up to 100 Gy, we reached a recovery value of about 97% with the 514 nm laser light at the higher power of 430 mW.

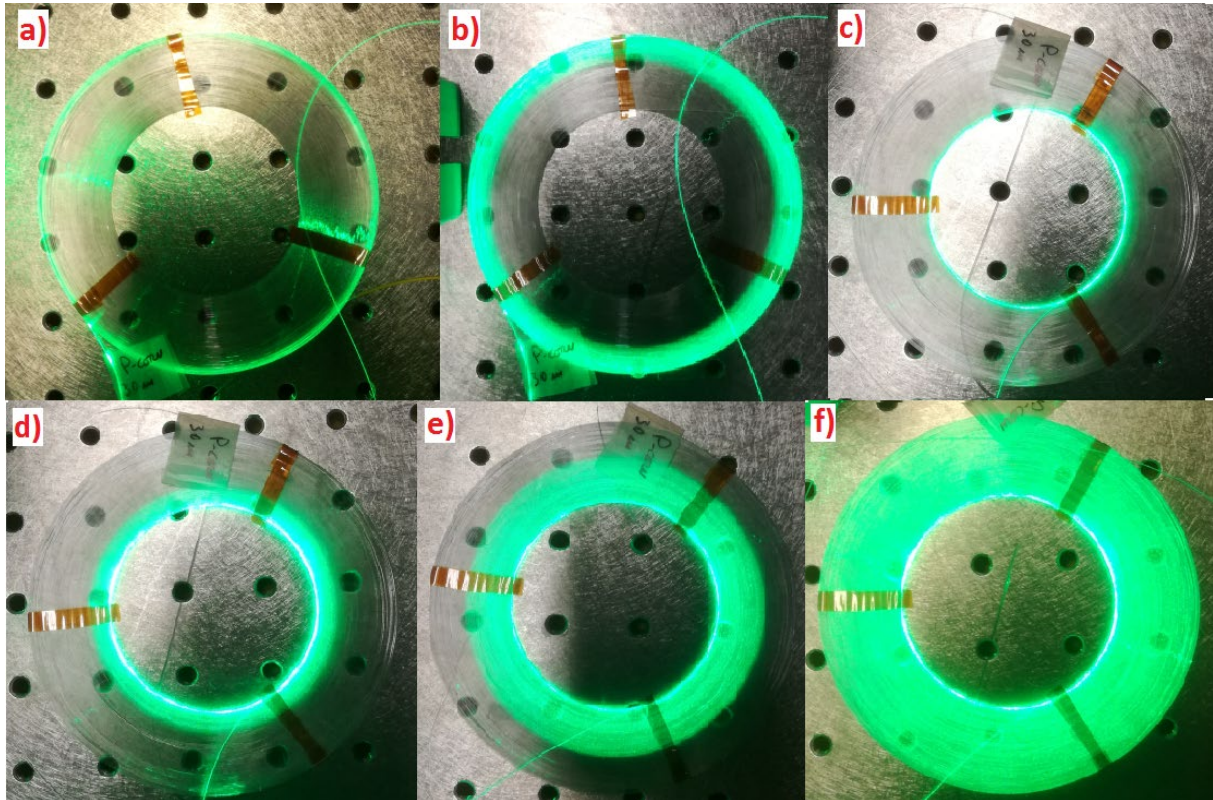


Figure 5.16 Radial light scattering of the recovery process. From a) to f) the progressive increasing of the light transmission injected from the out-side (a) and b)) and then from the inner side (from c) to e)). Finally the full recovery of the fiber and the light traveling through the whole sample f).

Summary: To the best of our knowledge, we have demonstrated for the first time the possibility to regenerate P-doped OF dosimeters operating in the IR domain. Moreover, we showed that the radiation sensitivity of the fiber remains unchanged by this regeneration process which means it is possible to reset the sensor for successive applications while keeping the same optical response. This technique is extremely significant for the regeneration of the distributed OF dosimeters employed at CERN by extending the lifetime of each sensor and reducing the corresponding maintenance costs.

5.4 Spatial resolution investigation

Among the various possible improvements of the DOFRS described in this work, one could concern the need to improve the spatial resolution of the current system based on optical time domain reflectometry. Today, using the radiation sensitive P-doped SMF, the selected OTDR operates at the wavelength of 1550 nm and offers the possibility to perform measurements with a spatial resolution of about one meter over distance of a few kilometres. The sensing distance is obviously reduced under irradiation due to the RIA increase and the limited OTDR budget. During the PhD thesis, we initiated a preliminary study to compare the performances of three different reflectometers in terms of spatial resolution. The working principles of all of them are based on the backscattered Rayleigh signal but the selected interrogation techniques allow achieving different spatial resolutions. The goal was to better understand their differences and evaluate their potential applications. The used instruments are an OTDR, a High Resolution (HR-) OTDR, both from VIAVI solutions and an Optical Frequency Domain Reflectometer (OBR4600) from Luna Technologies. The potential of OFDR for radiation sensing has been already discussed by A. Faustov in two pioneer papers [135] and [136].

In the OTDR or HR-OTDR systems, an optical laser pulse is launched into the fiber and the backscattered light is continuously detected at the launching end as a function of the time, and consequently as a function of the distance from the injecting end along the fiber length, from the flight time. The power of the backscattered light decays as the distance increases, because of the fiber attenuation. Therefore, the radiation induced defects in the fiber core and cladding increase the attenuation and induce a variation of the backscattered light profile as a function of the distance. The spatial resolution depends on the temporal bandwidth of the light pulse, generally a 10 ns pulse corresponds to a spatial resolution of 1 m (OTDR) while a 3 ns pulse corresponds to a resolution of about 30 cm.

In the OFDR system a continuous wave tunable laser around 1550 nm, whose optical frequency is linearly swept in time, is used as light source. Mixing the backscattered light from the sample and the injected light as a reference, interference fringes containing the beat frequency are generated. Processing the interference fringe by Fourier Transform (FFT) the Rayleigh pattern as a function of the length is obtained. From the Rayleigh pattern obtained by both types of instruments, we can calculate the RIA of the fiber. For the OFDR the spatial resolution is inversely proportional to the range in which the laser frequency is swept: a spatial resolution from 1 cm to 40 μm can be reached in the sensing range from 2 km to 10 m, respectively. In Figure 5.17, we compare the spectral domains of operation of the OTDR or HR-OTDR and the OFDR with the RIA spectra of a phosphosilicate SMOF measured at a dose of 100 Gy(SiO_2) either by X-rays or γ -rays. It can be seen that in the spectral range of the OFDR source (1529 to 1571 nm), the RIA level is almost constant as we are for the tested optical fiber at the top of the optical absorption related to the P1 defects.

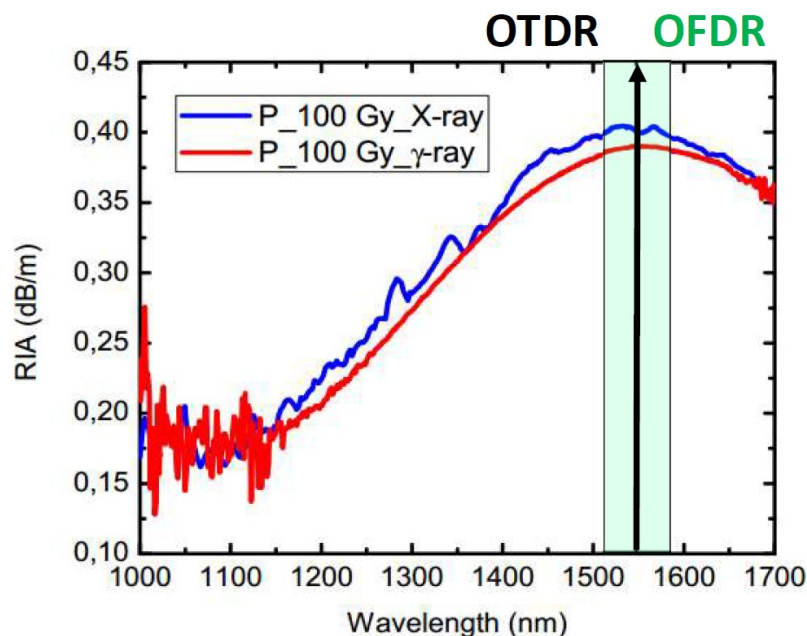


Figure 5.17 Comparison between the OTDR (or HR-OTDR) and OFDR spectral domains of operation and the RIA spectra measured for the P-doped SMOF after an irradiation dose of 100 Gy(SiO_2) (room temperature) either deposited by g-rays or X-rays.

Figure 5.18 a), b) and c) illustrate an example of the different spatial resolutions of the three instruments when monitoring a sample of P-doped fiber, length about 1 m, during the irradiation. The irradiation conditions were the following: a dose rate of 0.2 Gy/s at RT during about 123 minutes to reach a total accumulated dose of 1.5 kGy. Figure 5.18 d), and e) illustrate the results obtained with the OFDR when lengths of 0.5 m and 0.25 m are respectively irradiated in the same conditions.

The setup for the monitoring instrumentations were:

- **OTDR:**

$\lambda = 1550$ nm; pulse width = 10 ns; sampling resolution = 4 cm; time acquisition = 30 s;

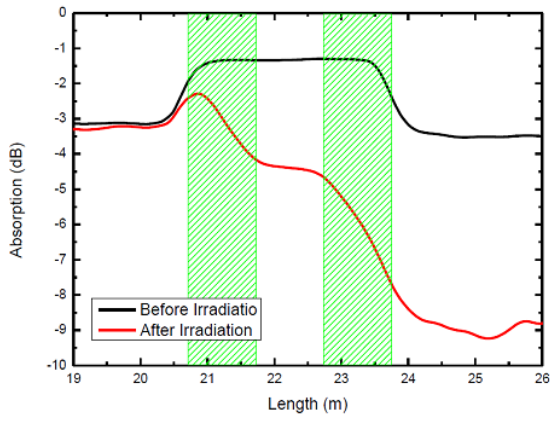
- **HR-OTDR:**

$\lambda = 1550$ nm; pulse width = 3 ns; sampling resolution = 4 cm; time acquisition = 30 s;

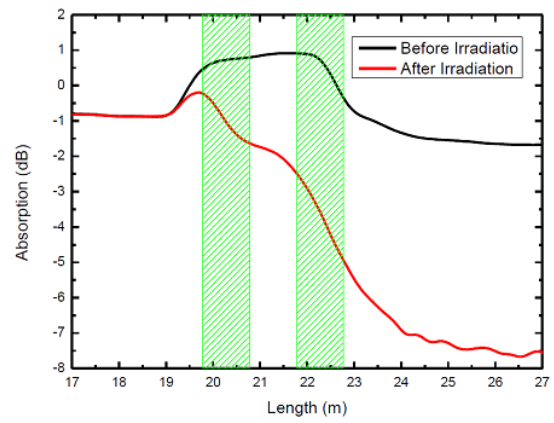
- **OFDR:**

scan range = 1529.321-1571.247 nm; gain = 24 dB;

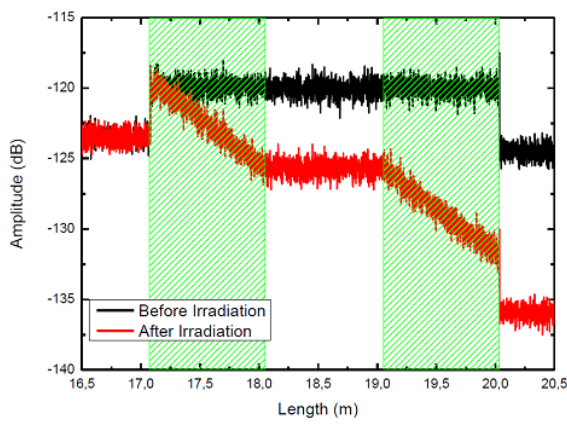
The peak we see in the OTDR and HR-OTDR traces is due to the splice between the rad-hard pigtailed, used to connect the sample to the interrogators and the sample itself. It should be noted that the setup could have been improved to limit its impact on the quality of the RIA measurements. In green we highlight the irradiated part of the P-doped sample that presents a higher Rayleigh backscattering. When the irradiated part is 1 m long, all equipment's are able to clearly detect the irradiated zones and associated losses (of about 3 dB/m at 1550 nm). Of course, the OFDR presents the best spatial resolution despite the fact that this system is not primarily designed for such operation. With the OFDR, our preliminary tests on reduced irradiated lengths of 0.5 m and 0.25 m show that 1 kGy related RIA (about 0.75 dB) can be detected quite easily over 25 cm.



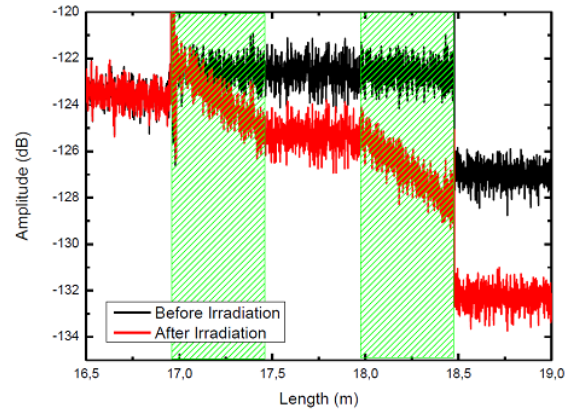
(a)



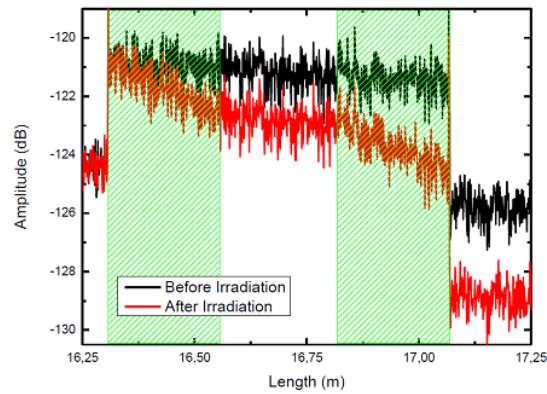
(b)



(c)



(d)



(e)

Figure 5.18 Traces of three instruments before and after the irradiation of a P-doped OF sample length of 1 m. In a) the OTDR trace, in b) the HR-OTDR trace and in c) the OFDR trace d). The areas highlighted in green indicate the parts of the sample that have been irradiated.

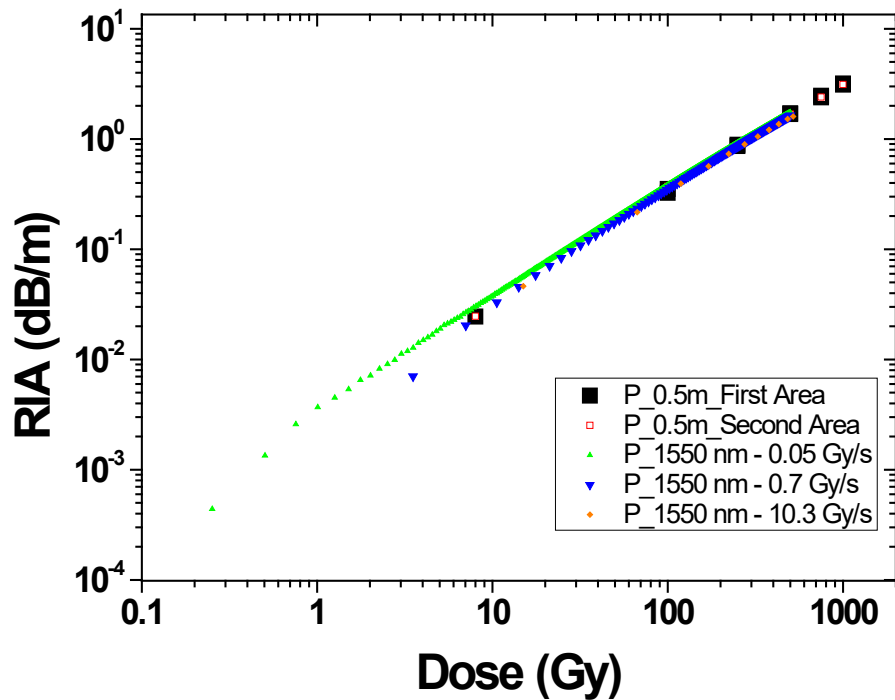


Figure 5.19 Comparison between the dose dependences of the RIA of the P-doped SMF measured with the OTDR at three different dose rates and by the OFDR on 50cm long fiber samples.

A last important point that has been checked concerns the calibration coefficient of the fiber that is used to convert the RIA into a deposited dose. To compare the dose dependences of the RIA as measured by the OTDR and the OFDR, we used the same experimental setup and irradiated at different doses (from 10 Gy to 1 kGy) two 50 cm samples of the P-doped SMF. The obtained results are summarized in Figure 5.19 and show the good correspondence between the results of the two techniques.

Summary: These results clearly show that the calibration curve of the P-doped fiber remain the same for the OFDR. OFDR can then be used for online dosimetry measurements in this range of dose and dose rate. Additional experiments are needed to fully assess the advantages of this interrogator in terms of spatial resolution and the limitations in terms of optical budget.

Conclusions & Perspectives

In this work, we have studied the behaviors of three diversely doped OFs with the aim to improve our understanding about their potential use as radiation dosimeters. We investigate the response of our fibers varying the dose, dose-rate, temperature and environment condition (X-ray, γ -ray, mix irradiation, proton and neutron). We also carried out online and post-mortem measurement studying the spontaneous recovery of the fibers after the end of irradiation and its impact on subsequent irradiations. The P-doped fiber appears as the most suitable fiber type to be used as a radiation dosimeter. In the NIR range of interest RIA of P-doped OF is due to P1 defect centered at around 1560 nm. The radiation response of the fiber at 1550 nm is linear until 500 Gy and the sensitivity variation varying the dose-rate is within the experimental error [91]. We confirm the absence of a temperature dependence of the RIA at both 1310 and 1550 nm in the P-doped fiber, in the studied temperature range (RT-50 °C), reinforces the idea to use it as radiation dosimeter [46,115]. The fiber has not spontaneous recovery after irradiation at the wavelength of interest. Concerning the multi-step irradiation at different dose-rates, the results found are not easy to interpret, although interesting, and further studies are needed to improve understanding of the phenomena occurring.

The introduction of Cerium as co-dopant makes the fiber less sensitive. This causes the fiber to lose its characteristics as a good dosimeter, but at the same time expands the range of potentially detectable radiation levels, and thus its range of application. Regarding the PCe-doped OF we found a slight dependence on both dose-rate and irradiation temperature. In addition, it is evident from the results that a spontaneous recovery begins immediately after the end of irradiation and that the fiber response also depends on the dose-rate. In conclusion, a possible use of this fiber as a radiation sensor presupposes a deep knowledge of the environment to be

investigated and an ad-hoc calibration as well as a more detailed study regarding spontaneous recovery.

Aluminum-doped fiber has shown promising characteristics for use as a radiation detection in the present investigation, but less for the dosimetry application. The Al-doped fiber is more sensitive than the P-doped fiber around 1550 nm, our benchmark, and therefore lends itself to the detection of lower dose rate radiation environments. The fiber has no dependence of the RIA on the dose rate and the irradiation temperature; it seems to have a weak spontaneous recovery that makes it less adapted for the dosimetry than the P-doped fibers for CERN applications.

A crucial part of this thesis work was the study of laser light stimulated recovery of irradiated fibers, *photobleaching*. We performed the measurement using the P-doped OF, the fiber that from the application point of view has more interest for us. The best result we got was with 30 m-long sample irradiated up to 100Gy, we reached a recovery value of about 97% with the 514 nm laser light at the higher power of 430 mW [124]. To the best of our knowledge, we have demonstrated for the first time the possibility to regenerate P-doped OF dosimeters operating in the IR domain. Moreover, we showed that the radiation sensitivity of the fiber remains unchanged by this regeneration process, which means it is possible to reset the sensor for successive applications while keeping the same optical response. This technique is extremely significant for the regeneration of the distributed OF dosimeters employed at CERN by extending the lifetime of each sensor and reducing the corresponding maintenance costs.

The last part of the thesis is dedicated to a test comparison between OTDR and OFDR. We presented also the measurement carried out in the Proton Synchrotron Booster and the comparison with point dosimeters installed in some focus points along the machine close to the fiber performed with a system that was implemented before this PhD work and that employed

a MM optical fibre. Such fibre did not have a response to radiation as good as the one reported in [91]. Consequently some systematic errors were observed with this system. As discussed above, there are several advantages to the DOFRS system as to monitoring online the whole environment. The measuring instrument, the OTDR, is installed in a safe area and is therefore always accessible, it is also possible to replace (*cable blowing*) or regenerate (*photobleaching*) the fiber without having to access the dangerous environment where it is installed.

The DOFRS has been successfully tested at CHARM facility in 2016 [81 ,137]. Subsequently, the first operational prototype for dose detection was installed in the PS Booster during 2016/17 EYETS [138]. This prototype started acquiring data at the beginning of 2017 operations and the results of this first real case scenario implementation are reported in ref. [82]. Because of the numerous limitations of the first prototype a new version of the system (sensors, interrogators, data analysis) was installed in the PS during YETS 2017/18 [139]. During the LS2 DOFRS systems has been installed in SPS and in several part of LHC near the main experiments and elsewhere

References

- [1] K. C. Kao and G. A. Hockham, 'Dielectric-fibre surface waveguides for optical frequencies', vol. 133, no. 3, p. 8, 1986.
- [2] A. H. Hartog, *An Introduction to Distributed Optical Fibre Sensors*.
- [3] X. Bao and L. Chen, "Recent Progress in Distributed Fiber Optic Sensors", *Sensors*, vol. 12, no. 7, Art. no. 7, Jun. 2012, doi: 10.3390/s120708601.
- [4] A. Thornton, 'CHARM Facility Test Area Radiation Field Description', p. 51.
- [5] W. J. Bock, I. Gannot, and S. Tanev, Eds., *Optical waveguide sensing and imaging: proceedings of the NATO Advanced Study Institute on Optical Waveguide Sensing and Imaging in Medicine, Environment, Security and Defence*, Gatineau, Québec, Canada, 12 - 21 October 2006. Dordrecht: Springer, 2008.
- [6] S. Girard et al., "Recent advances in radiation-hardened fiber-based technologies for space applications", *Journal of Optics*, vol. 20, no. 9, p. 093001, Sep. 2018, doi: 10.1088/2040-8986/aad271.
- [7] S. Girard et al., "Radiation Effects on Silica-Based Optical Fibers: Recent Advances and Future Challenges", *IEEE Trans. Nuc. Sci.*, vol. 60, no. 3, pp. 2015–2036, Jun. 2013, doi: 10.1109/TNS.2012.2235464.
- [8] E. J. Friebele, "Optical fiber waveguides in radiation environments", *Opt. Eng.*, vol. 18, no. 6, pp. 552–561, 1979
- [9] E. J. Friebele, C. G. Askins, M. E. Gingerich, and K. J. Long, "Optical fiber waveguides in radiation environments, II", *Nuclear Instruments and Methods in Physics Research Section B: Beam Interactions with Materials and Atoms*, vol. 1, no. 2–3, pp. 355–369, Feb. 1984, doi: 10.1016/0168-583X(84)90092-2.
- [10] W. Primak, "Fast-Neutron-Induced Changes in Quartz and Vitreous Silica", *Physical Review*, vol. 110, no. 6, pp. 1240–1254, Jun. 1958, doi: 10.1103/PhysRev.110.1240.
- [11] E. Lell, N. J. Hensler, and J. R. Hensler, J. Burke, Ed., "Radiation effects in quartz, silica and glasses", in *Progr. Ceramic Sci.*, New York, 1966, vol. 4, pp. 3–93, Pergamon.

-
- [12] J.D. Jackson, *Classical Electrodynamics*, 3rd ed.; John Wiley & Sons Inc.: Hoboken, NJ, USA, 2009.
- [13] M. Froggatt and J. Moore, “High-spatial-resolution distributed strain measurement in optical fiber with Rayleigh scatter”, *Applied Optics*, vol. 37, no. 10, p. 1735, Apr. 1998, doi: 10.1364/AO.37.001735.
- [14] D. Marcuse, “*Theory of Dielectric Optical Waveguides*”, Academic Press, 1991.
- [15] J-M. Jonathan, "Guided and Coupled waves : an overview of optical fibers and derived components for optical communications", Lecture notes, Institut Optique Graduate School, 2020
- [16] M.J. Adams, “*An Introduction to Optical Waveguides*”, (Wiley, Chichester, 1981).
- [17] R. Kerslake, W. Liese, K. Kowaliuk, and P. Pilon, “Differentiating core and cladding attenuation in single-mode fiber”, *Fiber and Integrated Optics*, vol. 10, no. 1, pp. 57–63, Jan. 1991, doi: 10.1080/01468039108201605.
- [18] O. V. Ivanov, S. A. Nikitov, and Y. V. Gulyaev, “Cladding modes of optical fibers: properties and applications”, *PHYS-USP*, vol. 49, no. 2, p. 167, 2006, doi: 10.1070/PU2006v049n02ABEH005784.
- [19] A. Joy and K. Ghatak, “Leaky modes in optical waveguides”, *Optical and Quantum Electronics* 17 (1985) 311-321.
- [20] A. W. Snyder and J. D. Love, ‘Tunnelling leaky modes on optical waveguides’, *Optics Communications*, vol.12, no. 3, Nov. 1974, doi: 10.1016/0030-4018(74)90026-1.
- [21] S. Girard et al., “Overview of radiation induced point defects in silica-based optical fibers”, *Reviews in Physics*, vol. 4, p. 100032, Nov. 2019, doi: 10.1016/j.revip.2019.100032.
- [22] S. Girard, J. Baggio, and J. Bisutti, “14-MeV Neutron, γ -Ray, and Pulsed X-Ray Radiation-Induced Effects on Multimode Silica-Based Optical Fibers”, *IEEE Trans. Nuc. Sci.*, vol. 53, no. 6, Art. no. 6, Dec. 2006, doi: 10.1109/TNS.2006.886222.
- [23] G. M. Ermolaeva, “Low-dispersion optical fiber highly transparent in the UV spectral range”, *Opt. Eng*, vol. 43, no. 12, p. 2896, Dec. 2004, doi: 10.1117/1.1814766.
- [24] W.H.Zachariasen, “The Atomic Arrangementt in Glass”, *J. Am. Chem. Soc.*, vol. 54, p. 3841, 1932.

-
- [25] G. Pacchioni, L. Skuja and D. L. Griscom, “Defects in SiO₂ and Related Dielectrics: Science and Technology”, Kluwer Academic, 2000. doi: 10.1007/978-94-010-0944-7
- [26] D. Ehrt, P. Ebeling, and U. Natura, “UV Transmission and radiation-induced defects in phosphate and fluoride-phosphate glasses”, *J. of Non-Cryst Solids*, 263&264, 240-250, 2000, doi.org/10.1016/S0022-3093(99)00681-X
- [27] P. C. Becker, N. A. Olsson et al. J. R. Simpson, *Erbium-Doped Fiber Amplifiers, Fundamental and Technology*, London: Academic Press, 1999.
- [28] J. Laegsgaard, *Phys. Rev. B*, 65, 174114-1, 2002. doi: 10.1103/PhysRevB.65.174114
- [29] S. Magne, Y. Ouerdane, M. Druetta, J. Goure, P. Ferdinand et G. Monnom, “Cooperative luminescence in an ytterbium-doped silica fibre”, *Opt. Comm.*, vol. 11, p. 310, 1994.
- [30] S. Girard et al., “On-site Regeneration Technique for Hole-Assisted Optical Fibers Used In Nuclear Facilities”, *IEEE Trans. Nucl. Sci.*, vol. 62, no. 6, Art. no. 6, Dec. 2015, doi: 10.1109/TNS.2015.2484353.
- [31] T. Deschamps, N. Ollier, H. Vezin et C. Gonnet, vol. *J. Chem. Phys.*, p. 014503/1, 2012. doi.org/10.1063/1.3670416
- [32] E. Regnier, I. Flammer, S. Girard, F. Gooijer, F. Achten, and G. Kuyt, “Low-Dose Radiation-Induced Attenuation at InfraRed Wavelengths for P-Doped, Ge-Doped and Pure Silica-Core Optical Fibres”, *IEEE Trans. Nucl. Sci.*, vol. 54, no. 4, Art. no. 4, Aug. 2007, doi: 10.1109/TNS.2007.894180.
- [33] D.L. Griscom, E.L. Friebele and K.J. Long, “Fundamental defect centers in glass: Electron spin resonance and optical absorption studies of irradiated phosphorus-doped silica glass and optical fibers”, *J. Appl. Phys.*, vol. 54, p. 3743/3762, Jul. 1983.
- [34] G. Origlio, F. Messina, S. Girard, M. Cannas, A. Boukenter, and Y. Ouerdane, “Spectroscopic studies of the origin of radiation-induced degradation in phosphorus-doped optical fibers and preforms”, *J. Appl. Phys.*, vol. 108, no. 12, Art. no. 12, Dec. 2010, doi: 10.1063/1.3517479.
- [35] L. Giacomazzi et al., “Optical absorption spectra of P defects in vitreous silica”, *Opt. Mat. Express*, vol. 8, no. 2, Art. no. 2, Feb. 2018, doi: 10.1364/OME.8.000385.
- [36] J.S. Stroud, “Color centers in a cerium-containing silicate glass”, *J. Chem. Phys.* 37 (4) (1962) 836–841, <https://doi.org/10.1063/1.1733170>.

-
- [37] J. S. Stroud, "Photoionization of Ce^{3+} in Glass", *J. Chem. Phys.*, vol. 35, p. 844, 1961. doi.org/10.1063/1.1701227
- [38] E. Anokin, A. Guryanov, D. Gusovskii, V. Mashinskii, S. M. V. Neustruev, V. Tikhomirov, and Y. B. Zverev, "UV and gamma radiation damage in silica glass and fibres doped with germanium and cerium", *Nuclear Instruments and Methods in Physics Research B65* (1992) 392-396.
- [39] M. Fasoli et al., "Effect of reducing sintering atmosphere on Ce-doped sol-gel silica glasses", *J. Non-Cryst. Solids*, vol. 355, no. 18–21, pp. 1140–1144, Jul. 2009, doi: 10.1016/j.jnoncrysol.2009.01.043.
- [40] D. Di Francesca "Role of Dopants, Interstitial O_2 and Temperature in the Effects of Irradiation on Silica-based Optical Fibers", PhD Thesis, Université de Saint-Etienne, Università di Palermo, 2015
- [41] H. Hideo and K. Hiroshi, "Radiation-induced coloring and paramagnetic centers in synthetic $SiO_2:Al$ glasses", *Nuclear Instruments and Methods in Physics Research Section B: Beam Interactions with Materials and Atoms*, vol. 91, no. 1–4, Art. no. 1–4, Jun. 1994, doi: 10.1016/0168-583X(94)96255-3.
- [42] F. Mady, A. Guttilla, M. Benabdesselam, W. Blanc, S. Girard, Y. Ouerdane, A. Boukenter, H. Desjonquères, C. Monsanglant-Louvet, "Optical fibers under irradiation: quantitative assessment of the energy distribution of radiation-induced trapped states", *SPIE Photonics* (2020). doi: 10.1117/12.2557834
- [43] M. Engholm, P. Jelger, F. Laurell, and L. Norin, "Improved photodarkening resistivity in ytterbium-doped fiber lasers by cerium codoping", *Opt. Lett.*, vol. 34, no. 8, Art. no. 8, Apr. 2009, doi: 10.1364/OL.34.001285.
- [44] J. C. Lagomacini, D. Bravo, A. Martín, F. J. López, P. Martín, and Á. Ibarra, "Growth kinetics of AlOH defects in γ -irradiated silica glasses", *J. Non-Cryst. Solids*, vol. 403, pp. 5–8, Nov. 2014, doi: 10.1016/j.jnoncrysol.2014.04.005.
- [45] A. N. Trukhin, J. Teteris, A. Fedotov, D. L. Griscom, and G. Buscarino, "Photosensitivity of SiO_2-Al and SiO_2-Na glasses under ArF (193nm) laser", *J. Non-Cryst. Solids*, vol. 355, no. 18–21, Art. no. 18–21, Jul. 2009, doi: 10.1016/j.jnoncrysol.2008.11.037.

-
- [46] G. Li Vecchi et al., “Infrared radiation Induced attenuation of radiation sensitive optical fibers: influence of temperature and modal propagation”, *Opt. Fib. Tech.*, vol. 55, p. 102166, Mar. 2020, doi: 10.1016/j.yofte.2020.102166.
- [47] A. V. Faustov et al., “Comparison of Gamma-Radiation Induced Attenuation in Al-Doped, P-Doped and Ge-Doped Fibres for Dosimetry”, *IEEE Trans. Nucl. Sci.*, vol. 60, no. 4, Art. no. 4, Aug. 2013, doi: 10.1109/TNS.2013.2273273.
- [48] A. V. Faustov et al., “Remote distributed optical fibre dose measuring of high gamma-irradiation with highly sensitive Al- and P-doped fibres”, Prague, Czech Republic, May 2013, p. 877404, doi: 10.1117/12.2017331.
- [49] A. Alessi et al., “Radiation Effects on Aluminosilicate Optical Fibers: Spectral Investigations From the Ultraviolet to Near-Infrared Domains”, *Phys. Stat. Sol. (a)*, Sep. 2018, doi: 10.1002/pssa.201800485.
- [50] A. S. Zyubin, A. M. Mebel, and S. H. Lin, “Quantum chemical modeling of photoabsorption and photoluminescence of the $[AlO_4]^0$ defect in bulk SiO_2 ”, *J. Chem. Phys.*, vol. 119, no. 21, p. 8, 2003. doi.org/10.1063/1.1622660
- [51] S. O’Keeffe, C. Fitzpatrick, E. Lewis, and A. I. Al-Shamma’a, “A review of optical fibre radiation dosimeters”, *Sensor Review*, vol. 28, no. 2, Art. no. 2, Mar. 2008, doi: 10.1108/02602280810856705.
- [52] T. Yanagida, G. Okada, and N. Kawaguchi, “Ionizing-radiation-induced storage-luminescence for dosimetric applications”, *J. of Luminescence*, vol. 207, pp. 14–21, Mar. 2019, doi: 10.1016/j.jlumin.2018.11.004.
- [53] S. H. Law, N. Suchowerska, D. R. McKenzie, S. C. Fleming, and T. Lin, “Cerenkov radiation in optical fibres”, *ACOFT/AOS 2006 - Australian Conference on Optical Fibre Technology/Australian Optical Society*, Melbourne, Australia, Jul. 2006, pp. 100–102, doi: 10.1109/ACOFT.2006.4519267.
- [54] I. I. Mahmoudi, A. E.-N. A. Mohamed, and A. N. Z. Rashed, “Modeling of radiation induced luminescence and how to reduce Cherenkov effect in optical fibers”. Published in 5th ICMIC, 2013.
- [55] M. J. Marrone, “Radiation-induced luminescence in silica core optical fibers”, *Appl. Phys. Lett.*, vol. 38, no. 3, pp. 115–117, Feb. 1981, doi: 10.1063/1.92294.

-
- [56] E. Damulira, M. N. S. Yusoff, A. F. Omar, and N. H. Mohd Taib, “A Review: Photonic Devices Used for Dosimetry in Medical Radiation”, *Sensors*, vol. 19, no. 10, p. 2226, May 2019, doi: 10.3390/s19102226.
- [57] L. Bøtter-Jensen, S. W. S. McKeever, and A. G. Wintle, *Optically stimulated luminescence dosimetry*, 1st ed. Amsterdam ; Boston ; London: Elsevier, 2003.
- [58] N. A. Helou et al., “Radioluminescence and Optically Stimulated Luminescence Responses of a Cerium-doped Sol-gel Silica Glass under X-ray Beam Irradiation”, *IEEE Trans. Nucl. Sci.*, pp. 1–1, 2017, doi: 10.1109/TNS.2017.2787039.
- [59] B. C. Bhatt, “Thermoluminescence optically stimulated luminescence and radiophotoluminescence dosimetry: an overall perspective”, *Radiat Prot Environ* 2011; 34:6-16. <https://www.rpe.org.in/text.asp?2011/34/1/6/93897>
- [60] C. Furetta, *Handbook of Thermoluminescence*, 1st ed. Singapore: World Scientific, 2003. doi.org/10.1142/7187
- [61] F. Ravotti, “Dosimetry Techniques and Radiation Test Facilities for Total Ionizing Dose Testing”, *IEEE Trans. Nucl. Sci.*, vol. 65, no. 8, pp. 1440–1464, Aug. 2018, doi: 10.1109/TNS.2018.2829864.
- [62] D.L. Griscom, M.E. Gingerich, E.J. Friebele, “Model for the dose, dose-rate and temperature dependence of radiation-induced loss in optical fibers”, *IEEE Trans. Nucl. Sci.* 41 (1994) 523.
- [63] H. Henschel, O. Köhn, H.U. Schmidt, “Influence of dose rate on radiation induced loss in optical fibres”, in *Proc. 1399 SPIE*, 1991, p. 49.
- [64] E.J. Friebele, C.G. Askins, M.E. Gingerich, “Effect of low dose rate irradiation on doped silica core optical fibers”, *Appl. Opt.* 23 (1984) 4202 1984.
- [65] S. Girard, et al., “Combined high dose and temperature radiation effects on multimode silica-based optical fibers”, *IEEE Trans. Nucl. Sci.* 60 (2013) 4305.
- [66] A.T. Ramsey, W. Tighe, J. Bartolick, P.D. Morgan, “Radiation effects on heated optical fibers”, *Rev. Sci. Instrum.* 68 (1997) 632.
- [67] P. Borgermans, “Spectral and Kinetic Analysis of Radiation Induced Optical Attenuation in Silica: Towards Intrinsic Fiber Optic Dosimetry?”, *Thèse de doctorat*, Vrije Universiteit, Brussels, 2001.

-
- [68] B. Brichard, S. Agnello, L. Nuccio, L. Dusseau, “Comparison between point defect generation by gamma-rays in bulk and fibre samples of high purity amorphous silica”, *IEEE Trans. Nucl. Sci.* 55 (2008) 2121. doi.org/10.1109/TNS.2008.2001706
- [69] S. Girard, et al., “Transient radiation effects on optical fibers for megajoule class lasers: influence of MCVD process parameters”, *IEEE Trans. Nucl. Sci.* 59 (2012) 2894.
- [70] G. Origlio, et al., “Influence of the drawing process on the defect generation in multistep-index germanium-doped optical fibers”, *Opt. Lett.* 34 (2009) 2282.
- [71] J. Kuhnehn, H. Henschel, U. Weinand, “Influence of coating material, cladding thickness, and core material on the radiation sensitivity of pure silica core step-index fibers”, presented at the 8th Eur. Conf. RADECS (2005) paper A2.
- [72] D.L. Griscom, M. E. Gingerich and E. J. Friebele, “Model for the dose, dose-rate and temperature dependence of radiation induced loss in optical fibers”, *IEEE Trans. Nucl. Sci.* 41 523–6 (1994).
- [73] D. L. Griscom, “Fractal kinetics of radiation-induced point defect formation and decay in amorphous insulators: application to color centers in silica-based optical fibers”, *Phys. Rev. B* 64 174201 (2001). doi: 10.1103/PhysRevB.64.174201
- [74] O. Gilard, M. Caussanel, H. Duval, G. Quadri and F. Reynaud, “New model for assessing dose, dose rate, and temperature sensitivity of radiation-induced absorption in glasses”, *J. Appl. Phys.* 108 093115 (2010). doi.org/10.1063/1.3503370
- [75] R. A. B. Devine, “On the physical models of annealing of radiation induced defects in amorphous SiO₂,” *Nucl. Instrum. Meth. Phys. Res. B* 46 261–4 (1990).
- [76] D. T. H. Liu and A. R. Johnston, “Theory of radiation induced absorption in optical fibers”, *Opt. Lett.* 19 548–50 (1994).
- [77] E. J. Friebele and D. L. Griscom, “Radiation effects in glass”, *Treatise on Materials Science and Technology* ed M T Doremus (New York: Academic) (1979).
- [78] E. J. Friebele, M. E. Gingerich and D. L. Griscom, “Survivability of optical fibers in space”, *Proc. SPIE* 1791 177–88 (1992).
- [79] H. Henschel, “Fibre optic radiation sensor systems for particle accelerators”, *Nuclear Instrument and Method in Phys. Res. A*, vol. 526, pp. 537–550, 2004. doi:10.1016/j.nima.2004.02.030

-
- [80] D. Di Francesca, A. Infantino, G. Li Vecchi, S. Girard, A. Alessi, Y. Kadi, M. Brugger, "Dosimetry Mapping of Mixed Field Radiation Environment through Combined Distributed Optical Fiber Sensing and FLUKA Simulation", *IEEE Trans. Nucl. Sci.*, vol.66 (1), pp. 299 - 305 (2019). doi: 10.1109/TNS.2018.2882135
- [81] I. Toccafondo et al., "Distributed Optical Fiber Radiation Sensing in a Mixed-Field Radiation Environment at CERN", *J. Lightw. Technol.*, vol. 35, no. 16, pp. 3303–3310, Aug. 2017, doi: 10.1109/JLT.2016.2608849.
- [82] D. Di Francesca et al., "Distributed Optical Fiber Radiation Sensing in the Proton Synchrotron Booster at CERN", *IEEE Trans. Nucl. Sci.*, vol. 65, no. 8, pp. 1639–1644, Aug. 2018, doi: 10.1109/TNS.2018.2818760.
- [83] G. Li Vecchi et al., "Distributed Optical Fiber Radiation Sensing at CERN", *Proceedings of the 9th Int. Particle Accelerator Conf., IPAC2018, Vancouver, BC, Canada, 2018*, doi: 10.18429/jacow-ipac2018-wepaf083.
- [84] Ravotti, "Development and Characterisation of Radiation Monitoring Sensors for the High Energy Physics Experiments of the CERN LHC Accelerator", Ph.D. dissertation, Montpellier, France, 2006.
- [85] F. Ravotti, M. Glaser, A. B. Rosenfeld, M. L. F. Lerch, A. G. Holmes-Siedle, and G. Sarrabayrouse, "Radiation Monitoring in Mixed Environments at CERN: From the IRRAD6 Facility to the LHC Experiments", *IEEE Trans. Nucl. Sci.*, vol. 54, no. 4, pp. 1170–1177, Aug. 2007, doi: 10.1109/TNS.2007.892677.
- [86] T. Yamamoto, A. Rosenfeld, T. Kron, F. d'Errico, and M. Moscovitch, "RPL Dosimetry: Principles and Applications", 2011, pp. 217–230. doi: 10.1063/1.3576169.
- [87] M. S. Andjelković, G. S. Ristić and A. B. Jakšić, "Using RADFET for the real-time measurement of gamma radiation dose rate", *Meas. Sci. Technol.* 26 025004 (2015). doi:10.1088/0957-0233/26/2/025004
- [88] <https://photonics.ixblue.com/>
- [89] S. Girard, J. Keurinck, Y. Ouerdane, J.-P. Meunier, and A. Boukenter, "γ-Rays and Pulsed X-Ray Radiation Responses of Germanosilicate Single-Mode Optical Fibers: Influence of Cladding Codopants", *J. Lightw. Technol.*, vol. 22, no. 8, pp. 1915–1922, Aug. 2004. doi: 10.1109/JLT.2004.832435

-
- [90] E. W. Mies and L. Soto. “Characterization of the Radiation Sensitivity of Single-Mode Optical Fibers”, IOOC-ECOC, 1985, pp. 255-258.
- [91] D. Di Francesca et al., “Qualification and Calibration of Single-Mode Phosphosilicate Optical Fiber for Dosimetry at CERN”, *J. Lightw. Technol.*, vol. 37, no. 18, pp. 4643–4649, Sep. 2019, doi: 10.1109/JLT.2019.2915510.
- [92] A.K. Sang, M.E. Froggatt, D.K. Gifford, S.T. Kreger, B.D. Dickerson, “One Centimeter Spatial Resolution Temperature Measurements in a Nuclear Reactor Using Rayleigh Scatter in Optical Fiber”, *IEEE Journal Sensors*, 8(7), 1375-1380 (2008).
- [93] A. Faustov, A. Gusarov, P. Mégret, M. Wuilpart, A.V. Zhukov, S. G. Novikov, V. Svetukhin, and A.A. Fotiadi, “The Use of Optical Frequency Domain Reflectometry in Remote Distributed Measurements of the γ Radiation Dose,” *Technical Physics Letters*, 41(5), 414–417 (2015).
- [94] A. Faustov, “Advanced fiber optics temperature and radiation sensing in harsh environments”, Ph.D. dissertation, Université de Mons, Mons, Belgium (2014).
- [95] K. Aoyama, K. Nakagawa, and T. Itoh, “Optical time domain reflectometry in a single-mode fiber”, *IEEE J. Quantum Electron.*, vol. 17, no. 6, pp. 862–868, Jun. 1981, doi: 10.1109/JQE.1981.1071237.
- [96] R. Hui and M. S. O’Sullivan, *Fiber optic measurement techniques*. Amsterdam ; London: Elsevier/Academic Press, 2009.
- [97] K. Yuksel, M. Wuilpart, V. Moeyaert, and P. Megret, “Optical frequency domain reflectometry: A review”, in 2009 11th International Conference on Transparent Optical Networks, Ponta Delgada, Portugal, Jun. 2009, pp. 1–5. doi: 10.1109/ICTON.2009.5185111.
- [98] J. Mekki, M. Brugger, R. G. Alia, A. Thornton, N. C. D. S. Mota, and S. Danzeca, “CHARM: A Mixed Field Facility at CERN for Radiation Tests in Ground, Atmospheric, Space and Accelerator Representative Environments”, *IEEE Trans. Nucl. Sci.*, vol. 63, no. 4, Art. no. 4, Aug. 2016, doi: 10.1109/TNS.2016.2528289.
- [99] CERN EN EDMS 1981751 v.1

-
- [100] J. M. Boone, J. A. Seibert, “An accurate method for computer-generating tungsten anode x-ray spectra from 30 to 140 kV”, *Med Phys*, 24(11):1661-70, Nov 1997. doi: 10.1118/1.597953. PMID: 9394272.
- [101] <https://www.nist.gov/pml/x-ray-mass-attenuation-coefficients>
- [102] <https://www.triumf.ca/proton-irradiation-facility>
- [103] <https://www.triumf.ca/pif-nif>
- [104] E. W. Blackmore, P. E. Dodd and M. R. Shaneyfelt, “Improved capabilities for proton and neutron irradiations at TRIUMF”, *IEEE Radiation Effects Data Workshop*, Monterey, CA, USA, 149-155 (2003). doi: 10.1109/REDW.2003.1281368
- [105] <https://www.triumf.ca/neutron-irradiation-facility>
- [106] C. Bélanger-Champagne, E. Blackmore, C. Lindsay, C. Hoehr and M. Trinczek, “Simulation and Measurements of Collimator Effects in Proton and Neutron Radiation Testing for Single-Event Effects”, *IEEE Trans. Nucl. Sci.*, 67, 161-168 (2020). doi: 10.1109/TNS.2019.2952003
- [107] <https://www.viavisolutions.com>
- [108] <https://www.thorlabs.com>
- [109] G. Li Vecchi, “Impact of H₂ loading on the radiation sensitivity of single-mode optical fibers”, Master Thesis, Università degli studi di Palermo and Université Jean Monnet-Saint-Etienne, 2015.
- [110] B. L. J. A.L. Huston, “Remote optical fiber dosimetry”, *Nuclear Instrument and Method in Phys. Res. B*, vol. 184, pp. 55–67, 2001.
- [111] R. L. Pease, R. D. Schrimpf, and D. M. Fleetwood, “ELDRS in Bipolar Linear Circuits: A Review”, *IEEE Trans. Nucl. Sci.*, vol. 56, no. 4, pp. 1894–1908, Aug. 2009.
- [112] E. W. Enlow, R. L. Pease, W. Combs, R. D. Schrimpf, and R. N. Nowlin, “Response of advanced bipolar processes to ionizing radiation”, *IEEE Trans. Nucl. Sci.*, vol. 38, no. 6, pp. 1342–1351, Dec. 1991.
- [113] A. H. Johnston and G. M. Swift, “Total Dose Effects in Conventional Bipolar Transistors and Linear Integrated Circuits”, *IEEE Trans. Nucl. Sci.*, vol. 46, no. 6, pp. 2427–2436, Dec. 1994.

-
- [114] A. Morana et al., “Operating Temperature Range of Phosphorous-Doped Optical Fiber Dosimeters Exploiting Infrared Radiation-Induced Attenuation”, *IEEE Trans. Nucl. Sci.*, vol. 68, no. 5, pp. 906–912, May 2021, doi: 10.1109/TNS.2021.3053164.
- [115] D. Di Francesca et al., “Radiation-Induced Attenuation in Single-Mode Phosphosilicate Optical Fibers for Radiation Detection”, *IEEE Trans. Nucl. Sci.*, vol. 65, no. 1, pp. 126–131, Jan. 2018, doi: 10.1109/TNS.2017.2778314.
- [116] J. Bisutti, *Etude de la Transmission du Signal sous Irradiation transitoire dans les fibres optiques*, Université de Saint-Etienne, Saint-Etienne, France, Thèse de Doctorat, 2010.
- [117] S. Girard, et al., “Radiation hardening techniques for Er/Yb doped optical fibers and amplifiers for space application”, *Opt. Express* 20 (8) (2012) 8457, <https://doi.org/10.1364/OE.20.008457>.
- [118] Blackmore E. W., Dodd P. E. and Shaneyfelt M. R., “Improved capabilities for proton and neutron irradiations at TRIUMF”, *IEEE Radiation Effects Data Workshop*, Monterey, CA, USA, 149-155 (2003).
- [119] JEDEC standard: <https://www.jedec.org/standards-documents/docs/jesd-89a>.
- [120] S. Girard, A. Morana, C. Hoehr, M. Trinczek, J. Vidalot, P. Paillet, C. Bélanger-Champagne, J. Mekki, N. Balcon, G. Li Vecchi, C. Campanella, D. Lambert, E. Marin, A. Boukenter, Y. Ouerdane, E. Blackmore, “Atmospheric Neutron Monitoring through Optical Fiber-Based Sensing”, *Sensors* 2020, 20, 4510; doi:10.3390/s20164510.
- [121] A. Morana, S. Girard, M. Cannas, E. Marin, C. Marcandella, P. Paillet., J. Perisse, J-R. Macé, R. Boscaino, B. Nacir, A. Boukenter, Y. Ouerdane, “Influence of neutron and gamma-ray irradiations on rad-hard optical fiber”, *Opt. Mat. Express*, 5, 898-911 (2015). doi: 10.1364/OME.5.000898
- [122] M. Benabdesselam, F. Mady, S. Girard, Y. Mebrouk, J. B. Duchez, M. Gaillardin, P. Paillet, “Performance of Ge-doped Optical Fiber as a Thermoluminescent Dosimeter”, *IEEE Trans. Nucl. Sci.*, 60, 4251-4256 (2013). doi: 10.1109/TNS.2013.2284289
- [123] M. T. Robinson, “Basic physics of radiation damage production”, *J. Nucl. Mater.*, 216, 1-28 (1994).
- [124] G. Li Vecchi et al., “In-situ regeneration of P-doped optical fiber dosimeter”, *Opt. Lett.*, vol. 45, no. 18, p. 5201, Sep. 2020, doi: 10.1364/OL.402382.

-
- [125] E. J. Friebele and M. E. Gingerich, "Photobleaching effects in optical fiber waveguides", *Appl. Opt.*, vol. 20, no. 19, pp. 3448–3452, 1981.
- [126] P.L. Swart and A.A. Chtcherbakov, "Study of Hydrogen Diffusion in Boron/Germanium Codoped Optical Fiber", *J. Lightw. Technol.*, vol.20, p.1933, 2002. doi: 10.1109/JLT.2002.806325
- [127] J. Stone, "Interactions of Hydrogen and Deuterium with Silica Optical Fibers: A Review", *J. Lightw. Technol.*, vol. LT-5, p.712, 1987.
- [128] H. Henschel and O. Kohn, "Regeneration of irradiated optical fibres by photobleaching?", in 1999 Fifth European Conference on Radiation and Its Effects on Components and Systems. RADECS 99 (Cat. No.99TH8471), Fontevraud, France, 2000, pp. 502–507. doi: 10.1109/radecs.1999.858632
- [129] H. Henschel, O. Kohn, and H. U. Schmidt, "Radiation hardening of optical fibre links by photobleaching with light of shorter wavelength", *IEEE Trans. Nucl. Sci.*, vol. 43, no. 3, pp. 1050–1056, Jun. 1996
- [130] P. Borgermans, B. Brichard, F. Berghmans, M. C. Decreton, K. M. Golant, A. L. Thomashuk, and I. V. Nikolin "Dosimetry with optical fibers: results for pure silica, phosphorous, and erbium doped samples", *Proc. SPIE 4204, Fiber Optic Sensor Technology II*, (1 March 2001); doi.org/10.1117/12.417404
- [131] D. Di Francesca et al., "Combined Temperature Radiation Effects and Influence of Drawing Conditions on Phosphorous-Doped Optical Fibers", *Phys. Stat. Sol. (a)*, p. 1800553, Dec. 2018, doi: 10.1002/pssa.201800553.
- [132] P. Borgermans, B. Brichard, F. Berghmans, M. Decréton, K.M. Golant, A.L. Thomashuk and I.V. Nikolin, "Dosimetry with optical fibers: results for pure silica, phosphorous, and erbium doped samples", presented at the Environmental and Industrial Sensing, Boston, MA, 2001, pp. 151–160.
- [133] S. Girard, Y. Ouerdane, A. Boukenter, C. Marcandella, J. Bisutti, J. Baggio, J.-P. Meunier, "Integration of Optical Fibers in Megajoule Class Laser Environments: Advantages and Limitations", *IEEE Trans. Nucl. Scie.* 59, 1317-1322 (2012). doi: 10.1109/TNS.2012.2199130
- [134] R. T. Ghahrizjani, M. Ameri, H. Jahanbakhsh, H. Sadeghi, and E. Mohajerani, *IEEE Sensors Journal*, 1 (2020)

-
- [135] A. V. Faustov et al., “Application of phosphate doped fibers for OFDR dosimetry”, *Results in Physics*, vol. 6, pp. 86–87, 2016, doi: 10.1016/j.rinp.2016.02.001.
- [136] A. V. Faustov, A. Gusarov, L. B. Liokumovich, A. A. Fotiadi, M. Wuilpart, and P. Mégret, “Comparison of simulated and experimental results for distributed radiation-induced absorption measurement using OFDR reflectometry”, Krakow, Poland, May 2013, p. 87943O, doi: 10.1117/12.2026786.
- [137] I. Toccafondo et al., “Raman Distributed Temperature Sensing at CERN”, *IEEE Photon. Technol. Lett.*, vol. 27, no. 20, pp. 2182–2185, Oct. 2015.
- [138] I. Toccafondo, Y. Kadi, EDMS id: 1703074/PSB-EIOF-EC-0001 v.1.0
- [139] D. Di Francesca, Y. Kadi, EDMS id: 1843997/PS-EIOF-EC-0001 v.1.0